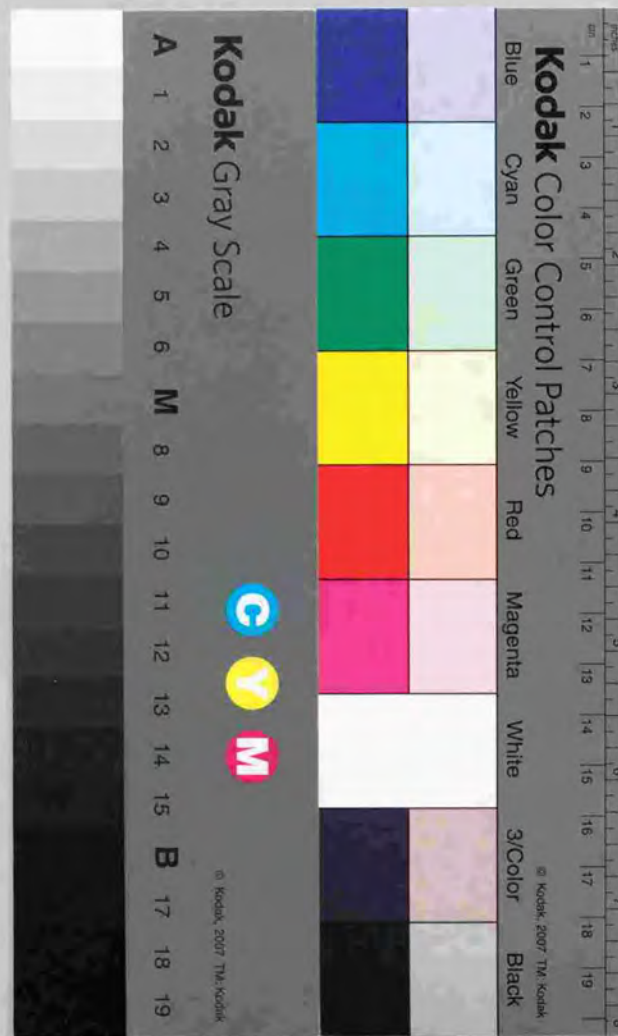学位論文

Sub-5-fs pulse generation
by noncollinear optical parametric amplification and
its application to the study of geometrical relaxation
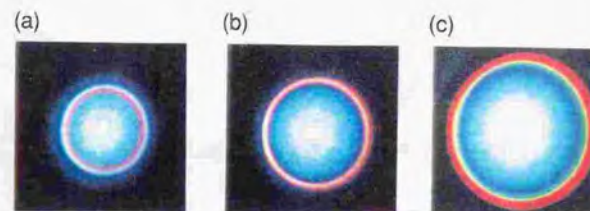in polydiacetylenes

(非平行光パラメトリック増幅によるサブ 5fs パルス発生と
そのポリジアセチレンにおける構造緩和の研究への応用)

平成 10 年 12 月 博士(理学)申請

東京大学大学院理学系研究科
物理学専攻

白川 晃

Photograph I. Far-field patterns of the type-I optical parametric fluorescence generated from a β-BaB$_2$O$_4$ crystal pumped at 395 nm. The crystal angles are at (a) $\theta \cong 31.1°$, (b) $\theta \cong 31.5°$, and (c) $\theta \cong 33.3°$, respectively.

Photograph II. Noncollinear optical parametric amplification for $\theta = 31.5°$. The signal is amplified on the dispersion-minimized fluorescence cone surface with the noncollinear angle $\alpha = 3.7°$. The idler emission is clearly observed by the visible second harmonics. The fan-shaped structure with a large spectral angular dispersion is well exhibiting the signal-idler group-velocity-matched interaction.

Dissertation

Sub-5-fs pulse generation

by noncollinear optical parametric amplification and

its application to the study of geometrical relaxation

in polydiacetylenes

(非平行光パラメトリック増幅によるサブ 5fs パルス発生と

そのポリジアセチレンにおける構造緩和の研究への応用)

Akira Shirakawa

Department of Physics, Graduate School of Science,

University of Tokyo

December 1998

Contents

1. Introduction

In the forthcoming 21-st century, orders of magnitude higher-density, higher-speed communication is expected to be required than the current system based on semiconductor electronics. Light with the advantageous properties such as the high speed, high frequency, and parallel-processing capability is the most possible candidate and all-optical transmissions, computings, and interfaces have been progressively explored in these two decades. Of quite importance is to realize an "optical transistor" and "optical switch", which encourages the recent investigations of materials with large optical nonlinearities and fast responses. For the widest and flexible applications it is quite important to understand the basic physical and chemical properties underlying in the ultrafast optical response. There are various processes of which the primary steps take place on femtosecond time scales. They are relaxations in condensed phase, photochemical reactions, energy-transfer processes in photosynthetic pigments, etc.. Especially a "real-time" observation of molecular vibration or phase relaxation in condensed phase requires extremely short optical pulses with less than 10-fs durations. Furthermore, a tuning ability across the wide optical spectral range is also strongly demanded for the investigations of the ultrafast relaxation mechanism in various materials with efficient excitation of electronic transitions.

In the decade of 1990's significant advances of femtosecond light sources have been experienced. This is mainly owing to the development of new solid-state laser materials with a broad gain bandwidth and mode-locking capability. Especially the appearance of a Kerr-lens mode-locked Ti:sapphire laser [1] and the successive development of the amplification system based on a chirped-pulse amplification technique [2] were the most epoch-making events. Those solid-state lasers have provided the following progress of versatile femtosecond light sources. For the extension of the spectral range of femtosecond pulses, optical parametric conversion has become a promising tool, which have succeeded in the tunable generation over the

ultraviolet (UV), visible, and infrared (IR) regions [3,4,5,6,7]. Hyper-continuum generation based on a channeled propagation generates broadest spectrum from the UV to near-IR (NIR) regions simultaneously [8]. High-harmonic generation in noble gases extends the wavelength to a few-nm region, which is well within the "water-window" [9]. The pulse generation with a high peak power is also to be mentioned and currently as high as a 100-TW peak power is obtained from a table-top system [10]. The highest reliability and easy handling capability of femtosecond solid-state lasers have spread femtosecond science over versatile fields.

One of the most progressive investigations performed in the last two decades is the generation of the shortest optical pulses. The history of pulse shortening from the era when dye lasers were dominant is shown in Fig. 1.1. Since the appearance of a Ti:sapphire laser, the bandwidth broadening of the solitary-like regime [11] realized the pulse generation with a less than 10-fs duration directly from an oscillator. For this purpose the constant group-delay dispersion (GDD) over the wide range of the gain spectral range has been pursued: the oscillator based on a prism pair produced shortest
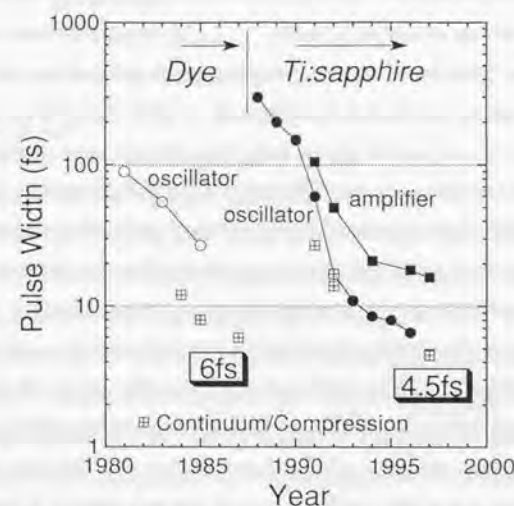

Fig. 1.1. Evolution of the pulse duration as a function of year from 1980. The shortest pulse durations of dye-laser oscillators, Ti:sapphire oscillators, and amplifiers in each year are shown.

pulses up to 8.5 fs [12], whereas the chirped-mirror technology which was also markedly progressed in this decade enabled a 7.5-fs pulse generation [13]. With the combination of chirped mirrors and a semiconductor saturable absorber mirror, the shortest pulses from an oscillator was achieved with the shortest 6.5-fs duration in 1997 [14]. The gain bandwidth broader than 200 THz of a Ti:sapphire crystal indicates the further pulse shortening less than 4 fs. However, the recent calculation considering the space-time focusing in the crystal suggested the practical limit is about 6 fs [15].

While a dye laser can generate pulses with as short as a 30-fs duration [16], the following fiber-compression stage realized the further pulse shortening [17]. Injection of ~100 fs pulses to an optical fiber causes self-phase modulation and with the combination of the dispersion the spectrum is broadened an order of magnitude with the linear frequency chirp accompanied (continuum-generation stage). The following chirp compensation by negative GDD elements reduces the pulse duration several tenths as short as that of the input pulse (compression stage). In 1987 Fork *et al.* successfully generated 6-fs pulses using a single-mode fiber and a grating-prism pulse compressor in a dye-amplifier system [18]. It had remained to be a record of the shortest pulse width for as long as 10 years.

In 1990s this "traditional" continuum-compression method has also been applied to Ti:sapphire systems and further investigated. In 1997 the 6-fs record was at last overcome by the two successive reports using basically the same method and the sub-5-fs regime was opened up for the first time. Baltuska and his coworkers obtained high-repetition-rate 4.6-fs pulses with an about 10-nJ pulse energy based on a cavity-dumped Ti:sapphire oscillator [19] and a single-mode fiber [20,21]. In the case of the single-mode fiber there is a fundamental problem of the restricted operation at a relatively low pulse energy. This was solved by Nisoli *et al.* by use of a hollow fiber filled with noble gases such as Ar and Xe [22]. 20-fs pulses from a Ti:sapphire amplifier was then continuum-compressed down to 4.5 fs with the pulse energy of several 10 μJ [23,24] and 5.1 fs with a 500-μJ energy [25] at 1 kHz, with the peak power of as high as 0.1 TW.

Even though both methods of a broadband Ti:sapphire laser and a continuum

compression have made the success to generate such short pulses, the applicability to a time-resolved spectroscopy is limited. The wavelength is mainly fixed to the NIR region or, even to partial regions in the UV by the harmonic generation. Because most of interesting materials have various electronic transition energies over the wide visible range, extremely short pulses covering the visible spectral region with the tuning ability is highly required for the investigation of such physical systems.

In this thesis a novel method of ultrashort pulse generation is proposed and experimentally investigated. Noncollinear optical parametric amplification (NOPA) provides an order of magnitude broader parametric gain bandwidth than that in a collinear geometry, and with the combination of a pulse-front matching and angular-dispersion compensation geometries sub-10-fs pulses can be obtained in a wide tuning range both in the visible and NIR. This is the first light source which generates tunable sub-10-fs pulses. The shortest duration of 4.7 fs was achieved in the visible range with a 5-μJ pulse energy. This is the first sub-5-fs source by other methods than the continuum-compression scheme. This NOPA is believed to be the most useful light source for ultrafast spectroscopy with the highest time resolution, and to lead us to a new regime in ultrafast science.

Outline of this thesis

The outline of the rest of this thesis is as follows. In Chapter 2 the basic principle of NOPA is explained and demonstrated in an OPA based on a β-BaB$_2$O$_4$ crystal. The noncollinear geometry can realize a group-velocity matching between the signal and idler, which is equivalent to an achromatic phase matching with the spectral angular dispersion, and the broadest gain bandwidth is attained. It is shown that a pulse-front tilting intrinsic for a noncollinear interaction limits the pulse-width shortening. In Chapter 3 a pulse-front-matching geometry is introduced and the transform-limited sub-10-fs pulse generation is demonstrated with the tunability between 550 and 700 nm. The angular-dispersion compensation of the idler realizes sub-10-fs pulses also in the NIR. The shortest 4.7-fs visible pulses are achieved by a pulse compressor

composed of a prism pair and customized chirped mirrors with the bandwidth of broader than 200 THz. Also remarked are the future prospects of this NOPA.

In Chapter 4 a spectroscopic application of the sub-5-fs NOPA to a pump-probe experiment of a polydiacetylene (PDA) film is presented. The long-living high-frequency wavepacket motion of C=C (23fs) and C≡C (16fs) stretching along the backbone characterizes the coherent relaxation from free excitons (FEs) to self-trapped (geometrically-relaxed) states via self-trapped excitons and internal conversion within 80 fs. The wavepacket motion in a self-trapped state is transferred coherently from a FE, which indicates the coherent motions of the C=C and C≡C stretching act as the driving force of the geometrical relaxation to a localized butatriene-like structure. The diabatic coupling of the stretching modes with the planar bending mode of C–C=C is characterized by the mode-frequency modulation at ~230 cm^{-1}. Such dynamical molecular motions are observed for the first time, which clearly reflects the advantages of the NOPA.

Finally Chapter 5 summarizes this thesis. In Appendix A several formulas about pulse-front tilting are described using analytical expressions. Appendix B contributes to the technical details of ray-tracing calculations developed for the design of pulse compressors, and the problem of geometrical smearing non-negligible in a 5-fs regime is discussed in Appendix C.

2. Broadband Optical Parametric Amplification by Noncollinear Phase Matching

2.1. Introduction

2.1.1. Tunable Femtosecond Light Source Targeting a 10-fs Regime

Because the spectral range covered by the gain spectra of laser media applicable to femtosecond operation is only a limited part of the whole optical frequency range, the wavelength conversion of the laser output has been one of the most important subjects in ultrafast science. Numerous studies have been reported using various methods such as dye amplification, harmonic generation, and optical parametric conversion.

Femtosecond dye lasers and amplifiers were extensively investigated in 1980s. Because the family of versatile organic dyes can cover the visible spectral range it seems possible to obtain femtosecond pulses at any wavelength in the visible [26]. However, because of the lack of the saturable absorber suitable for a given gain dye, it has been difficult to obtain tunable pulses directly form lasers. Thus the continuum generation followed by amplification was used exclusively and the wavelengths were extended to blue-green and 800-nm regions from a standard colliding-pulse mode-locked (CPM) dye-laser system operated around 620 nm. In this way ~20-fs pulses were generated [27] which duration is determined by the gain bandwidths of dyes. For the further shortening a successive continuum compression was pioneered and the noteworthy 9- and 10-fs pulse generations were achieved at 800 nm in 1989 [28] and at 500 nm in 1991 [29], respectively. However, its shortcomings such as complicated apparatus, maintenance problem due to easy chemical degradation, and low stability induced by the mechanical fluctuation of dye jets have strongly imposed us to do a complete about-face for further progresses.

The simplest method of the wavelength conversion is the harmonic generation of a

laser output. Recent efforts have exhibited the novel generations of ultrashort pulses around 400 and 270-nm regions, respectively by the second-harmonic generation (SHG) and third-harmonic generation (THG) of a Ti:sapphire system. Around 400 nm pulses with as short as 10-fs durations have been generated by the direct SHG of a 10-fs oscillator [30] and the hollow-fiber-compression technique [31]. This technique was applied to the THG and sub-20-fs UV pulses were obtained [32]. The much higher harmonic generations have also been investigated [9,33,34] and a 27-fs pulse generation at the 7th harmonic was marked [35]. However, because of its discrete spectrum and limitation to the UV region, further extension of the tuning range is always desired for spectroscopic applications.

2.1.2. Femtosecond OPAs

Recently optical parametric oscillation (OPO) and optical parametric amplification (OPA) have become popular methods for tunable femtosecond pulse generation, especially after the appearance of femtosecond Ti:sapphire lasers [3,4,5,6]. The high power and excellent stability of a Ti:sapphire system make the optical parametric conversion as the most promising method to obtain tunable ultrashort pulses. The progress of the growth of nonlinear optical crystals with large nonlinear coefficients and damage thresholds in 1980s also bases the versatile applications in this decade [36].

From ~1994 an OPA pumped by a Ti:sapphire amplifier has shown an innovation for ultrashort pulses tunable outside the 800-nm region with a μJ pulse energy. An OPA pumped at ~800 nm (fundamental of Ti:sapphire) generates the near-infrared (NIR) pulses in the range between 1 and 4 μm, whereas that pumped at ~400 nm (SH of Ti:sapphire) can cover the shorter visible-NIR optical region between 450 nm and 3.5 μm [4,5,6,37,38,39,40,41,42] The following harmonic generation, sum-frequency generation (SFG), and difference-frequency generation (DFG) of the signal and idler can be used to cover the range from 200 nm to 12 μm, almost the whole optical frequency region [4,5,6].

However, the shortening of the output pulse from an OPA faces a problem of the

bandwidth of the phase-matching condition. The phase-matching and energy conservation conditions are given by

$$k_p = k_s + k_i, \tag{2.1}$$

$$\omega_p = \omega_s + \omega_i, \tag{2.2}$$

where k_j and ω_j are the wavevector and angular frequency with the suffixes j = p, s, and i corresponding to the pump, signal, and idler, respectively. Approximating the plane-wave interaction and neglecting the pump depletion and spectral width, the well-known parametric gain G is given by [43,44]

$$G = \left(\Gamma l_c \cdot \frac{\sinh(g l_c)}{g l_c} \right)^2 + 1,$$

$$g = \sqrt{\Gamma^2 - \left(\frac{\Delta k}{2} \right)^2}, \Gamma = 2 d_{eff} \sqrt{\frac{\omega_s \omega_i \Phi}{\varepsilon_0 n_s n_i n_p c^3}}, \tag{2.3}$$

where Γ is the coupling constant, d_{eff} is the effective nonlinear coefficient of the nonlinear optical crystal, c is the vacuum light velocity, ε_0 is the vacuum dielectric constant, Φ is the pump intensity, l_c is the crystal length, and n_j is the refractive index of the corresponding wave. The phase mismatch Δk along the pump direction is written in a general expression as

$$\Delta k = k_p - k_s \cos \alpha - k_i \cos \beta, \tag{2.4}$$
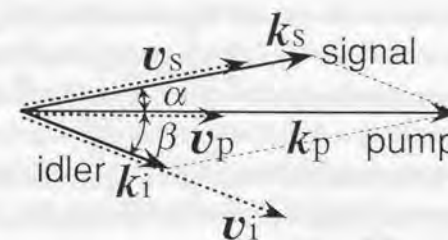

Fig. 2.1. Geometrical configuration of the wavevectors in an OPA. The wavevectors of the pump (k_p), signal (k_s), and idler (k_i) are shown in the gain crystal. The α and β are internal noncollinear angles. The group velocities of the pump (v_p), signal (v_s), and idler (v_i) are also shown by dashed lines.

where α and β are the noncollinear angles which the wavevectors of the signal and idler make with that of the pump, respectively. Figure 2.1 illustrates the arrangement of the general noncollinear configuration.

In the typical collinear geometry ($\alpha = \beta = 0$) the expression is simplified. By Taylor expansion in powers of the angular frequencies around the central frequencies ω_{s0} and ω_{i0}, Δk is given by

$$\Delta k = -\left(\frac{1}{v_s} - \frac{1}{v_i}\right)\Delta\omega_s - \frac{1}{2}\left(\frac{\partial^2 k_s}{\partial\omega_s^2} + \frac{\partial^2 k_i}{\partial\omega_i^2}\right)(\Delta\omega_s)^2 + \cdots, \tag{2.5}$$

where $\Delta\omega_s \equiv \omega_s - \omega_{s0}$ and $\Delta\omega_i \equiv \omega_i - \omega_{i0}$ and we use $\Delta\omega_i = -\Delta\omega_s$ under the monochromatic pump approximation. $v_j = \left(\frac{\partial k_j}{\partial\omega_j}\right)^{-1}$ is the group velocity of a j-th component at the central frequency. If we assume the first-order variation, the parametric bandwidth defined as the FWHM of the gain spectrum $G(\omega_s)$ is given by [44]

$$\Delta\nu_{parametric} = \frac{0.53}{\left|\frac{1}{v_s} - \frac{1}{v_i}\right| \cdot c}\sqrt{\frac{\Gamma}{l_c}}. \tag{2.6}$$

This expression well explains that the group-velocity mismatch (GVM) between the signal and idler in the nonlinear optical crystal determines the bandwidth of an OPA. The GVM is an intrinsic effect for the ultrashort pulse interaction and determines the parametric bandwidth around 200–500 cm^{-1} in standard OPAs [44]. The previously reported femtosecond OPAs with the collinear geometry have suffered from this problem and the shortest pulse durations have been limited to ~40 fs in the visible [40] and to ~30 fs in the NIR [6,41].

The broadening of the parametric bandwidth is an essential factor to obtain a tunable sub-10-fs light source. Sosnowski et al. demonstrated a spectral broadening of the signal to about 800 cm^{-1} in the visible region by a multi-stage amplification in which different spectral regions are amplified at each stage with slightly different crystal angles [45]. However, this method has shortcomings such as the rather complicated arrangement. Very recently novel NIR OPAs have been reported

successively. Fournier et al. have used the cascading process of the SHG of a signal and the self-compression to 20-fs signal pulses is obtained [46]. Nisoli et al. demonstrated the shortest 14.5-fs signal pulse generation around 1.5 μm by use of an ultrashort 18-fs pump source from a Ti:sapphire amplifier followed by a hollow-fiber compressor [47]. Both methods seem to be difficult and too sensitive to the pump energy because the third-order effects take an essential role for the characteristic pulse propagation in their schemes. Simpler and more robust methods are strongly desired for the shorter pulse generation.

2.1.3. Recent Advances of Noncollinearly Phase-matched Optical Parametric Conversion

The idea of a noncollinear phase matching (NCPM) is not new for the broadband amplification. Takeuchi et al. reported a broadband generation of idler pulses by focusing a white-light continuum with a large convergence angle into the crystal to be phase-matched noncollinearly among the wide range of the continuum [48]. The bandwidth was increased to as broad as 1300 cm^{-1} in the NIR. They used the noncollinearly generated signal and idler just around the pump axis. In the present work an NCPM is investigated which the signal and idler are arranged with larger noncollinear angles as shown in Fig. 2.1.

The NCPM has characteristic advantages over the collinear phase matching, which is dominant in the OPAs reported in literatures. In an OPO, the NCPM is often adopted to compensate the spatial walk-off of the extraordinary ray in the crystal and increases the gain [3,49,50,51,52,53]. A temporal walk-off caused by the GVM can also be improved by the NCPM [54,55,56]. Trapani et al. demonstrated an NCPM in an OPA for satisfying the group-velocity matching between the pump pulse and signal or idler pulse in a β-BaB$_2$O$_4$ (BBO) crystal to obtain a higher conversion efficiency with the longer interaction length than in the case of a collinear OPA [54,55,56].

It is in these few years that the NCPM is recognized as a method to attain the broadest parametric bandwidth by the signal-idler group-velocity matching. The first report of this type of an NCPM was made by Gale and his coworkers in 1995 [50],

who constructed a synchronously-pumped OPO based on a BBO crystal. The noncollinear geometry of the pump and oscillating signal realized the broadband phase-matching condition and provided as short as 13-fs pulses in the visible range. Also reported was the generation of the broad spectrum over 100 nm in a nanosecond OPO based on the same configuration [57]. We have demonstrated a noncollinearly phase-matched OPA (NOPA) using a BBO and achieved a tunable 14-fs pulse generation in the visible with 3–8-µJ pulse energies in 1997 [58,59,60]. While there exists a strict restriction for the synchronization condition between the pump and signal pulses as well as the bandwidth limitations of cavity mirrors in a synchronously-pumped OPO [61], a femtosecond NOPA is expected to generate the shorter pulses with a multi-µJ pulse energy and broad tunability. Further extensive investigations have been performed successively [62,63,64,65,66,67], and the NOPA is attracting many scientists owing to its remarkable advantages. Table 2.1 summarizes the properties of the reported NOPAs, including the works presented here. Our results have always taken the lead in the field and by introducing a pulse-front-matching geometry [64] a sub-5-fs pulse generation has been attained in the visible region [66,67]. This is the first sub-5-fs light source by other methods than the conventional continuum-compression scheme. In this thesis we would like to present our experimental works toward the sub-5-fs pulse generation.

Author	Year	Region	Tuning	Pulse Width	$\Delta t \cdot \Delta v$	Ref.
Shirakawa et al.	1997	550 ~ 700 nm	delay line	> 14 fs	0.6 ~ 1.1	[58,59]
		460 ~ 1150 nm	θ	> 18 fs		[60]
Wilhelm et al.	1997	470 ~ 750 nm	α, θ	> 16 fs	0.4 ~ 0.5	[62]
Cerullo et al.	1997	500 ~ 700 nm	delay line	> 11 fs	0.6 ~ 0.9	[63]
Shirakawa et al.	1998	550 ~ 700 nm	delay line	> 6.1 fs	0.33	[64]
		900 ~ 1300 nm		> 8.4 fs	0.42	
Cerullo et al.	1998	500 ~ 800 nm	—	7.3 fs	0.65	[65]
Shirakawa et al.	1998	500 ~ 800 nm	—	4.7 fs	0.52	[66,67]

Table 2.1. Property of NOPAs reported in 1997–1998. Our works are indicated by gray columns. α, signal noncollinear angle; θ, crystal angle.

2.2. Noncollinear Optical Parametric Amplification (NOPA)

2.2.1. Broadband Phase-matching Condition – Achromatic Down-Conversion

In the noncollinear geometry, the phase mismatch is expressed with more parameters than in the collinear geometry. Angles α and β are wavelength-dependent and are expanded around the central frequency as

$$\cos\alpha = \cos\alpha_0 - \sin\alpha_0 \left(\frac{\partial\alpha}{\partial\omega_s}\right)_0 \Delta\omega_s - \frac{1}{2}\cos\alpha_0 \left(\frac{\partial^2\alpha}{\partial\omega_s^2}\right)_0 (\Delta\omega_s)^2 + \cdots,$$

$$\cos\beta = \cos\beta_0 + \sin\beta_0 \left(\frac{\partial\beta}{\partial\omega_i}\right)_0 \Delta\omega_s - \frac{1}{2}\cos\beta_0 \left(\frac{\partial^2\beta}{\partial\omega_i^2}\right)_0 (\Delta\omega_s)^2 + \cdots,$$

(2.7)

where the subscript 0 denotes the central value. From the phase-matching condition of Eq.(2.1) we obtain

$$k_p = k_{s0}\cos\alpha_0 + k_{i0}\cos\beta_0,$$

$$k_{s0}\sin\alpha_0 = k_{i0}\sin\beta_0.$$

(2.8)

By substituting Eqs.(2.7) and (2.8) into Eq.(2.4) we can expand the phase mismatch as

$$\Delta k = -\left[\frac{\cos\alpha_0}{v_s} - \frac{\cos\beta_0}{v_i} - k_{s0}\sin\alpha_0 \left(\frac{\partial\alpha}{\partial\omega_s}\right)_0 + k_{i0}\sin\beta_0 \left(\frac{\partial\beta}{\partial\omega_i}\right)_0\right]\Delta\omega_s + \cdots. \quad (2.9)$$

Thus the first-order coefficient can include the dispersion of the noncollinear angles. It means that the signal-idler group-velocity mismatch in Eq.(2.6) can be modified by the wavelength-dependent noncollinear angles. In the case

$$\frac{\cos\alpha_0}{v_s} - \frac{\cos\beta_0}{v_i} - k_{s0}\sin\alpha_0 \left(\frac{\partial\alpha}{\partial\omega_s}\right)_0 + k_{i0}\sin\beta_0 \left(\frac{\partial\beta}{\partial\omega_i}\right)_0 = 0 \quad (2.10a)$$

the first-order phase mismatch is eliminated and an extremely broadband phase matching is enabled. The corresponding condition along the direction perpendicular to the pump can be derived in the same way as

$$\frac{\sin\alpha_0}{v_s} + \frac{\sin\beta_0}{v_i} + k_{s0}\cos\alpha_0 \left(\frac{\partial\alpha}{\partial\omega_s}\right)_0 + k_{i0}\cos\beta_0 \left(\frac{\partial\beta}{\partial\omega_i}\right)_0 = 0. \quad (2.10b)$$
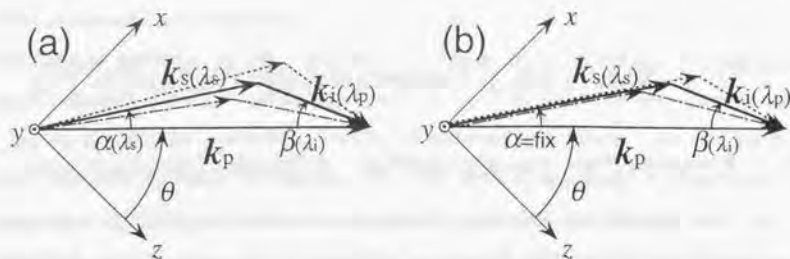
Fig. 2.2. Signal-idler group-velocity matching in the (a) general geometry and (b) special geometry for $\alpha = $ const.. x, y, z, and θ denote the crystal axes and angle in the case of the present work.

By Eq.(2.10) we can define in a broad sense the group-velocity matching in the noncollinear geometry.

In the case of a conventional collinear geometry ($\alpha = \beta = 0$) this condition is only satisfied when

$$v_s = v_i,$$ (2.11)

which is only satisfied at the degeneracy ($\omega_s = \omega_i = \omega_p/2$) in a type-I interaction ($e \to o + o$ or $o \to e + e$). In a type-II interaction ($e \to o + e$ or $o \to o + e$) the GVM is in general larger due to the large birefringence in practical crystals [42,44].

On the other hand, in the noncollinear geometry the angular dispersion can eliminate the GVM and a broadband phase matching can be attained. The schematic of this configuration is depicted in Fig. 2.2(a). The angular dispersions satisfying this condition are calculated from Eq.(2.10) as

$$\left(\frac{\partial \alpha}{\partial \omega_s} \right)_0 = \frac{v_s^{-1} \cos(\alpha_0 + \beta_0) - v_i^{-1}}{k_{s0} \sin(\alpha_0 + \beta_0)},$$
$$\left(\frac{\partial \beta}{\partial \omega_i} \right)_0 = \frac{v_i^{-1} \cos(\alpha_0 + \beta_0) - v_s^{-1}}{k_{i0} \sin(\alpha_0 + \beta_0)}.$$ (2.12)

This kind of phase matching is well known as an achromatic phase matching [68,69], which has attracted many scientists to obtain a broadband wavelength conversion of ultrashort pulses [70,71,72,73,74,75,76]. All applications ever reported were *up-conversion* such as SHG and SFG, and much interest has been focused onto the technique to prepare the desired angular dispersion of the input beams. However, in the present case it is *down-conversion* so the broadband condition can be automatically satisfied by the generation of the angular-dispersed signal and idler. The characteristic feature will be discussed in the next section.

For practical applications such as an OPA which amplifies a seeded weak signal the angular dispersion is not desired. Thus we consider the case that the signal has no angular dispersion ($\alpha = \alpha_0$). The schematic is shown in Fig. 2.2(b). For $\alpha = \alpha_0$, Eq.(2.12) yields the simple group-velocity matching condition

$$v_s = v_i \cos(\alpha + \beta),$$ (2.13)

with

$$\frac{\partial \beta}{\partial \omega_i} = -\frac{1}{k_i \cos \beta} \left(\frac{\sin \alpha}{v_s} + \frac{\sin \beta}{v_i} \right) = -\frac{\tan(\alpha + \beta)}{k_i v_i},$$ (2.14)

where the subscript 0 is removed for simplicity. The condition is then simplified as the projection of the idler group velocity to the signal direction is equal to the signal group velocity. The phase mismatch in Eq.(2.9) can then be rewritten as

$$\Delta k = -\frac{\cos(\alpha + \beta)}{\cos \beta} \left(\frac{1}{v_s} - \frac{1}{v_i \cos(\alpha + \beta)} \right) \Delta \omega_s + \cdots,$$ (2.15)

which clearly indicates the broadband phase matching in the case of the group-velocity matching.

Note that this group-velocity matching is owing to the idler angular dispersion given by Eq.(2.12). We use the term of the "signal-idler group-velocity matching" in this special case. The above mentioned general group-velocity matching is to be called an "achromatic phase matching" hereafter for simplicity.

For small α condition applicable to many experiments, $\frac{\cos(\alpha + \beta)}{\cos \beta} \sim 1$ within a 2-% accuracy, so that it is convenient to use the general GVM defined as

$$GVM_{s-i} = \frac{1}{v_s} - \frac{1}{v_i \cos(\alpha + \beta)}.$$ (2.16)

The GVM between the pump and signal, which limits the interaction length in the crystal, is also given by [54]

$$GVM_{p-s} = \frac{1}{v_p} - \frac{1}{v_s \cos\alpha}. \tag{2.17}$$

As clearly seen from Eqs.(2.16) and (2.17), both GVMs are dependent on the noncollinear angle α and can be eliminated by a proper geometrical arrangement. The group-velocity matching between the pump and signal or idler by the noncollinear geometry in the case of $v_s > v_p$ was reported and an order of magnitude longer interaction length than that in the collinear geometry can be obtained [54,55,56]. Our current interest is the signal-idler group-velocity matching, which is possible if $v_s < v_i$. The bandwidth is broadened by more than ten times and is only limited by the group-velocity dispersion (GVD) as indicated in Eq.(2.5) [44], and an ultrashort pulse generation is expected

2.2.2. Group-velocity Matching in β-BaB$_2$O$_4$

In order to understand the characteristic behavior of the achromatic phase matching an NCPM in a BBO crystal is considered. A BBO crystal is widely used for a gain crystal of an OPA because of the advantages of the broad tunability, high damage threshold, and large nonlinear coefficient [44]. A type-I ($e \rightarrow o + o$) OPA is more suitable for an ultrashort pulse generation than a type-II ($e \rightarrow o + e$) OPA because of the smaller GVM and larger effective nonlinear coefficient [42,44,47].

From Eq.(2.8) the angle θ between the pump beam and the z axis (optic axis) and the idler noncollinear angle β satisfying the type-I phase matching are respectively given by

$$\theta(\lambda_s, \alpha) = \cos^{-1}\left\{ \frac{1}{\sqrt{n_o^{-2}(\lambda_p) - n_e^{-2}(\lambda_p)}} \right.$$

$$\times \left. \sqrt{\frac{1}{\lambda_p^2 \left(n_o(\lambda_s)\cos\alpha/\lambda_s + \sqrt{(n_o(\lambda_i)/\lambda_i)^2 - (n_o(\lambda_s)\sin\alpha/\lambda_s)^2}\right)^2} - \frac{1}{n_e^2(\lambda_p)}} \right\},$$

$$\tag{2.18a}$$
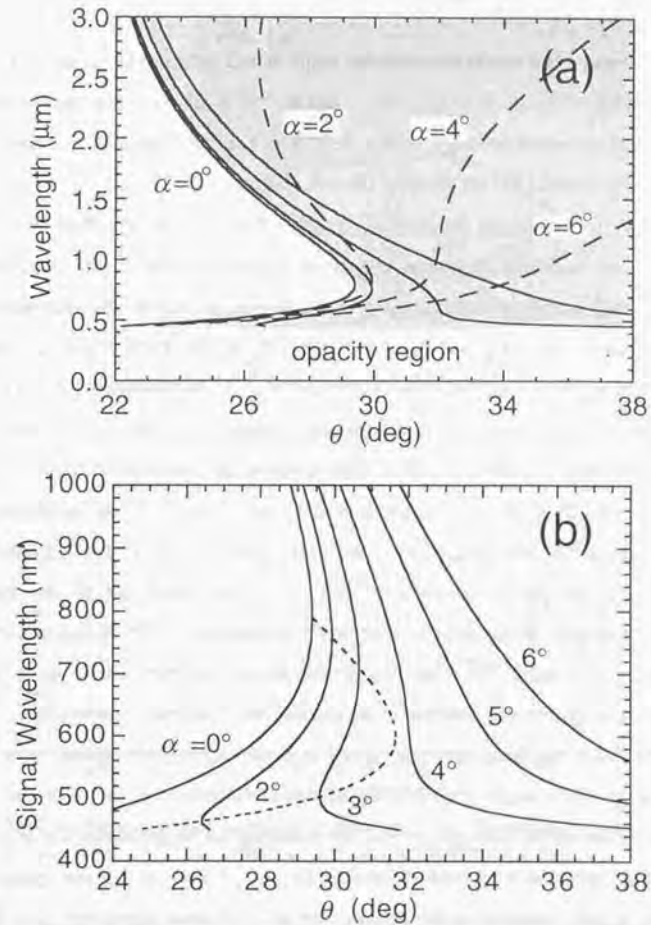
Fig. 2.3. (a) Theoretical phase-matching curves of θ in a type-I BBO OPA pumped at 395 nm with several different values of the signal noncollinear angle α. The signal branch (solid curves) and idler branch (dashed curves) are shown. The area in gray indicates the region where the achromatic phase matching is enabled. The opacity region indicated in the figure is due to the corresponding idler absorption. (b) Signal branches magnified in a wavelength region of shorter than 1000 nm. The dashed curve indicates the signal-idler group-velocity matching points.

$$\beta(\lambda_s, \alpha) = \sin^{-1}\left(\frac{n_o(\lambda_s)}{n_o(\lambda_i)} \frac{\lambda_i}{\lambda_s} \sin \alpha\right). \qquad (2.18b)$$

Here we consider the signal noncollinear angle α as a parameter. λ_j's are wavelengths with the relationship of $\lambda_i = (\lambda_p^{-1} - \lambda_s^{-1})^{-1}$ and n_o and n_e are the refractive indices of the ordinary and extraordinary rays, respectively. The Sellmeier equations of the refractive indices given in Ref. [77] are used for the calculation.

The curves of $\theta(\lambda_s, \alpha)$ for various α pumped at 395 nm are shown in Fig. 2.3. There are two branches corresponding to the signal and idler in the phase-matching curve for each non-zero α. The most characteristic feature is the enormous phase-matching activity over a broad spectral range. The region filled in gray in Fig. 2.3(a) can satisfy the phase-matching condition by a noncollinear interaction. For given θ the signal and idler waves can be simultaneously emitted in a broad range of wavelength as shown in Fig. 2.2. For $\theta < 29.4°$ the range of the spectrum is partially limited, whereas for $\theta > 29.4°$ the whole optical modes over 450 nm – 3 μm are excited, which is only restricted by the absorption of the idler in the crystal. These behaviors can be explained by the group-velocity matching in a broad sense where the appropriate angular dispersions of the noncollinear angles eliminate the GVM between the signal and idler and realizes the ultra-broadband phase matching. Note again that this condition is automatically satisfied in the interaction of a down-conversion.

Each phase-matching curve for given α is substantially modified even with the small change of the angle. Figure 2.3(b) shows the existence of an inflection, which is the point of the signal-idler group-velocity matching on the condition for $\alpha = $ const. In the spectral range of a normal dispersion ($v_s < v_i$ for $\lambda_s < \lambda_i$), the group-velocity matching is only attained at the degeneracy in a collinear geometry ($\alpha = \beta = 0$) as mentioned above. By utilizing the noncollinear geometry, on the other hand, the group-velocity matching can occur for $\lambda_s < 790$ nm as indicated by a dashed curve in Fig. 2.3(b). The wavelength dependence of α which realizes $GVM_{s-i} = 0$ is shown in Fig. 2.4. Interestingly, α has a broad maximum around 600 nm and decreases at the shorter wavelength. This is due to the negative GVD at $\lambda_i > 1.3$ μm. Over a broader spectral range than 100 nm α suffers only a small deviation of less than 0.1° from 3.7°,
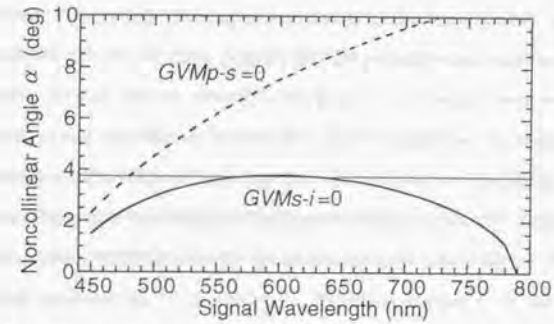
Fig. 2.4. Wavelength dependence of α to satisfy the signal-idler group velocity matching condition (solid curve). Also shown is α which satisfies group-velocity matching between the pump and signal (dashed curve). The thin line indicates $\alpha = 3.7°$.
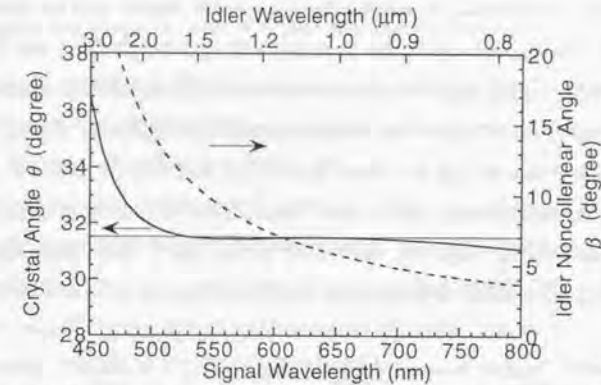
Fig. 2.5. Phase-matching curves of θ (solid curve) and β (dashed curve) in the case for $\alpha = 3.7°$, dominantly investigated in the present work.

by which a broad plateau at $\theta = 31.5\pm0.1°$ between 520 to 710 nm appears in the phase-matching curve for $\alpha = 3.7°$, as presented in Fig. 2.5.

An optical parametric fluorescence well exhibits the characteristic properties of the NCPM. We observed the fluorescence by pumping a 1-mm-thick BBO crystal with 150-fs pulses at 395 nm. The pump intensity was about 300 GW/cm². Under the intense pumping condition, a noncollinearly phase-matched optical parametric

fluorescence is strongly emitted like a cone to form a ring pattern around the pump beam due to the type-I interaction [54,78]. Photograph I shows the far-field patterns of fluorescence intensity distribution at three different crystal angles. When the BBO crystal is oriented in the range of $\theta > 30°$, where a collinear phase matching is not satisfied, a fluorescence containing a broad spectrum is emitted noncollinearly [54,78]. The ring structure has a large spectral angular dispersion along the axial direction, which visually exhibits the characteristics of an achromatic down-conversion. The dispersions of the fluorescence at $\theta \cong 33.3°$ and $\theta \cong 31.1°$ are reversed from each other. The former has larger cone angles and the intensity is higher, because GVM_{p-s} is reduced for larger α (see Fig. 2.4) [54].

The angular dispersion is minimized around $\theta = 31.5°$ and a large fraction of the visible fluorescence intensity is emitted along a conical surface with the internal cone angle of $3.7°$ (Photograph I(b)). This property well agrees with the above mentioned prediction, representing the exceptional broadband group-velocity matching. The parametric gain given by Eq.(2.3) is calculated in this configuration. Figure 2.6 shows the result in the case for $d_{eff} = 1.6\cos\theta$ pm/V [77] and $\Phi = 50$ GW/cm^2. The gain covers the enormously broad visible range from 520 to 750 nm with small variation. The bandwidth is as large as 160 THz (5300 cm^{-1}), and from the Fourier transformation the possible shortest pulse width is estimated to be 4.4 fs. Note again
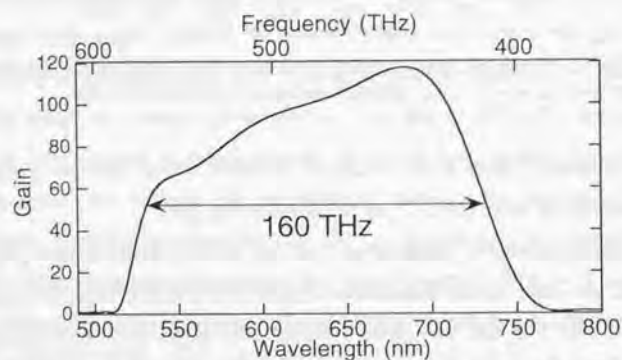

Fig. 2.6. Wavelength dependence of the parametric gain (Eq.(2.3)) in the type-I NCPM for $\alpha = 3.7°$. Here $l_c = 1$ mm and $\Phi = 50$ GW/cm^2.

that the idler waves are also generated with the same broad bandwidth in the NIR with the angular dispersion to be phase-matched with the broad spectrum of the signal waves (see Fig. 2.5).

These features indicate that a NOPA may be a quite promising method to generate ultrashort pulses over a wide visible range in a sub-10-fs regime. In the present work this characteristic signal-idler group-velocity matched interaction is focused on and the applicability to the ultrashort pulse generation is extensively investigated and explored.

2.3. Femtosecond NOPA based on β-BaB$_2$O$_4$

2.3.1. Broadband Amplification of Single-filament Continuum

The arrangement of the NOPA is schematically shown in Fig. 2.7. A mode-locked Ti:sapphire oscillator (Spectra-Physics, Tsunami) pumped by an 8-W Ar-ion laser (Coherent, Innova 310) produces 82-MHz, 80-fs pulses with a 1-W average power at 790 nm. They are then seeded to a Ti:sapphire regenerative amplifier system with a chirped-pulse amplification scheme (Clark-MXR, CPA-1000) which is pumped by a frequency-doubled CW Q-switched Nd:YAG laser (Clark-MXR, ORC-1000, 5 W, 1 kHz at 532 nm). The pulse energy and duration of the output pulse are 300 μJ and 120 fs, respectively. The SH at 395 nm is generated in a 1-mm-thick BBO crystal (type I, $\theta = 29.4°$) with a 100-μJ pulse energy and then separated from the fundamental and is utilized as a pump. The pulse width of the SH is estimated to be ~150 fs by the cross-correlation measurement with the fundamental pulse. After passing through a delay line for synchronization, the pump beam is telescoped to obtain a peak intensity ~300 GW/cm^2 and pumps a 1-mm-thick BBO crystal (type I, $\theta = 30°$). The small beam diameter of 0.5 mm is to suppress the effect of the pulse-front tilting [56] (see Section 2.3.3). The crystal is placed with the xz-plane lying in the plane of the page, and the polarization of the pump beam is on the plane as an e-ray. The thickness of the BBO crystal is determined so that the temporal walk-off due to GVM_{p-s} (~100 fs/mm) is well
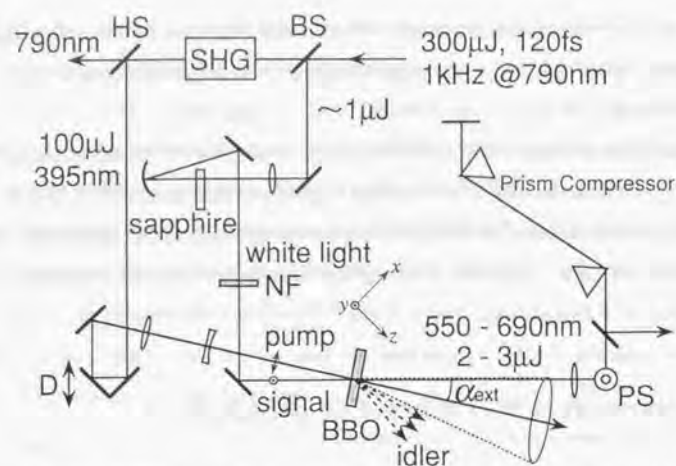
Fig. 2.7. Experimental setup for the noncollinearly phase-matched OPA (NOPA). SHG, second-harmonic generator; BS, beam sampler; HS, fundamental and second-harmonic separator; NF, notch filter centered at 800 nm; D, variable optical delay line; PS, periscope for rotating the polarization of the signal. The cone-like parametric fluorescence with the minimized dispersion (see text) is illustrated with the external cone angle α_{ext}. Also illustrated is the crystal axes x, y, and z.

below the duration of the pump pulse. A noncollinearly phase-matched parametric fluorescence is strongly emitted as shown in Photograph I. The crystal angle is adjusted to $\theta \cong 31.5°$ for the signal-idler group-velocity matching, which is assured by observing the angular dispersion of the fluorescence to be minimized. The fluorescence covering a large portion of the visible region is emitted conically with the internal cone angle of ~3.7° (Photograph I (b)).

The parametric fluorescence can also be used for the seed of an OPA [55,56]. However, it seems more promising to use a stable white-light continuum as a seed for the practical use because the gain of the amplification in such a thin crystal is not large enough to reach a saturation regime. A small fraction of the pulse energy of about 1 μJ at 790 nm is focused onto a 2-mm-thick sapphire glass and converted to a single-filament continuum to be used as the signal [39,41,79]. This type of continuum is obtained by adjusting carefully the incident pulse energy to be only slightly higher

than the threshold of the continuum generation. The stabilities of the intensity and spectrum and the spatial coherence along the cross section are both excellent and suited for the seed of an OPA. As shown in Fig. 2.8, the spectrum of the single-filament continuum covers a broad spectral range from 450 to longer than 1000 nm. There is a strong spike around 790 nm due to the fundamental pulses. Outside this region it shows a smooth feature.

The chirp property is measured by a spectrally resolved up-conversion [18,21,80]. The sum-frequency pulse of the continuum and 120-fs gate pulse at 790 nm are generated in a 0.5-mm-thick BBO crystal (type I, $\theta = 35°$) and the different spectral portions are selected in an $f = 10$-cm monochromater with an about 1-nm resolution. The wavelength-dependent group delay (GD) is determined as the center-of-mass delay position in the corresponding cross-correlation trace [21]. The dispersion of air suffering from the propagation to the up-conversion apparatus is corrected using the refractive index data in ref. [81]. The result is shown in Fig. 2.8. The GD shows a large nonlinear change around the fundamental wavelength, whereas on both sides a quasi-linear chirp is observed. This feature agrees well with the previous reports [82]. Because of the unsaturated interaction with the self-phase modulation, the single-filament continuum does not posses a linear chirp across the whole range of the
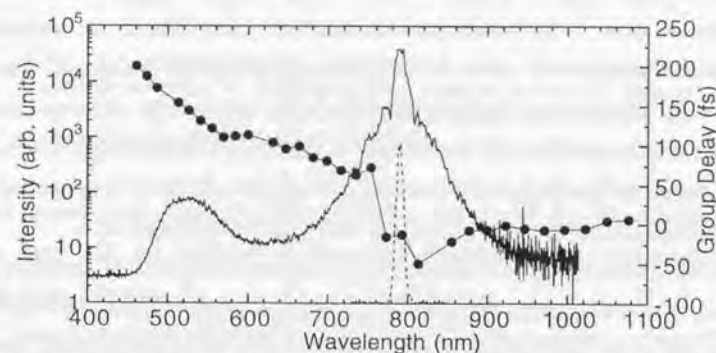

Fig. 2.8. Wavelength dependence of the intensity (solid curve, log scale) and the group delay (full circles) of the single-filament continuum. The spectrum of the injected 790-nm pulses are also shown (dashed curve, linear scale). The spectra are not intensity-calibrated.

spectrum as is well-known in optical fibers [17,18,21].

The continuum beam is collimated and passes through a notch filter with a peak reflectance of ~90 % at 800 nm to reduce the fundamental pulse energy, and then injected to propagate along the dispersion-minimized cone surface as shown in Photograph II. The direction is in the xz-plane to be matched with the Poynting vector of the pump for the walk-off compensation [49]. A broad spectral range of the continuum is noncollinearly amplified to a 2–3-μJ pulse energy with a short-term peak-to-peak fluctuation of about 10 %.

2.3.2. Output Properties

The center wavelength of the amplified signal sensitively depends on the position of the delay line of the pump pulse owing to the chirp of the continuum. By scanning the delay line with the range of 50 μm, the signal is stably tuned between 550 and 690 nm as shown in Fig. 2.9. Each of them has a broad spectrum with the bandwidth up to 2000 cm⁻¹. The small peak structures around 530 nm and 760 nm are due to the imperfect flatness of the phase-matching curve and the strong seed intensity near the fundamental, respectively. The signal suffers from no significant pulse energy reduction, indicating the bandwidth is not limited by the gain bandwidth but by the seed chirp. However, if the notch filter is removed to decrease the amount of the chirp, the intense spike of the fundamental in the seed pulse induces the substantial amplification around 790 nm as well as at the phase-matched wavelength. This is because the differences of the phase-matching angles and the GDs of the continuum between at 790 nm and at 600 nm are only 0.3° and 150 fs, respectively. The notch filter suppresses the unexpected dual-wavelength amplification both by decreasing the fundamental intensity and by separating the two signal components in time.

In this group-velocity-matching geometry the idler is also broadly generated and fan-shaped with a spanning angle of about 7° in the xz-plane, which can be observed by the SH of the idler generated from the BBO by a non-phase-matched process (Photograph II). Figure 2.10 shows the wavelength dependence of the external noncollinear angle with respect to the pump direction. It is to be mentioned that the
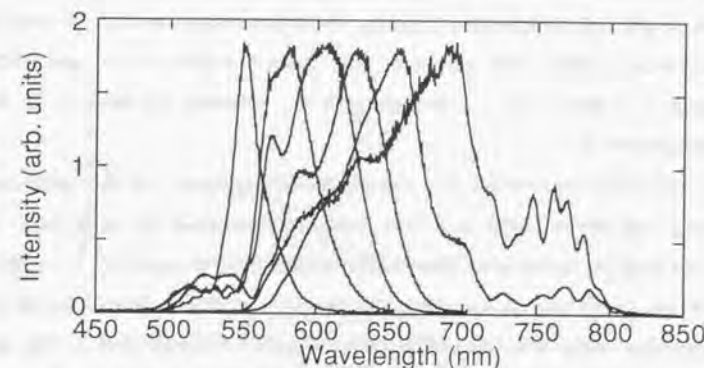
Fig. 2.9. Spectra of the amplified signal. The center wavelength can be tuned only by scanning the delay line of the pump by 50 μm.
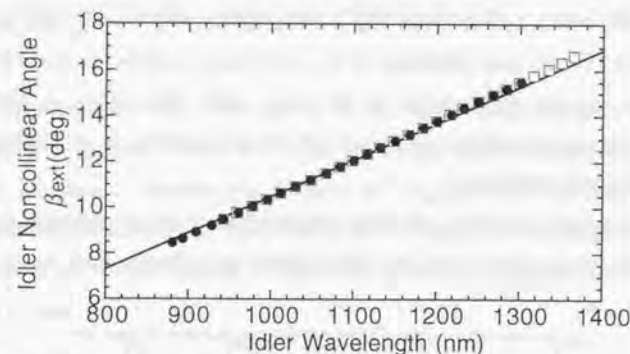
Fig. 2.10. Angular-dispersion property of the idler. Measured external noncollinear angles β_{ext} with respect to the pump are shown (full circles at $\lambda_s = 680$ nm and open squares at $\lambda_s = 600$ nm)). Also shown is the calculated phase-matching curve (solid curve).

broad spectra is observed to be distributed from 800 to 1400 nm. The measured data well agree with the theoretical phase-matching curve and show the characteristic quasi-linear dependence.

Figure 2.11 shows the background-free intensity autocorrelation trace at 625 nm after the pulse compression. A 100-μm-thick BBO (Type I, $\theta = 45°$) is used for the SHG. The pulse compressor is a pair of BK7 Brewster prisms and optimized to a 37-

cm slant length with a minimum insertion. A fit assuming a sech^2-pulse envelope function yields a pulse width of 14 fs. The spectral width of a 66-nm FWHM corresponds to a pulse width of as short as 8 fs, indicating the pulse is far from transform-limited (TL).

The measured pulse width and time-bandwidth product over the pump-delay tuning range are shown in Fig. 2.12. The bandwidths are from 700 up to 2000 cm^{-1}, with keeping sub-20-fs durations. The time-bandwidth products are 0.6–1.1, except for 0.4 at 550 nm. In the long wavelength region the spectrum distributes to ~800 nm with a non-negligible spike, which degrades the products to be larger than 1. The large time-bandwidth product is partly due to the pulse-width measuring apparatus. The autocorrelator composed of the 100-μm-thick BBO with the GVM of 40 fs at 600 nm and dispersive media such as a lens and a beam splitter may overestimate the pulse width. The 3.3-fs/step time resolution of the pulse stage used for the delay line also disturbs the accurate measurement of the pulse width. The wings on both sides observed in the autocorrelation traces also indicate the higher-order dispersion. These problems should be eliminated.

The low conversion efficiency (~5%) can be improved by an additional two-stage amplification, where both pump and signal beams are reflected back to the crystal

Fig. 2.12. Wavelength dependence of the pulse width (full circles, sech^2-fit) and time-bandwidth product (full squares). The dotted line indicates the product of a transform-limited pulse (0.315) in the case of a sech^2-pulse envelope.

twice by plane mirrors with small vertically tilting angles. Even though the gain of the first stage is as high as 10^4, the gain in the succeeding stage is smaller than 3, which reason is not clear but supposed to be due to the degradation of the beam quality by higher-order nonlinear effects. The resultant pulse energy is up to about 8 μJ, which accompanies the longer duration of about 18 fs and the increased time-bandwidth product to larger than 1.
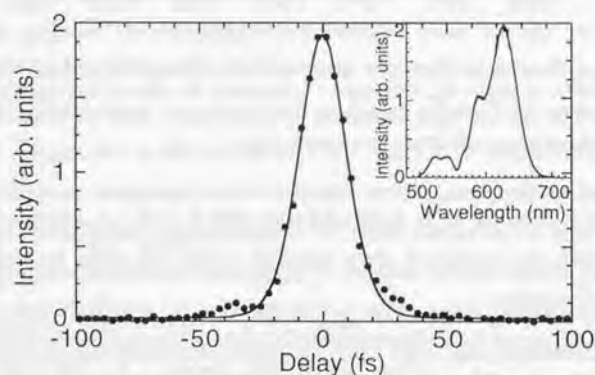

Fig. 2.11. Intensity autocorrelation trace of the amplified signal after pulse compression (full circles). The sech^2-fit (solid curve) pulse width is 14 fs (FWHM). The spectrum is shown in the inset.

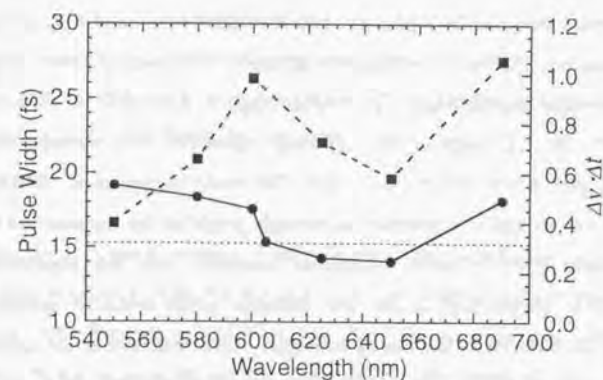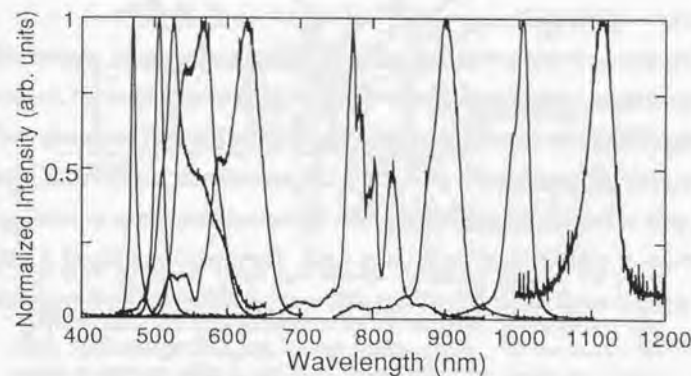Fig. 2.13. Angle-tuned spectra of the signal.

The spectral range of the signal can also be extended by angle-tuning. Figure 2.13 shows the spectra obtained by rotating the crystal by the range of about 5° in the case of the three-stage amplification. The tuning range is from 460 to 1150 nm, which covers nearly the full range of the continuum spectrum. The corresponding tuning range of the idler is from 600 nm to 2.8 μm. The stable generation at ~800 nm is to be mentioned even though the spectrum is strongly modified by the notched filter. In a type-I collinear OPA, a stable continuous tunability near the degeneracy is not available. The degeneracy causes the unstable phase-sensitive interaction [83] resulting in the absence of the tuning between ~700 to 900 nm in the collinear OPA pumped at ~400 nm [39,40]. The NCPM removes the degeneracy even under a type-I phase matching and enables the continuous tuning over the 800-nm region, like in a type-II OPA [5,6,42].

2.3.3. Limitation of Pulse Width – Pulse-front Tilting

As discussed in the last section, the NOPA based on the signal-idler group-velocity matching shows the advantageous property to generate sub-20-fs pulses with the wide tuning range of the visible. However, from the broad spectra with exceeding 2000-cm⁻¹ bandwidths, much shorter pulses with less than 10-fs durations are expected. The unexpected large time-bandwidth products are partly due to the non-optimized autocorrelator and pulse compressor as mentioned above. However, it seems to be difficult to explain the broadening factor of 2 to 3 from the TL duration.

The most probable reason is the pulse-front tilting, which is an intrinsic effect for the noncollinear interaction of ultrashort pulses [56]. Figure 2.14 shows the schematic behavior. Under the noncollinear geometry, the pulse fronts of the pump and signal cannot perfectly overlap with each other. The noncollinear amplification causes the tilted gain volume in the signal beam with the noncollinear angle α, resulting in the generation of a tilted signal by the same angle. The general property of a pulse-front tilted pulse is explained in Appendix A. The external tilt angle γ is simply given from the relation

$$\tan \alpha = \frac{v_s}{c} \tan \gamma. \tag{2.19}$$

Note that the group velocity v_s describes the refraction. The pulse-front tilting induces a temporal delay across the beam diameter d by

$$\delta t_{\text{tilt}} = \frac{d \tan \gamma}{c}, \tag{2.20}$$

which gives the maximum amount of the effective pulse broadening by a time-space coupling. In a femtosecond NOPA the tilting induces more serious problem than in a noncollinear OPO because an order of magnitude larger beam spot size is used in OPAs [56]. In the present NOPA for $\alpha = 3.7°$ the tilt angle of the exit signal is calculated to be 6.3° at 600 nm. The 0.5-mm diameter of the pump can cause broadening up to 180 fs. This value is too large to explain the present experiments. An interaction within the smaller cross section is considered to be taking place in the crystal (see Fig. 2.14). The divergence of the amplified signal and the relatively-low conversion efficiency support this explanation.

The most evident feature is the spatial chirp of the amplified signal. The pulse-front tilting is accompanied with a dispersion of the exit angle ε expressed in the

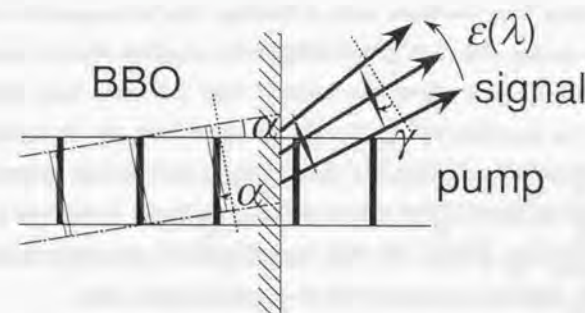Fig. 2.14. Schematic of the noncollinear interaction between the pump pulse and signal pulse. The crystal is on the left side. The volumes where the pump pulse and signal pulse exist are shown by the black and gray bold lines, respectively. The gain volume by the pump pulse introduces the tilting of the wave plate of the signal pulse by α in the crystal, resulting in the dispersion of the exit angle of the signal pulse.
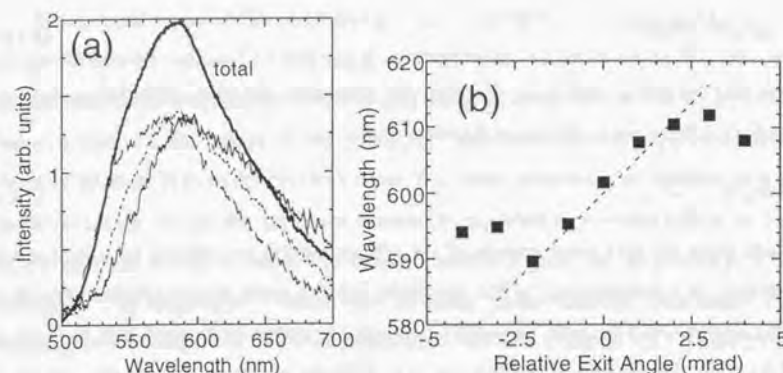
Fig. 2.15. Property of the spatial chirp. (a) Spectra passing through the vertical slit at three different positions (thin curves) and in the case of the full open (bold curve). (b) Center-of-mass wavelength as a function of the relative exit angle. The dashed line indicates the expected spatial chirp of the signal tilted by 6.3°.

formula [84] (see Appendix A):

$$\frac{d\varepsilon}{d\lambda} = -\frac{\tan\gamma}{\lambda}.$$

(2.21)

This feature originates from the inhibition of a confined beam propagation with the pulse-front tilting from the wave front, in analogy with the propagation through a prism [84] or grating [85]. The spatial chirp of the amplified signal is measured by scanning a 100-μm-wide slit on the xz-plane over the beam cross section after collimating. The spectrum passing through the slit exhibits the position-dependent feature, as shown in Fig. 2.15(a). The spatial chirp is estimated by weight-averaging the spectra and the result shows a characteristic quasi-linear dependence on the exit angle as shown in Fig. 2.15(b). The slope expected from the pulse-front tilting with $\gamma = 6.3°$ shows the surprising agreement with the measured spatial chirp.

Thus it is confirmed that the pulse-front tilting gives the limitation in the performance of the NOPA. To reduce the pulse broadening effect, the beam cross section must be minimized, which in turn causes a pulse energy reduction because of amplification saturation due to a pump depletion. Therefore eliminating the pulse-front

tilting with a relatively large beam diameter seems the most essential requirement to achieve a generation of TL sub-10-fs pulses with a medium pulse energy from a NOPA. This problem will be solved in the next chapter to obtain the remarkable progress.

3. Pulse-front-matched Noncollinear Optical Parametric Amplification

3.1. Tilted-pump Geometry for Pulse-front Matching

In Chapter 2 we have discussed noncollinear optical parametric amplification (NOPA) as a leading candidate to realize a tunable several-fs light source. However, we face an intrinsic problem to progress further pulse shortening to a sub-10-fs regime. The pulse-front tilting caused by the noncollinear interaction is the most dominant cause of the pulse-width broadening. Overlapping the pulse fronts of the pump and signal in the crystal and eliminating the pulse-front tilt is the most essential to obtain a transform-limited (TL) sub-10-fs pulses. We call this requirement as "pulse-front matching".

As discussed in Appendix A, a pulse-front tilt can be generated by using angular dispersing elements such as a prism [84] or grating [85]. The tilt angle can be also controlled by imaging optics or refraction. Thus two ways are considered for the pulse-front matching as shown in Fig. 3.1. (a) Pre-tilting the pulse front of the signal to be matched with that of the pump in the crystal. (b) Pre-tilting the pulse front of the pump
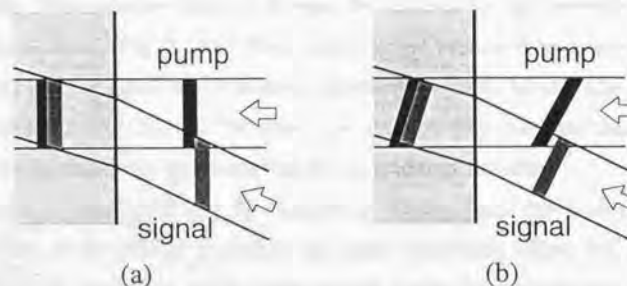
Fig. 3.1. Two schemes for the pulse-front matching between the pump and signal pulses. (a) Tilted-signal geometry. (b) Tilted-pump geometry.
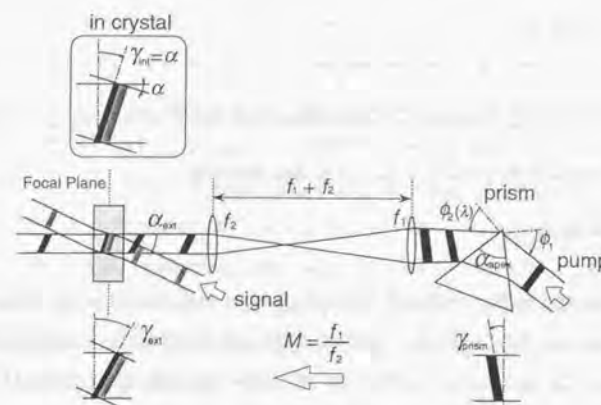
Fig. 3.2. Pulse-front matching geometry.

to be matched with that of the signal in the crystal. The scheme (a) is inconvenient because the tilted front of the signal must be corrected again after the amplification. In addition, due to the broadband spectra of the signal, there will be problems such as a nonlinear front distortion [86] and a pulse-width broadening induced by the serious (chromatic) dispersion in optical elements. Therefore the pulse front of the nearly monochromatic pump is controlled here (Fig. 3.1(b)).

The pulse-front matching geometry is schematically shown in Fig. 3.2. The pump beam passes through a prism with an incident and exit angles ϕ_1 and ϕ_2, respectively, and the pulse-front is tilted. The tilt angle γ_{prism} just after the prism is given by [84] (see Appendix A)

$$\tan \gamma_{prism} = -\lambda \frac{d\phi_2}{d\lambda} = -\frac{\sin \alpha_{apex}}{\cos \phi_1' \cos \phi_2} \lambda \frac{dn}{d\lambda}, \qquad (3.1)$$

where n is the refractive index of the prism, α_{apex} is the prism apex angle, and ϕ_1' is the internal incident angle. The tilt angle is then decreased and the pulse width is broadened during the propagation in the free space by the spectral lateral walk-off over the beam cross section [85]. The following telescope recollimates the spectral lateral walk-off and images the tilted fronts on the focal plane *with a longitudinal magnification factor $M = f_1/f_2$*, which gives the tilt angle γ_{ext} at the crystal position as

$$\tan\gamma_{ext} = -\frac{f_1}{f_2}\tan\gamma_{prism},\tag{3.2}$$

The internal tilt angle γ_{int} is reduced by refraction with the relation $\tan\gamma_{int} = \frac{v_g}{c}\tan\gamma_{ext}$. The pulse-front matching condition $\gamma_{int} = \alpha$ is then given by

$$\tan\alpha = \frac{v_g}{c}\frac{f_1}{f_2}\tan\gamma_{prism}.\tag{3.3}$$

Because the spectral lateral walk-off in the horizontal direction is insignificant in the present experimental condition, the beam is almost recollimated both horizontally and vertically. Since the spot size is reduced by the lateral magnification factor $M^{-1} = f_2/f_1$, the combination of the telescope is essentially determined by the requirement of the efficient amplification and dimensional restriction. Thus a prism apex angle and incident angle are the most essential parameters for the optimization to satisfy Eq.(3.3).

The apparatus with pre-tilting and imaging for an OPA was firstly demonstrated by Danielius *et al.* in 1996 [87,88]. However, their purpose is to control the group velocity of the pump for the efficient amplification in a collinear OPA. The combination of the tilting and walk-off of the *e*-polarized pump can realize the matching between the group velocity of the pump and the averaged group velocity of the signal and idler. The apparatus reported in this work is the first presentation of the pulse-front matching in an OPA.

3.2. Tunable Sub-10-fs Pulse Generation in the Visible

3.2.1. Experimental Setup of Pulse-front-matched NOPA

The whole experimental setup of the pulse-front matched NOPA is shown in Fig. 3.3. The pump and probe pulses are generated basically in the same way as described in Chapter 2, however, the details are improved. The Ar-ion laser is replaced by a laser-diode-pumped intracavity-doubled CW Nd:YVO$_4$ laser (Spectra-Physics,

Millennia; 5W at 532 nm), resulting in the oscillator pulses of a 600-mW average power and an ~80-fs duration. The pulse energy of the amplified pulses are increased to 400 μJ by an 8-W pumping by the Nd:YAG laser. A 1-mm-thick LiB$_3$O$_5$ crystal (type I, $\theta = 90°$, $\phi = 33.7°$) in place of a BBO is used for the SHG of the fundamental pulses to reduce the walk-off effect and used as a pump. The stage of the continuum generation is the same as before. The notch filter which was used to prevent undesired amplification of the fundamental spike is replaced by a thin 175-μm-thick high-pass filter ($T < 0.1$ % at > 750 nm) to minimize the seed chirp. The signal beam is aligned to be propagated on a dispersion-minimized cone and amplified with the noncollinear internal angle α of 3.7°.
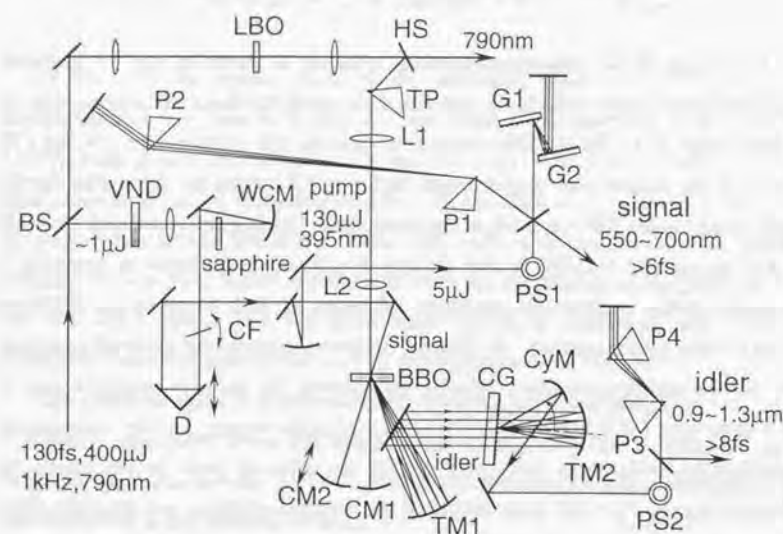
Fig. 3.3. Schematic of the sub-10-fs NOPA. BS, beam sampler; HS, harmonic separator; TP, prism for pulse-front tilting; L1, L2, $f = 200$- and 71-mm lenses; CM1, CM2, spherical mirrors ($r = 100$ mm); VND, variable neutral-density filter; WCM, spherical mirror ($r = 120$ mm); CF, cut-off filter; D, optical delay line; TM1, spherical mirror ($r = 250$ mm); TM2, cylindrical mirror ($r = 115$ mm); CG, grating (600 ℓ/mm); CyM, cylindrical mirror ($r = 77.85$ mm); PS1, PS2, periscope; P1, P2, 45° fused-silica prism pair; P3, P4, 60.2° SF10 prism pair; G1, G2, grating pair (150 ℓ/mm).

Fig. 3.4. Design of the pulse-front-matching apparatus.

Fig. 3.5. Comparison of the spatial chirp of the amplified signal centered at 600 nm in the horizontal direction. A center-of-mass wavelength is shown in both cases of the non-tilted (open squares) and tilted (full circles) pump geometries. The dashed line indicates the expected spatial chirp of the tilted signal in the former geometry. The solid curve is for an eye guide.

The design of the pulse-front-matching apparatus is shown in Fig. 3.4 in detail. The pump beam passes through an antireflection-coated 45° fused-silica prism with an incident angle of 49° for the pulse front to be tilted by 2.3°. A telescope ($f = 200 / 70$ mm) with the longitudinal magnification factor of 2.8 images the front with the tilt angle of 6.4° at the BBO located on the focal plane. Corresponding internal tilt angle of 3.7° (using $v_g/c = 0.575$ at 395 nm and $\theta = 31.5°$) being equal to α assures a maximum spatial overlap between them. Diameters of both beams at the BBO are about 1.5 mm (pump intensity ~50 GW/cm²). However, due to the mode mismatching and the non-uniform intensity across the pump beam, the signal is amplified only in the limited area (~0.5-mm diameter) up to a 3-μJ pulse energy. For the second-stage amplification, both pump and signal beams are reflected back to the crystal by spherical mirrors ($r = 100$ mm) located at the confocal positions and the same pulse fronts are reappeared and overlapped well each other again. The back-reflecting mirrors have slight vertical tilt-angles to extract the output at the mirror placed jus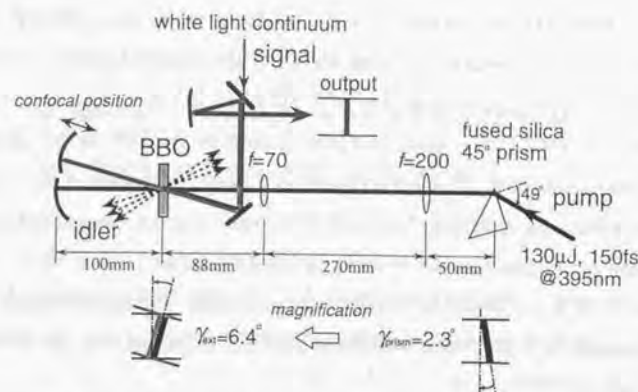t below the incident beam axis. A spherical mirror ($r = 500$ mm) compensates the small divergence of the beam. The final pulse energy is 5 μJ with the peak-to-peak fluctuation of 5–10 %. The signal can be tuned from 550 to 700 nm by scanning the delay line of the seed.

In Fig. 3.5 the spatial chirp of the amplified signal after the first-stage amplification is compared with that in a non-tilted pump geometry shown in Fig. 2.15(b). Both spectra are centered at 600 nm. The large chirp of the signal in the non-tilted pump case can be reasonably explained by the tilted signal generation, whereas the pulse-front-matched interaction dramatically reduces the spatial chirp. It strongly indicates the non-tilted signal amplification from the relationship of Eq.(2.21). In this way the spatial effect over the beam cross section is minimized, and only an appropriate pulse compressor leads to a TL pulse generation as follows.

The amplified signal then passes through a grating-prism compressor and the chirp is precisely eliminated across the tuning range. The pulse shape is measured by a fringe-resolved autocorrelator (FRAC). The following sections explain the details. The part of the idler is explained in Section 3.3.

3.2.2. Chirp Property of Signal

Because the seeded continuum has a chirp, the OPA is processed as a chirped-pulse amplification [89] and the amplified signal initially possesses the same chirp. In addition, the signal experiences the phase distortion caused by the nonlinear effect in the BBO and by the propagation through the dispersive media such as the crystal, air,

and the beam splitters in the FRAC. In order to attain a TL sub-10-fs pulse, an accurate phase correction is required over the wide spectral range.

The wavelength dependent phase $\phi(\omega)$ (ω: angular frequency) of the pulse is expanded around a center angular frequency ω_0 as

$$\phi(\omega) = \phi(\omega_0) + \left(\frac{d\phi}{d\omega}\right)_{\omega_0}(\omega - \omega_0) + \frac{1}{2}\left(\frac{d^2\phi}{d\omega^2}\right)_{\omega_0}(\omega - \omega_0)^2 + \frac{1}{3!}\left(\frac{d^3\phi}{d\omega^3}\right)_{\omega_0}(\omega - \omega_0)^3$$
$$+ \frac{1}{4!}\left(\frac{d^4\phi}{d\omega^4}\right)_{\omega_0}(\omega - \omega_0)^4 + \cdots. \qquad (3.4)$$

The distortion of the pulse shape is not caused by the dispersion of the phase velocity but by that of the group velocity. So that the group delay (GD) $T(\omega)$ given below is commonly used for pulse-propagation characterization:

$$T(\omega) = \frac{d\phi}{d\omega}$$
$$= \left(\frac{d^2\phi}{d\omega^2}\right)_{\omega_0}(\omega - \omega_0) + \frac{1}{2}\left(\frac{d^3\phi}{d\omega^3}\right)_{\omega_0}(\omega - \omega_0)^2 + \frac{1}{6}\left(\frac{d^4\phi}{d\omega^4}\right)_{\omega_0}(\omega - \omega_0)^3 + \cdots. \qquad (3.5)$$

The constant term induces only a temporal shift during the pulse propagation without any shape change and is thus eliminated in Eq.(3.5). The coefficients of the expansion $\phi''(\omega_0)$, $\phi'''(\omega_0)$, $\phi''''(\omega_0)$,... are called GD dispersion (GDD), third-order dispersion (TOD), fourth-order dispersion (FOD),..., respectively.

In the propagation through a medium with the path length l and wavevector $k(\omega) = n(\omega)\omega/c$, the phase shift is $\phi(\omega) = k(\omega)l$, yielding

$$T(\omega) = \frac{l}{v_g(\omega)}, \qquad (3.6)$$

which gives the intuitive representation of the GD. However, the concept of the GD can be also generally used for the optical systems with wavelength-dependent optical paths $P(\omega)$ such as a grating pair [90] or prism pair [91]. The GD of such systems can be given by

$$T(\omega) = \frac{d}{d\omega}\left(\frac{\omega P(\omega)}{c}\right). \qquad (3.7)$$

Because most of optical media have a positive GDD from the ultraviolet to near-
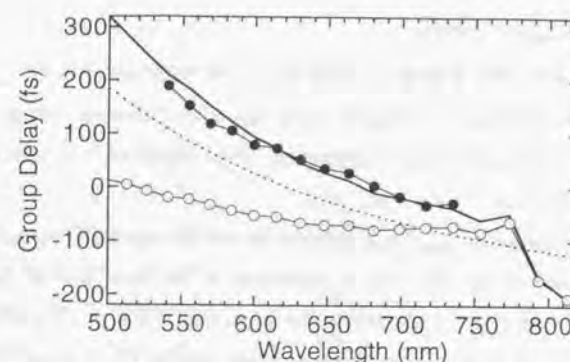
Fig. 3.6. Measured GD of the amplified signal centered at 630 nm (full circles). The thick solid line shows the sum of the GD of the seeded continuum (open circles) and that of the BBO with a net 2-mm thickness (dashed curve). The effect of air is corrected so that the GDs at the BBO position are presented. The wavelength of a zero-GD is arbitrarily chosen.

infrared (NIR) regions, the signal experiences positive chirp where the red portion of the pulse goes ahead the blue. However, as shown in Appendix A and B the use of refraction can give a negative contribution to the GDD, which enables the pulse compression [92]. In Chapter 2 we used a single prism pair for the compressor. However, because the higher terms such as a TOD and FOD become significant in a sub-10-fs regime with covering a broad spectral range, a more precise phase correction is needed for the compression to the TL.

Here the grating-prism compression is introduced to compress the signal pulses [18,93]. This method enables the simultaneous compensation of the GDD and TOD and is widely used in the sub-10-fs regime [18,20,30]. However, instead of the elimination of the terms of the GDD and TOD at the center frequency conventionally used, a global cancellation of the wavelength-dependent GD across the whole tuning range [21] is more convenient for the tunable pulse generation. This approach simplifies the compressor design and promises the best results. The requirement of the perfect compression is the constant GD *at the position* of the pulse-shape measurement apparatus, i.e.,

$$T_{\text{pulse}}(\omega) + T_{\text{compressor}}(\omega) = \text{const.,} \qquad (3.8)$$

where $T_{\text{pulse}}(\omega)$ is the GD of the pulse at the exit of the BBO crystal and $T_{\text{compressor}}(\omega)$ is the GD of the compressor including whole dispersive elements which the pulse encounters before the pulse-shape measurement. The compressor is designed to have a GD which satisfies Eq.(3.8) reasonably well.

Precise knowledge of $T_{\text{pulse}}(\omega)$ is required for the appropriate compressor design. A spectrally-resolved up-conversion is performed in the same way as used in the measurement of the chirp of the continuum in Section 2.3.1. A 10-μm-thick BBO crystal (the same one used in the autocorrelator, see Section 3.2.3) is used for the SFG with the gate pulses at 790 nm to minimize the additional dispersion. The measured GD is shown in Fig. 3.6. Also shown is the chirp of the continuum at the BBO after passing the thin high-pass filter. The effect of the dispersion of air is corrected. The sum of the continuum chirp and the dispersion of the BBO well explains the $T_{\text{pulse}}(\omega)$, which indicates the chirp conversion from the pump pulses or the nonlinear effects such as self-phase modulation (SPM) is weak enough and it is reasonable to be neglected.

The compressor is composed of a grating pair, a prism pair, air, and a 0.5-mm-thick broadband Cr-coated beam splitter in the FRAC (see the subsequent section). The beam-steering and focusing optics are composed of several overcoated silver mirrors and a few overcoated aluminum mirrors, the GD change of which is at most 1 fs per one reflection over the wide range of the visible [94] and is neglected hereafter. The gratings are used in the near-Littrow configuration with the small incident angle of 10° to increase the diffraction efficiency to about 60 % per one reflection. The blazed wavelength is 550 nm and the groove density is 150 ℓ/mm. The prisms are made of fused-silica with small apex angles of 45°. Such low dispersive thin prisms reduce the intraprism path length (IPL) and minimize the TOD error caused mainly by the dispersion of glass, and are advantageous for the broadband phase correction [21,24]. The prisms are arranged with the minimum deviation for the sake of the experimental convenience. The other parameters of the grating-prism compressor are

determined to best-fit Eq.(3.8). The GDs of the grating pair and prism pair are calculated by the dispersive ray-tracing analysis [93]. The wavelength-dependent diffraction, refraction, and refractive indices are taken into account and the accumulated path length $P(\omega)$ in Eq.(3.7) is evaluated. In the present case the results are expressed simply in analytical forms (see Appendix B).

Figure 3.7 shows the series of the GD of each element in the compressor at the optimal compression. The parameters are as follows: a 15-mm separation of the grating pair and 550-mm slant length and 3.4-mm IPL of the prism pair at 650 nm. The resultant path length of air is approximately 3 m. The 45° incidence of the beam onto the beam splitters in the FRAC is considered. The sum of the all contributions well compensates $T_{\text{pulse}}(\omega)$ substantially well (Fig. 3.7(e)). The throughput of the part of the grating-prism

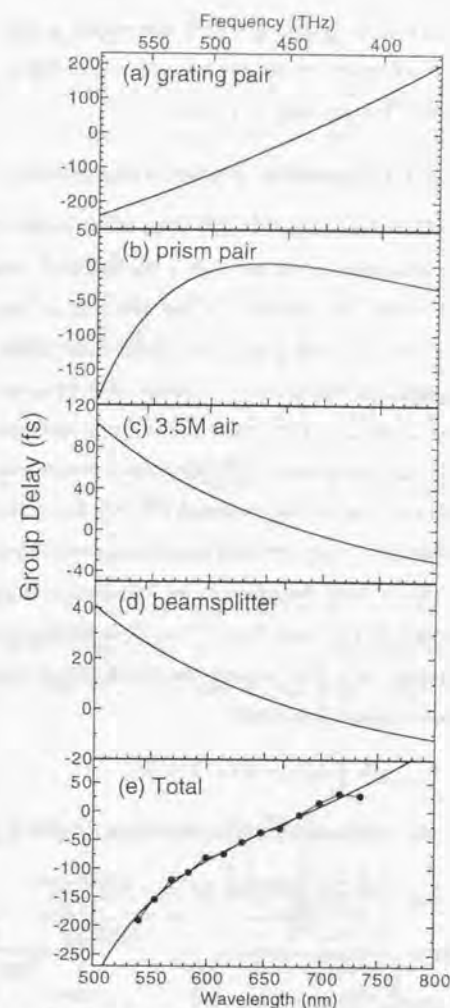Fig. 3.7. Wavelength dependence of the GD of each element in the compressor: (a) grating pair with a 15-mm separation, (b) prism pair with a 550-mm slant length and 3.4-mm intraprism path length at 650 nm, (c) air with a 3.5-m path length, and (d) 0.5-mm-thick beam splitter in the autocorrelator. The total GD of the compressor is shown in (e) with the measured GD with the signs inverted for fitting.

compressor is limited to ~10 % due mainly to the four reflections on the gratings. The eight reflections on the prism surfaces give fairly high throughput of ~80 % even by the non-Brewster-angle incidence.

3.2.3. Fringe-resolved Autocorrelator (FRAC)

The measurement of the pulse width shorter than 10 fs needs careful attentions. The background-free intensity autocorrelation used in Chapter 2 is less informative and suffers the problem of the geometrical smearing caused by the noncollinear interaction in analogous to the pulse-front tilting mentioned above. The details are discussed in Appendix C. A remarkable progress in measuring the pulse shape has been made in the last decade and versatile methods have appeared such as a frequency-resolved optical gating (FROG). The measurement of sub-10-fs pulses, however, still remains an up-to-date challenge [95,96], then in this experiment a reliable well-known method of a fringe-resolved (interferometric) autocorrelation technique is utilized [97].

In a FRAC the pulse to be measured is separated to two portions of the fields denoted by $E_1(t)$ and $E_2(t)$. When E_2 is delayed by τ and both beams are recombined coaxially in a SHG crystal, the FRAC signal given by the power of the frequency-doubled signal is given by

$$I_{FRAC}(\tau) = \int_{-\infty}^{\infty}(E_1(t) + E_2(t-\tau))^4 dt. \tag{3.9}$$

If both fields are identical to each other, $E_1(t) = E_2(t) = A(t)\cos(\omega t + \phi(t))$, we obtain

$$I_{FRAC}(\tau) = \frac{3}{4}[1 + 2G(\tau) + 2F_1(\tau) + F_2(\tau)], \tag{3.10}$$

where

$$G(\tau) = \int_{-\infty}^{\infty} I(t)I(t-\tau)dt, \tag{3.11a}$$

$$F_1(\tau) = \int_{-\infty}^{\infty} A(t)A(t-\tau)(I(t) + I(t-\tau))\cos(\omega\tau + \phi(t) - \phi(t-\tau))dt, \tag{3.11b}$$

$$F_2(\tau) = \int_{-\infty}^{\infty} I(t)I(t-\tau)\cos 2(\omega\tau + \phi(t) - \phi(t-\tau))dt. \tag{3.11c}$$

Here we use the intensity envelope function $I(t) = A^2(t)$ normalized as $\int I^2(t)dt = 1$. $G(\tau)$ is the intensity autocorrelation function. $F_1(\tau)$ and $F_2(\tau)$ are oscillating components with angular frequencies of ω and 2ω, respectively. Because $G(0) = 1$, $F_1(0) = 2$, and $F_2(0) = 1$, the well-known 1:8 ratio between the background and zero-delay signal is obtained. However, if the two beams are not identical, the correlation trace is distorted and this ratio cannot be obtained.

As an example, in the case of a TL hyperbolic secant envelope $A(t) \propto \text{sech}(t/T)$ with $\phi(t) = 0$, the pulse width is given by $1.763T$ and Eqs.(3.11a)–(3.11c) are

$$G(\tau) = \frac{3}{\sinh^2(\tau/T)}\left[\frac{\tau}{T}\coth\left(\frac{\tau}{T}\right) - 1\right], \tag{3.12a}$$

$$F_1(\tau) = \frac{3}{\cosh(\tau/T)\tanh^3(\tau/T)}\left[\tanh\left(\frac{\tau}{T}\right) - \frac{\tau}{T}\text{sech}^2\left(\frac{\tau}{T}\right)\right]\cos\omega\tau, \tag{3.12b}$$

$$F_2(\tau) = G(\tau)\cos 2\omega\tau. \tag{3.12c}$$

The schematic of the low dispersive FRAC constructed in the present work is shown in Fig. 3.8. Both arms are perfectly balanced by using two identical beam splitters, which are arranged in anti-parallel with each other so that both reflections
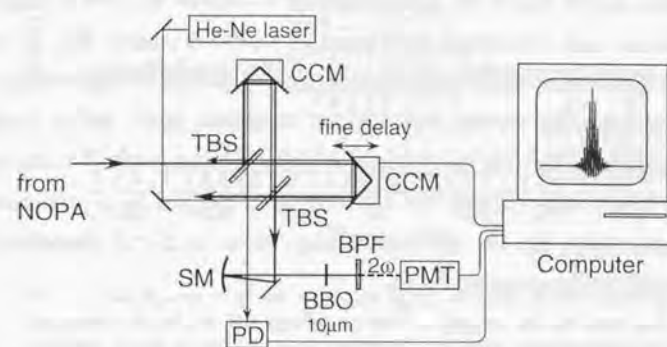

Fig. 3.8. Schematic of the fringe-resolved autocorrelator. TBS, thin 0.5-mm-thick beam splitter with Cr-coating; CCM, corner-cube mirror; SM, spherical mirror ($r = 300$ mm); BPF, bandpass filter; PMT, photomultiplier; PD, photodiode.

occur at the same air-coating interfaces. The intensities and material dispersions are then perfectly equalized and a precise autocorrelation trace given by Eq.(3.10) is obtained. The thin coating of chromium exhibits the almost constant 30 ± 1-% reflectance and transmittance in a wide range between 500 and 800 nm without any polarization dependence. The GD originating from the coating can thus be neglected. The substrate is made of B7 with a 0.5-mm thickness: this is almost the minimum thickness which does not suffer from bend during coating process and allows the accurate measurement of the interference pattern. The reflectors in both arms are corner-cube mirror assemblies. The delay line is driven by an ultra-fine pulse stage (Suruga-Seiki, R10-80L) with the minimal step of ~20 nm, corresponding to the time step of approximately 0.07 fs. The time axis is on-line calibrated with a He-Ne laser, the beam of which is aligned to propagate in the opposite direction to the signal beam [20,21]. The calibration is done by the cosine function fitting to the partial data including one-period fringe around each position.

The recombined beam is focused by an r = 300-mm spherical mirror onto a doubling crystal with the folding angle of 3° to minimize the astigmatism. An ultra-thin 10-μm-thick BBO crystal (EKSMA; type I, θ = 45°, ϕ = 0°) is used for the doubling crystal to minimize the group-velocity mismatch (GVM) between the fundamental and SH. The GVM of only 4 fs at 600 nm enables the accurate acquisition of the second-order correlation signal even in a sub-5-fs regime [98]. A careful attention should also be taken for the bandpass filter: a specially designed filter is used here to minimize the filtering effect of the correlation signal and to block the fundamental effectively. The transmittance is 70 ± 10 % between 280 and 380 nm and less than 0.5 % across 500 to 780 nm. The SH is detected by a photomultiplier (Hamamatsu, H957-01) and the He-Ne fringe is by a Si-PIN photodiode. All measurements are computer-controlled.

3.2.4. Tuning Property

A typical FRAC trace of the signal at the optimal compression at 630 nm is shown in Fig. 3.9. The ratio 1:8 is obtained which indicates the precision of the system. Also

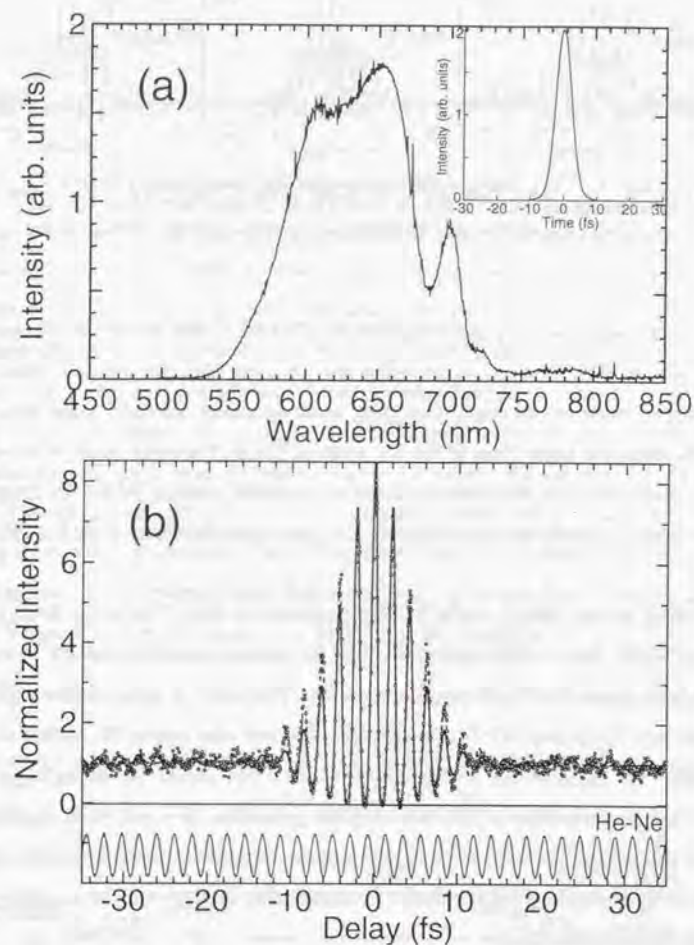Fig. 3.9 (a) Spectrum of the amplified signal centered at 630 nm. The bandwidth is 100 nm. The inset shows the TL intensity profile with 5.6-fs FWHM. (b) Fringe-resolved autocorrelation trace. Measured (open circles), sech^2-fit (dashed curve), and TL (solid curve) traces are shown. The sech^2-fit pulse width is 6.2 fs. At the bottom shown are the He-Ne fringes used for the time-axis calibration.
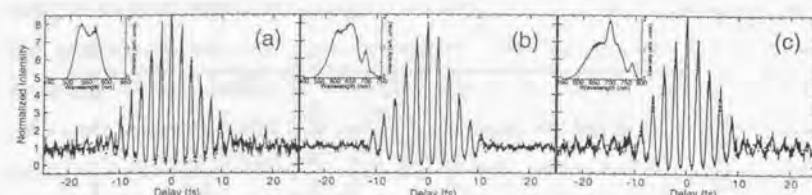
Fig. 3.10. FRAC traces of the signal across the tuning range. The sech²-fit (dashed curves) pulse widths are (a) 7.1 fs at 550 nm, (b) 6.2 fs at 620 nm, and (c) 6.1 fs at 690 nm. Each intensity-calibrated spectrum is shown in the inset.

shown is the corresponding spectrum with the FWHM of 100 nm and its TL intensity profile obtained by Fourier-transforming the spectrum with the constant phase. The spectrum is intensity-calibrated. The pulse width assuming the sech²-shape is as short as 6.2 fs, which is fairly close to the TL width of 5.6 fs. The pulse duration is reduced to less than half from that obtained from a non-tilted pumped NOPA in Chapter 2, which indeed presents the importance of the pulse-front matching in such a sub-10-fs regime.

Tuning is very simply performed by scanning the delay line at the fixed crystal angle of 31.5°. Only a slight optimization of the grating separation and IPL is needed. Figure 3.10 shows the FRAC traces and spectra. The sech²-fit pulse widths at 550 and 690 nm are 7.1 fs and 6.1 fs, respectively, and are also nearly TL within a 20-% deviation. The pulse energy is almost constant to 0.5 μJ across the tuning range. This is the first demonstration of the tunable pulse generation in a sub-10-fs regime. The current throughput (~10 %) of the grating-prism compressor limits the pulse energy, which is to be improved dramatically by introducing chirped mirrors in place of the grating pair (Section 3.4).

3.3. Tunable Sub-10-fs Pulse Generation in the Near-infrared

3.3.1. Idler Angular-dispersion Compensation

The idler is generated with a large spectral angular dispersion to be phase-matched with the broad spectrum of the signal (see Fig. 2.10, Photograph II). This is a characteristic property of the group-velocity matched NOPA between the signal and idler as discussed in Chapter 2. While the achromatic phase matching in up-conversion such as SHG requires a precise optical design to prepare the angular dispersion of the incident beam [75,76], in the present down-conversion the achromatism is attained automatically. Because the bandwidth of the idler should be the same as that of the signal, a sub-10-fs pulse generation is also expected in the NIR.

In order to obtain the collimated idler beam, only an angular-dispersion compensator after the crystal is required. Figure 3.11 shows the scheme of a Martinez-type telescope-grating compensator conventionally used [70]. The crystal and the grating are respectively placed at the objective and image focal planes of the telescope. The dispersion of the external noncollinear angle $\beta_{ext}(\lambda_i)$ of the idler is then magnified by the longitudinal magnification factor $M = f_1/f_2$ at the grating as

$$M\frac{d\beta_{ext}}{d\lambda_i} = \frac{d\theta_i}{d\lambda_i},\qquad(3.13)$$

where $\theta_i(\lambda_i)$ is the incident angle onto the grating. The diffracted angle $\theta_o(\lambda_i)$ is

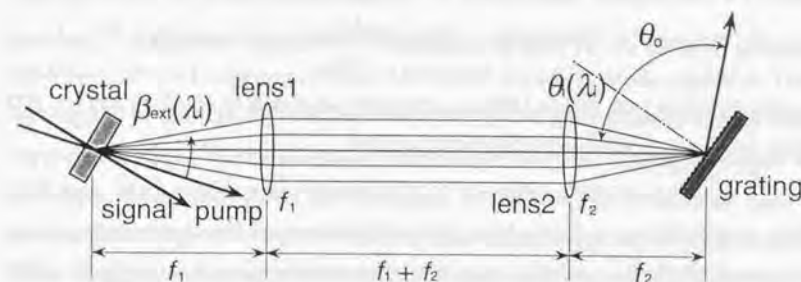
Fig. 3.11. Basic schematic of the angular-dispersion compensation.

obtained by the grating equation for the first-order diffraction:

$$\sin\theta_o(\lambda_i) - \sin\theta_i(\lambda_i) = b\lambda_i, \tag{3.14}$$

where b is the groove density. Differentiating Eq.(3.14) yields

$$\cos\theta_o \frac{d\theta_o}{d\lambda_i} - \cos\theta_i \frac{d\theta_i}{d\lambda_i} = b. \tag{3.15}$$

The elimination of the angular dispersion in the diffracted beam ($\frac{d\theta_o}{d\lambda_i} = 0$) is thus attained when

$$\frac{d\theta_i}{d\lambda_i} = -\frac{b}{\cos\theta_i(\lambda_i)} \tag{3.16}$$

over the whole spectrum. By substituting Eq.(3.13), the condition required for the angular-dispersion compensator is obtained as

$$M\frac{d\beta_{eo}}{d\lambda_i} = -\frac{b}{\cos\theta_i(\lambda_i)}. \tag{3.17}$$

Both sides of the above equation are expanded to Taylor series' around the center wavelength λ_{ic} and the equalization of the first term yields

$$M\left(\frac{d\beta_{ext}}{d\lambda_i}\right)_{\lambda_{ic}} = -\frac{b}{\cos\theta_i(\lambda_{ic})}. \tag{3.18}$$

This condition can be fulfilled by selecting the parameters of the telescope, groove density, and incident angle onto the grating. As discussed in Section 2.3.2, $\beta_{ext}(\lambda_i)$ features a characteristic highly-linear wavelength-dependence at the group-velocity-matching point for $\alpha = 3.7°$ and the coefficient $\frac{d\beta_{ext}}{d\lambda_i}$ is 0.279 mrad/nm at 1.1 μm with a small deviation from 800 to 1400 nm. Thus the parameters of $M = 2.17$ and $b = 600$ ℓ/mm used here can satisfy Eq.(3.18) at $\theta_i = \pm 8.4°$.

In the present NOPA, however, the bandwidth is amounting up to more than 3000 cm^{-1} and cares must be taken about the validity of the compensation. In an achromatic SHG the quadratic term of a phase-matching curve is generally much larger than that of the grating diffraction and gives the limitation of the bandwidth
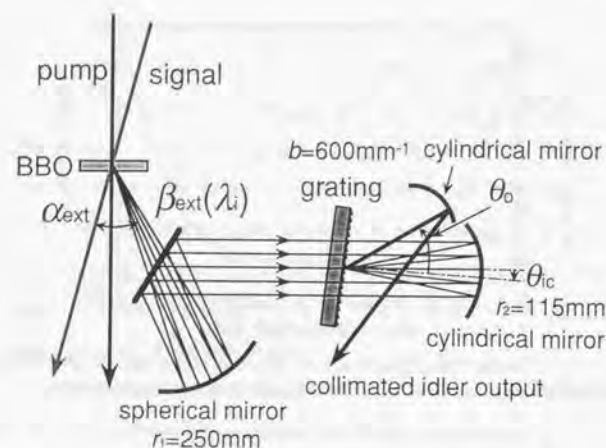
Fig. 3.12. Idler angular-dispersion compensator.

[70,71]. The enhancement of this quadratic term is recently demonstrated by using a "grism", which is the combination of a prism and a transmitting-type grating [75]. However, in our NOPA the signal-idler group-velocity matching realizes the highly linear dependence and thus the nonlinear diffraction of the grating itself limits the bandwidth. The aberration of the spherical optics is also must be taken into account because the spectrum is widely spread over the dimension of the mirrors and the paraxial-ray approximation is invalid, resulting in a chromatic distortion at the exit causing a wavelength-dependent GD. These factors are carefully estimated by a dispersive ray-tracing analysis as follows.

An all reflective-type angular-dispersion compensator is designed for the broadband sub-10-fs operation. Figure 3.12 shows the details of the apparatus. They are aligned so that the ray-component at 1100 nm is back-reflected with a small vertical tilt angle, which minimizes astigmatism. The rays are again aligned to propagate horizontally before the incidence to the grating. Because the idler is generated from the BBO with a small divergence vertically, an $r = 250$-mm spherical mirror recollimates the idler in both vertical and horizontal directions, while an $r = 115$-mm cylindrical mirror focuses it horizontally on the grating. The corresponding
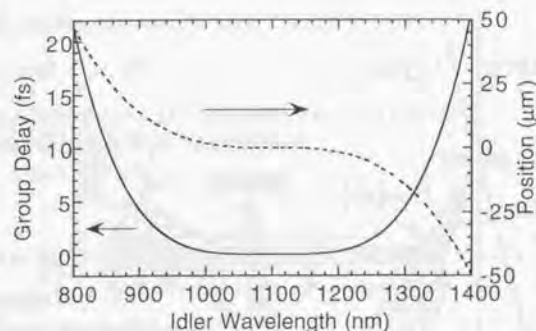
Fig. 3.13. Wavelength dependence of the GD (solid curve) and lateral walk-off (dashed curve) of the collected idler at the grating position.
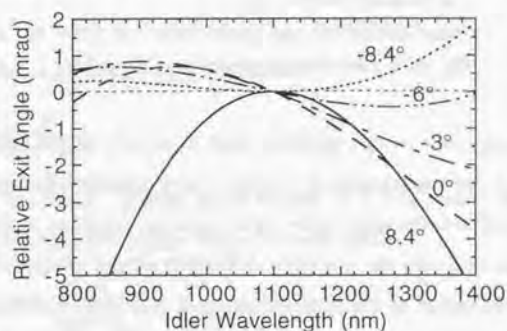
Fig. 3.14. Wavelength dependence of the relative exit angle with respect to $\theta_0(1100 \text{ nm})$ at various incident angle $\theta_i(1100 \text{ nm})$.

magnification factor M is 2.17 as mentioned above. The visible non-phase-matched SH coaxially generated from the BBO can be used for the total alignment.

The ray-tracing analysis is straightforward in such a reflective optical system: each ray-component at λ_i is emitted from the crystal position to the direction with $\beta_{ext}(\lambda_i)$, and the geometrical reflections at mirrors and the grating diffraction according to Eq.(3.14) are calculated. The effect of the beam divergence is neglected for simplicity. The small astigmatism in the vertical direction is also neglected. The astigmatism in the horizontal plane plays a dominant role in the distortions and is carefully computed. We assume the system is aligned correctly as shown in Fig. 3.12

and the standard 1100-nm ray is propagated along the center axis.

Figure 3.13 shows the calculated GD and lateral position of each wavelength component at the grating position (on the image plane) after passing through the telescope. The wavelength-dependent feature originates from the aberration. Because the beam diameter of the idler in the BBO is estimated to be ~500 µm, the horizontal size of the idler beam on the grating is calculated to be reduced by M^{-1} to 230 µm. The lateral walk-off is thus within 20 % of the output cross section which may be negligible. The GD shows the dependence of a fifth-order dispersion and the ~20-fs delay increase is induced at the both sides.

The angular dispersion of the first-order diffraction depends on the rotating angle of the grating. The wavelength dependence of the exit angle is calculated when $\theta_i(1100 \text{ nm})$ is changed around the two solutions $\pm 8.4°$ of Eq.(3.18). As shown in Fig. 3.14, at both solutions the angular dispersion is completely eliminated at 1100 nm. However, a larger dispersion remains outside the solution. This fact originates from the large diffraction nonlinearity of the grating and not from the aberration. For the tunable sub-10-fs generation, a global suppression of the dispersion across the whole spectral range is pursued. Figure 3.15 shows the best result obtained in the case of
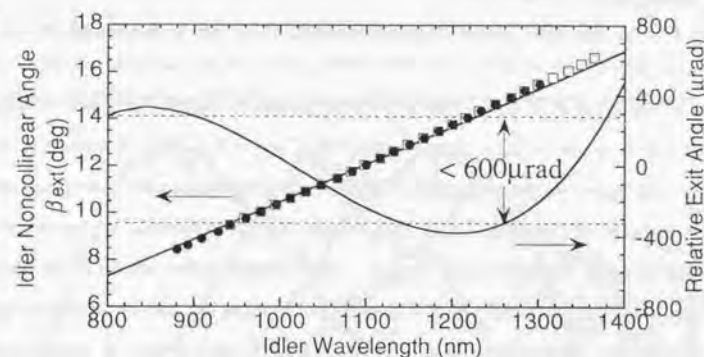

Fig. 3.15. Angular-dispersion properties of the idler. The large dispersion of β_{ext} at the exit of the BBO (calculated (solid curve) and measured (full circles at $\lambda_s = 680$ nm and open squares at $\lambda_s = 600$ nm)) is best suppressed by the compensator with the incident angle $\theta_i(1100 \text{ nm}) = -7°$. The zero exit angle corresponds to $\theta_o = 32.6°$.

$\theta_i(1100 \text{ nm}) = -7°$, where the angular distribution of the first-order diffraction is well suppressed within 600 μrad from 800 to 1400 nm. Thus the idler can be tuned without any readjustment of the system. This grating angle is used henceforth.

Actually there is an effect of the horizontal wave-diffraction due to the confinement of the beam diameter. An additional cylindrical mirror ($r = 77.85$ mm) is used after the grating for the horizontal collimation. The output beam pattern is rectangular due to the different magnification coefficients of the telescope between the vertical and horizontal direction. The pulse energy of the collimated beam is about 1 μJ, which is limited mainly by the diffraction efficiency (~60 %) of the grating blazed at 1000 nm.

3.3.2. Chirp Property of Idler

The spectra of the collimated idler after passing through the angular-dispersion compensator are shown in Fig. 3.16. The continuous tuning is attained from 900 to 1300 nm corresponding to the signal tuning from 700 to 560 nm. The FWHM amounts up to 200 nm. The bandwidth is ~20 % narrower than that expected from the signal, which is mainly caused by the relatively narrowband diffraction efficiency of the blazed grating in the compensator.

The GD of the idler pulses centered around 1100 nm is measured by an up-
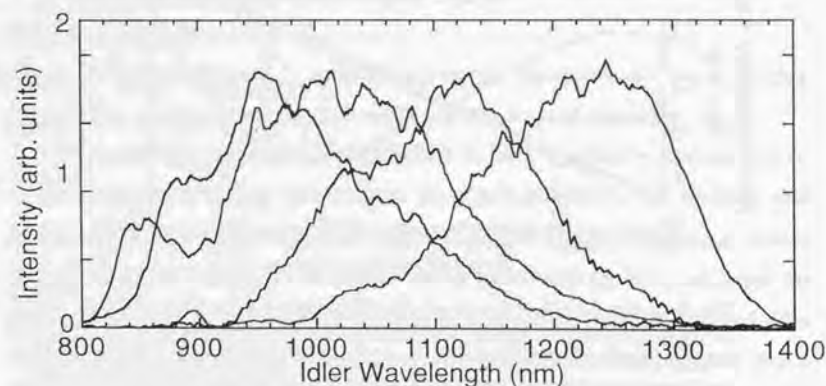
Fig. 3.16. Spectra of the idler.
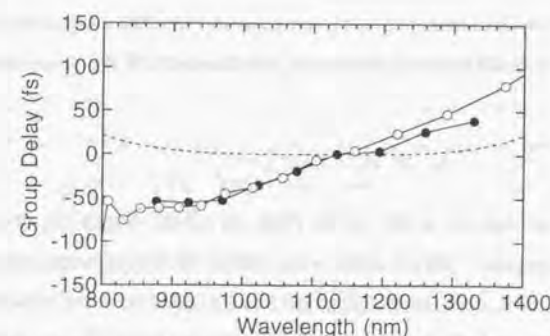
Fig. 3.17. GD property of the idler. The measured (full circles), predicted (open circles), and the GD of the angular-dispersion compensator (dashed line) are shown. In the measured GD the effect of air is corrected.

conversion similarly in the case of the signal and is shown in Fig. 3.17. A 100-μm-thick BBO crystal (type I, $\theta = 45°$) is used for the SFG with the 790-nm gate pulses. The effect of air is corrected. The result presents the characteristic negative chirp property. This is well understood by the parametric interaction between the signal and idler.

As a basic property of the three-wave interaction the relative phase

$$\theta_r = \Delta k \cdot z + \phi_p - \phi_s - \phi_i \qquad (3.19)$$

determines the direction of the energy flow between the three waves [83]. Here Δk is the phase mismatch along the direction of the pump z and ϕ_j is the phase of the j-th wave, respectively. When $\theta_r = +\pi/2$, the pump energy is increased with the reduction of the energies of the signal and idler (SFG). On the other hand, when $\theta_r = -\pi/2$, the pump energy is converted to the signal and idler (OPA). The relative phase is maintained to be the either values under the case of a two-wave input, which means the generated wave has the phase to satisfies $\theta_r = \pm\pi/2$. The sign is determined by the intensity ratio. In case of monochromatic waves the phase matching can be completely satisfied and the phase relation of the three waves are locked through the propagation.

In the case of femtosecond pulses with broad spectra, however, the GVM dominates the interaction as discussed in Chapter 2. In the monochromatic pump

approximation the first-order phase mismatch around the center signal frequency ω_{s0} is described by the GVM between the signal and idler and the relation which should be satisfied is

$$GVM_{s-i} \cdot (\omega_s - \omega_{s0}) \cdot z + \phi_p - \phi_s(\omega_s) - \phi_i(\omega_i) = -\frac{\pi}{2}, \qquad (3.20)$$

where GVM_{s-i} is defined in Eq.(2.16). Thus the GVM causes the phase variation through the propagation. On the signal-idler group-velocity matching condition in the present work, $GVM_{s-i} = 0$, so that this variation is eliminated and the phase relation between the signal and idler is locked. By differentiating Eq.(3.20) we obtain

$$T_i(\omega_i = \omega_p - \omega_s) = T_s(\omega_s), \qquad (3.21)$$

and

$$\frac{d^2\phi_i}{d\omega_i^2} = -\frac{d^2\phi_s}{d\omega_s^2}, \frac{d^3\phi_i}{d\omega_i^3} = \frac{d^3\phi_s}{d\omega_s^3}, \qquad (3.22)$$

where $d\omega_i = -d\omega_s$ is used. Therefore the chirp of the idler can be simply determined by the seed chirp so that the idler compensates the seed chirp. The positive GDD and TOD of the signal give the negative GDD and positive TOD of the idler, respectively. Piskarskas *et al.* investigated this phenomena in the case of picosecond pulses and they called it as "chirp reversal" [99].

The GD of the signal at the exit of the BBO is the sum of the GDs of the seed chirp and BBO. Considering the additional GD caused by the angular-dispersion compensator, the predicted GD of the idler is calculated and shown in Fig. 3.17. The agreement is well within the limited time resolution. Thus in the present experiment the chirp reversal dominantly determines the chirp of the idler. Note that Eq.(3.20) assumes the chirp-free (monochromatic) pump condition and no higher-order effect. Thus this result in turn supports the assumption that the higher-order nonlinear effects are weak enough, as expected from the assignment of the signal chirp (see Fig. 3.6).

3.3.3. Pulse Compression

It is a problem to design a pulse compressor which has the GD property with a positive GDD and negative TOD in order to cancel the idler chirp. A grating pair in the stretcher geometry [100] has these signs, but it seems to be impractical because of the low efficiency and difficult alignment. Materials generally have zero GDD points around the spectral region from 1100 to 1500 nm and at the longer wavelength the GDD becomes negative while the TOD maintains positive. Because the refraction only contributes to a negative GDD, a prism pair generally cannot give a large positive GDD. However, owing to the small GDD of the idler, we can find the optimum condition where the chirp can be compensated from 900 to 1300 nm. A ray-tracing analysis is used for the optimization of both proper material and configuration (see Appendix B). It is concluded that a highly dispersive SF10 prism with a 60.2° apex angle used with the minimum deviation can yield the best result.

Figure 3.18 shows the GD of the compressor which is composed of a prism pair, air, and a beam splitter in the FRAC. The contribution of mirrors is neglected again. The parameters are as follows: a 70-mm slant length and 4-mm IPL of the prism pair at 1100 nm and a 1.5-m path length of air. The configuration of the prism compressor is shown in Fig. 3.3. The overall adjustment of the idler beam in the compressor and FRAC is done by use of the visible SH with an increased IPL before the best compression. The SH is then perfectly eliminated by decreasing the IPL to the
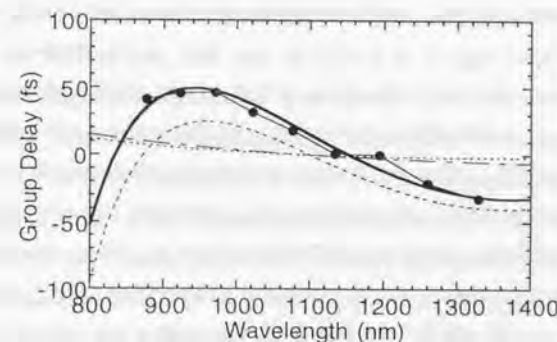

Fig. 3.18. GD property of the compressor. The GDs of the total compressor (solid curve), prism pair (dashed curve), air with a 1.5-m path length (dashed-dotted curve), and beam splitter in the FRAC (dotted curve) are shown. Also shown is the measured GD of the idler (full circles) with the sign reversed.
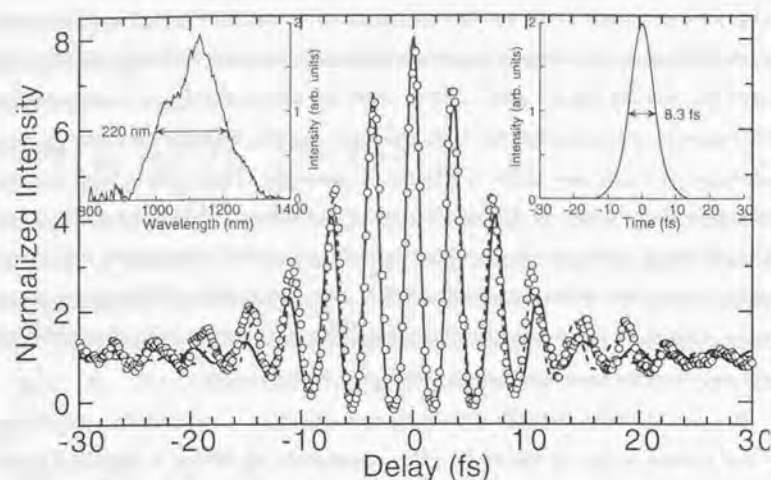
Fig. 3.19. FRAC trace of the idler at 1100 nm. The measured (open circles), calculated TL (solid curve, 8.3 fs) and $sech^2$-fit (dashed curve, 8.4 fs) traces are shown. The spectrum and TL intensity profiles are shown in the insets at the upper left and upper right, respectively.

optimum value. No filter is used for the separation of the idler and SH in order to minimize the phase distortion.

A FRAC trace is measured by the same autocorrelator shown in Fig. 3.8. Here a 100-μm-thick BBO (type I, $\theta = 45°$) for the SHG and a PMT for the visible (Hamamatsu Photonics, H957-06) are used. Two different bandpass filters (HOYA, HA30 and a thin cut-of filter identical to that used in the seed beam) are used for the sufficient flat transmittance of < 0.5 % for λ > 750 nm and > 80 % for λ < 750 nm.

The FRAC trace of the compressed pulse at 1100 nm is shown in Fig. 3.19. The $sech^2$-fit pulse width is as short as 8.4 fs. This is fairly close to the TL width of 8.3 fs determined by the spectrum. We believe this is the first report of the sub-10-fs pulse generation in the NIR longer than 1000 nm. By tuning the signal to the shorter wavelength the idler is tuned to the longer and the pulse width is maintained well below 10 fs. At 1250 nm the pulse width is 9.0 fs, however, the amplitude ratio suffers a slight degradation from 1:8. This may be due to the insufficient positive GDD of the

compressor for the compensation at a longer wavelength (see Fig. 3.18).

The longer pulse width of the idler than that of the signal is mainly due to the spectral narrowing caused by the grating and partly to the residual angular dispersion (Fig. 3.15). The tilt mismatch of the idler in the BBO seems to be less effective because of the intrinsic large angular dispersion. Optimization of the system will also provide sub-7-fs pulses in the NIR.

3.4. Sub-5-fs Pulse Generation

3.4.1. Toward Full-bandwidth Operation

So far the tunable pulse generations have been investigated by scanning the seed delay owing to the intrinsic chirp of the seed. Only the spectral components of the continuum overlapping with the pump can be amplified, resulting in the automatic spectral filtering. However, the shortest pulse generation using the overall bandwidth is also to be a marked challenge. The recently reported sub-5-fs pulse generations were attained by a continuum compression of a Ti:sapphire laser [20,21,23,24,25], the spectra of which are mainly located in the NIR and limit the versatile spectroscopic applications. The NOPA is expected to overcome these restrictions and lead to a new regime in ultrafast science.

It is straightforward to achieve the full bandwidth of 160 THz determined by the phase matching (see Fig. 2.6): the chirp rate must be small enough for all the spectral components in the bandwidth to encounter the pump pulses in a BBO crystal. Cerullo *et al.* could satisfy this requirement by decreasing the material amount before the crystal and obtain a 180-THz bandwidth [65]. In the present work we use a thicker sapphire glass (2 mm) for the stable continuum generation and a cut-off filter before the BBO to suppress the amplification of the intense spike at 790 nm. The resultant GD difference ΔT is ~80 fs between 530 and 770 nm, and then increased through the BBO crystal by $\Delta T_{BBO} = 231$ fs over the net 2-mm thickness (see Fig. 3.6). The condition for the full bandwidth through the two-stage amplification is roughly

estimated to be

$$\Delta T + \Delta T_{BBO} < \frac{\tau_P}{2} + \left(GVM_{p-s}\right)_{MAX},\qquad(3.23)$$

where τ_p is the pump duration of 150 fs and the maximum GVM between the pump and signal is 206 fs/mm at 770 nm. Thus the initial GD difference is needed to be less than 50 fs.

This requirement is attained by pre-compressing the seeded continuum by some pulse compressor [101]. In the former sections we have utilized a prism pair and a grating pair for compression over the wide spectral range. However, much more useful compressor with advantageous properties such as a maintenance-free operation, compact dimensions, and the highest throughput is to be requested. The recently progressed chirped-mirror technology [102] seems the most promising to satisfy these demands. In 1990s this technology has been widely applied to mode-locked Ti:sapphire lasers [13,14], other solid-state lasers [103], chirped-pulse amplifiers [25], optical parametric oscillators [104], and continuum compressions [20,21,23,24,25]. However, most of the applications are operated in the 800-nm region and the applicability of this technology in the higher frequency visible range with the broad bandwidth still remains an up-to-date work. We next go on to quest this subject and sub-5-fs pulses with the highest energy from the NOPA are pursued.

3.4.2. Design of Ultra-broadband Chirped Mirror

The idea of a chirped mirror to control femtosecond pulses was firstly suggested and demonstrated to a CPM dye laser by Yamashita *et al.* in 1986 [105]. The schematic is shown in Fig. 3.20. By modulating the multilayer period during the deposition, a quasi-quarter-wave dielectric coatings with varied Bragg wavelength is fabricated. An incident wavepacket of a given center wavelength is most efficiently reflected at the corresponding quarter-wave stack, so that the field penetration depth becomes wavelength-dependent and the GD can be controlled. If the Bragg wavelength is varied from the shorter wavelength to longer one from the air surface to the substrate side, a negative GDD is achieved. In 1994 Szipöcs and his coworkers
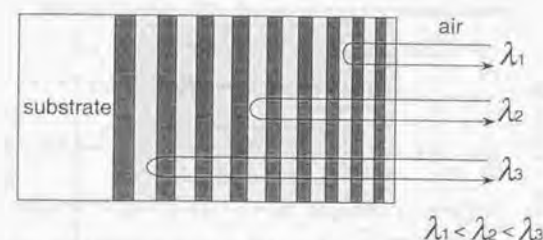
Fig. 3.20. Schematic of the basic design of chirped mirrors. The normal case of a negative GDD is shown. The thick and thin gray regions indicate the layers of materials with higher and lower refractive indices, respectively.

have shown that an extensive computer optimization of a multilayer design can provide a highly-controlled GD over a broad bandwidth [106], originating the recent wide use of chirped mirrors.

Intuitively for a constant GDD (linear variation of GD) a linearly-chirped multilayer periods seem the best configuration. However, the GDD is strongly perturbed by emergence of Fabry-Perot-like resonances inside the structures, resulting in non-negligible oscillations. For the quest of the smooth GD variation over a broad bandwidth, it is essential to introduce an optimized modulation in the chirped multilayer periods with both of the phase and amplitude [107]. It is not suitable to increase the total number of layers to control the GD over a broader bandwidth, because the more precision of the deposition is required with the undesired higher stress in such coatings. Thus an elegant design of a multi-layer system with a limited number of layers (~50) and insensitivity to a deposition error is especially to be quested for the broadband operation, especially in the present visible region with the larger dispersion of the layer materials than in the NIR region.

The chirped mirrors presented here are all designed and manufactured by Mr. M. Takasaka in Central Research Laboratory, Hamamatsu Photonics. The specific designs composed of alternating 40 layers of TiO_2 and SiO_2 are obtained by a simulated

Fig. 3.21. Wavelength dependence of the GDs of (a) UBCM-A and (b) UBCM-B per one reflection. Measured (solid curves) and designed (dashed curves) GDs are shown. Also shown is the transmittance of each mirror (dotted curve).

annealing method [108], which refines the transmittance, reflectance, and phase changes upon reflection of multilayer systems. Mirrors were manufactured under several kinds of designs but for the compressor only two of them are finally used and described here with the marks of UBCM-A and UBCM-B. The UBCM-A was designed 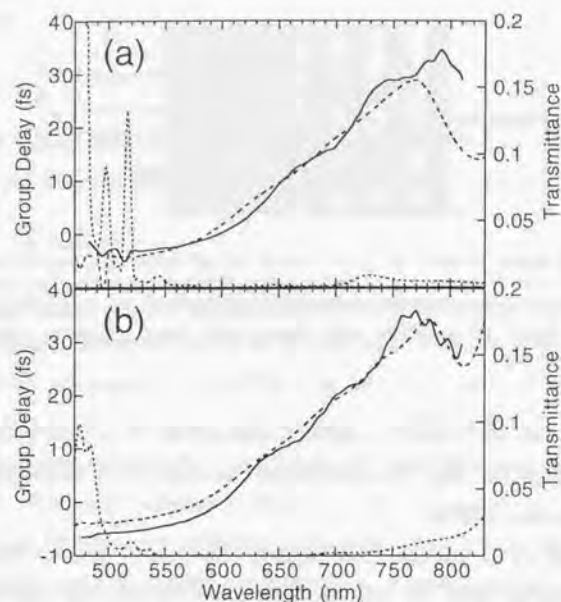to exhibit a GD property with several reflections to compensate the chirp of the NOPA output with the combination of the 45° prism pair, air, and the beamspiltter (see Fig. 3.7) all over the gain bandwidth from 480 to 760 nm. The UBCM-B was designed to have a GDD and TOD with -45 fs^2 and 20 fs^3, respectively, with the spectral region from 500 to 780 nm. In addition, both of them also have the high reflectivity ($R > 99\%$) in their bandwidths. Even with the different target functions, the optimization is resulted in similar behaviors of the GD as shown in Fig. 3.21. The

decrease of the GDD at the shorter wavelength is a general feature of chirped multi-layer systems, which is mainly determined by the ratio of the refractive indices of the layer materials. The UBCMs were fabricated by electron-beam evaporation.

3.4.3. Group-delay Measurement by White-light Interferometry

The measurement of the GD property of the manufactured UBCMs is essential for the precise phase correction of the NOPA output. There have been proposed several methods to measure GDs of optical elements by use of a white-light interferometry [109] such as a fringe-contour technique [94,110], Fourier-transform correlation [111], phase-locked interferometry [112], and Fabry-Perot interferometry [113]. For the simple and precise measurement, however, a one-shot type measurement is desirable. Here the GD was measured by a spectrally-resolved white-light interferometry which Kovács *et al.* reported in 1995 [114] and is widely used.

The schematic of the experimental setup is shown in Fig. 3.22. The fiber-transmitted white light from a tungsten lamp is collimated by lenses and injected into a Michelson interferometer. The spatial coherence of the light is increased by the small apertures. The beams are split to the reference and sample arms and are back-reflected
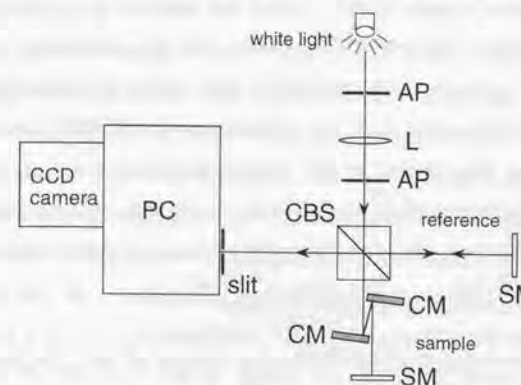

Fig. 3.22. Schematic of the spectrally-resolved white-light interferometry for the GD measurement. AP, aperture; L, collimating lens; CBS, cube beam splitter; CM, chirped mirrors; SM, over-coated silver mirror; PC, polychromator.
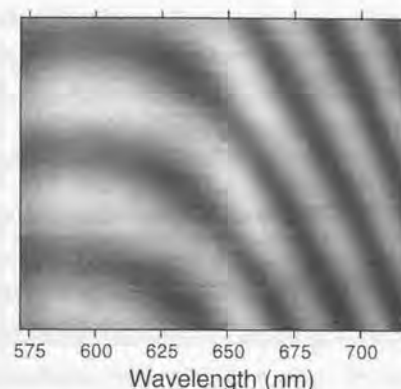
Fig. 3.23. Spectrally-resolved interference pattern of a UBCM-A pair. The dispersion is increased by four reflections.

Fig. 3.24. Property of the UBCM pair used for the pulse compressor. The GD (solid curve) and GDD (dashed curve) per one reflection are shown..

by identical overcoated silver mirrors with a negligible dispersion. In the sample arm two identical UBCMs are incorporated in parallel and reflect the white light with the incident angle of ~5°. The phase shift by the reflection on the dielectric multilayers are thus accumulated four times. If one of the end mirrors are slightly tilted in the vertical direction, the recombined beam has horizontal fringes, which is then spectrally dispersed in a polychromator (SPEX, 270M) and detected by a digital CCD camera (Hamamatsu, C4742, 1000(H)×1018(V) pixels). The two-dimensional image includes the interference pattern at each wavelength from which the wavelength-dependent phase shift $\phi(\omega)$ originating from the reflection on the UBCMs can be calculated. Though the term proportional to the angular frequency ω cannot be determined because of the uncertainty of the zero position, the resultant constant component of the GD has no effect on the properties of femtosecond pulses and thus the GD $T(\omega) = \dfrac{d\phi}{d\omega}$ can be calculated straightforwardly.

A typical spectrally-resolved interference pattern of the UBCM-A on a CCD camera is shown in Fig. 3.23. The parabolic feature of the fringe curves clearly indicates the negative GDD. The inhomogenity of the illumination caused by the spectral sensitivity of the camera, spectral variation of the tungsten lamp, and any

other possible contributions are removed by normalization, and then at each wavelength the fringe pattern is fitted by a cosine function and the phase is extracted. $T(\omega)$ is calculated by fitting the phase to a cubic-polynomial function over a 10-nm range around ω, and then divided by the reflection number four. The precision of the GD is less than 0.5 fs.

The measured GD and transmittance of the UBCM-A and UBCM-B are shown in Fig. 3.21 (a) and (b), respectively. Each of them indicates fairly high reflectivity larger than 99 % and nearly linear GD with the appropriate variance between 550 and 750 nm, as designed. There are a few oscillations across the whole spectral range, which are not predicted from the calculation and may originate from a deposition error. These oscillations are not negligible for the application to the compression to a sub-5-fs regime. In fact the pulse shortening to less than 8 fs is impossible by use of the same type of mirrors in place of a grating pair. Because the oscillations have the opposite phase between the UBCM-A and B, mainly due to the difference of the designed bandwidth, pairing these two mirrors effectively eliminates the oscillations as shown in Fig. 3.24. The GDD is -40 ± 15 fs^2 per one reflection between 600 and 700 nm and

has appropriate dependence on wavelength between 550 and 750 nm to correct the phase over the ultra-broadband spectrum. This kind of cancellation of the undesired structures by use of different chirped mirrors is essential in such a broadband operation for the shorter pulse generation [115].

3.4.4. Compression to a Sub-5-fs Regime

The GD compensation of the signal pulses using the above UBCMs is performed with the combination of a 45° fused-silica prism pair, air, and the beam splitter, as is in Section 3.2. By the global optimization to satisfy Eq.(3.8) across the whole spectral range, the best compression is attained in the case of a 1-m slant length and a 6.0-mm IPL of the prism pair at 650 nm and four round trips (eight reflections) of the UBCM pair, as shown in Fig. 3.25.

In order to obtain the full-bandwidth amplification, the compressor is divided into two portions before and after the BBO. The experimental setup for the sub-5-fs NOPA
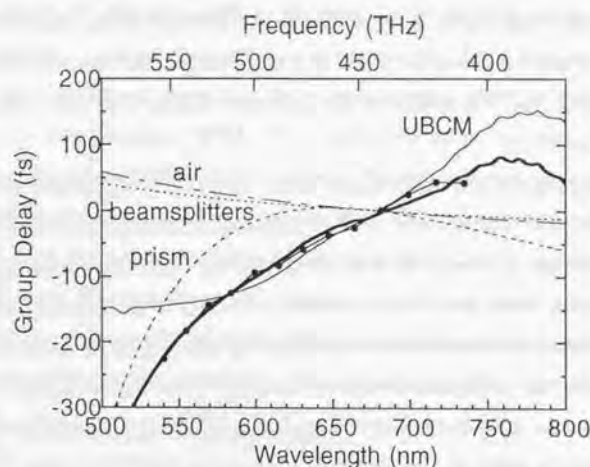
Fig. 3.25. GD property of the compressor. The GDs of the total compressor (bold solid curve), the UBCM pair with four round-trips (thin solid curve), the prism pair (dashed curve), air with a 4.5-m path length (dashed-dotted curve), and the beam splitter in the FRAC (dotted curve) are shown. Also shown is the measured GD of the signal (full circles) with the sign reversed.
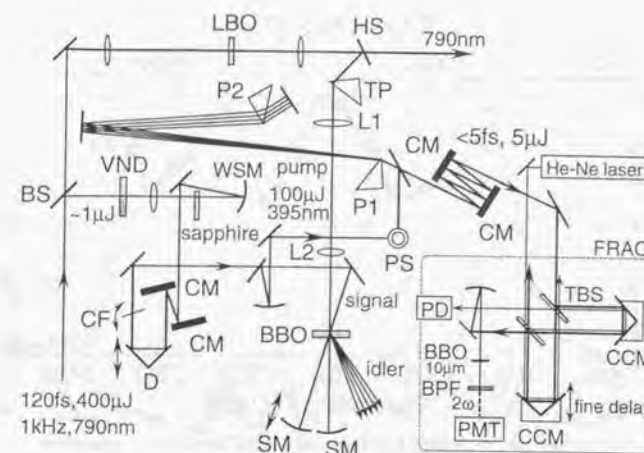
Fig. 3.26. Schematic of the visible sub-5-fs pulse generator. BS, beam sampler; HS, harmonic separator; TP, prism for pulse-front tilting; L1, L2, lenses for the telescope; SM's, spherical mirrors (r = 100 mm); VND, variable neutral-density filter; WSM, spherical mirror (r = 120 mm); CF, cut-off filter; D, optical delay line; PS, periscope; P1, P2, 45° fused-silica prisms; TBS, thin beam splitter; CCM's, corner-cube mirrors; BPF, bandpass filter; PMT, photomultiplier; PD, photodiode.

is shown in Fig. 3.26. The pre-compressor is composed of one UBCM pair in a single round-trip configuration, and the main compressor is of another pair in three round-trip configuration and other elements. The insertion of the UBCM pair before the crystal reduces the seed chirp to a ~10-fs GD difference between 530 and 770 nm, and Eq.(3.23) is sufficiently fulfilled and the full-bandwidth operation over the two amplification stages is enabled. As is reflected in the chirp properties of the signal and idler inspected so far, the effects such as a SPM or a cascaded second-order process [116] seem to be weak enough under the experimental condition. Therefore the reduction of the initial chirp does not change significantly the net pulse parameters including the overall chirp property.

The pulse energy is from ~6 to 7 μJ just after the BBO, and after the main compressor it is about 5 μJ. The highest throughput of ~80% is attained by the UBCMs; only the reflection on the surfaces of the prisms originates the loss. The
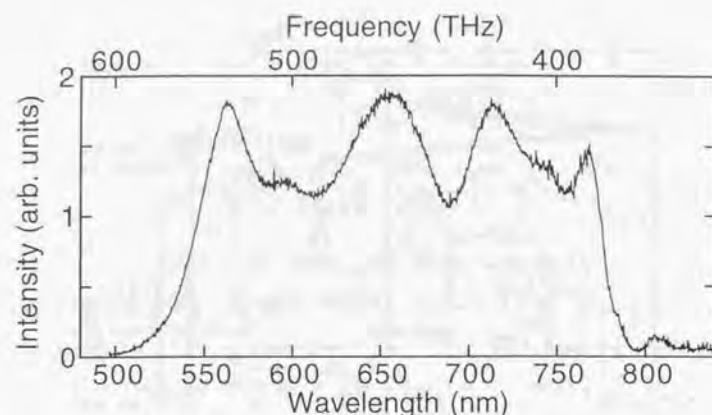
Fig. 3.27. Spectrum of the signal pulses under a full-bandwidth operation.

spectrum of the signal is shown in Fig. 3.27. The spectral shape depends on the positions of the delay lines, which are fixed to maximize the bandwidth. The FWHM is as broad as 240 nm (150 THz), and the TL pulse width is 4.4 fs. The bandwidth is slightly narrower than that reported in ref. [65]. The cut-off filter of the seed effectively suppresses the amplification around 790 nm, where the chirp exhibits a large nonlinearity (see Fig. 2.8). The collimated seed-pump beam interaction also avoids the spectral broadening of the signal caused by the beam divergence [101], which is accompanied by an undesirable spatial chirp. Careful attention to both of these details is essential to obtain a signal compressible to the TL.

The pulse shape is measured by a FRAC as is in Section 3.2.3. The pulse energy is appropriately reduced by an iris before the measurement. Figure 3.28 shows the FRAC trace of the signal after the slight optimization. The sech²-fit pulse width is as short as 3.5 fs, which is shorter than the TL width. Because of the significant modulation of the spectral intensity, such assumption cannot give an accurate width [21]. In the present work the pulse width is estimated by Fourier-transforming the spectrum including the wavelength dependence of the phase in two ways.

First, the phase is calculated from the properties of the measured GD of the signal $T_{pulse}(\omega)$ and the GD of the compressor $T_{compressor}(\omega)$ (see Fig. 3.25). The phase $\phi(\omega)$ is
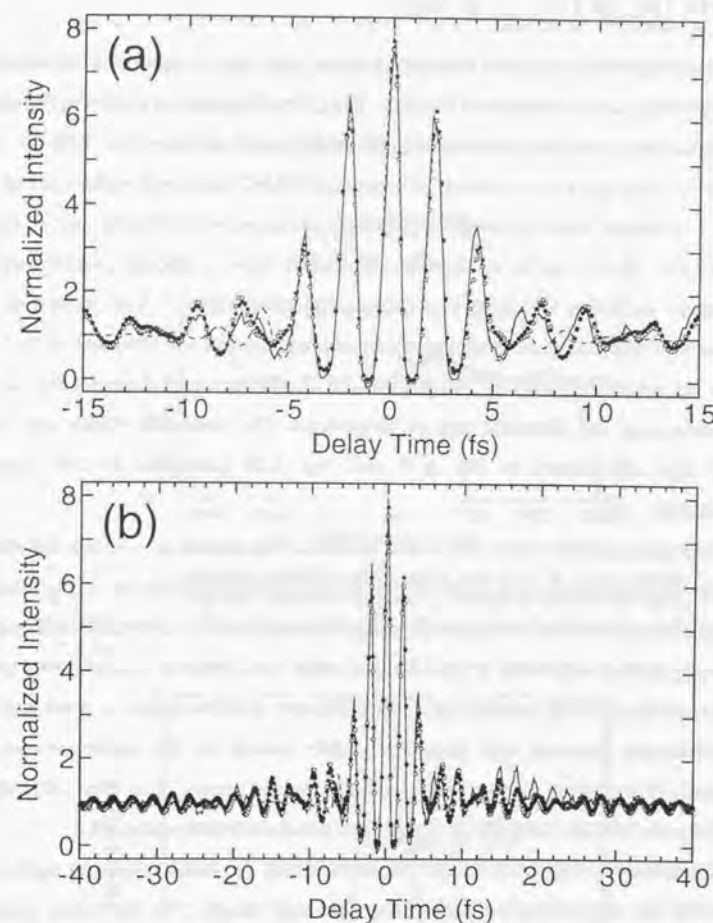
Fig. 3.28. FRAC trace of the compressor output (a) for $|\tau| < 15$ fs and (b) for $|\tau| < 40$ fs (τ: delay time). Measured (solid curve), calculated (open circles, see text), FT-fit (full circles, see text), and sech²-fit (dashed curve) traces are shown. The sech²-fit pulse width is 3.5 fs, whereas the calculated and FT-fit pulse widths are 4.7 fs and 4.7±0.1 fs, respectively.

calculated as

$$\phi(\omega) = \int^{\omega} \left(T_{pulse}(\omega') + T_{compressor}(\omega') \right) d\omega'. \qquad (3.24)$$

The scattering of the measured GD caused by the poor time resolution is smoothed by being fitted to a cubic-polynomial function. The calculated phase is shown in Fig. 3.29. The FRAC trace is then constructed and indicated by open circles in Fig. 3.28.

The second approach is fitting the measured FRAC trace with parameters of the phase. The complicated wavelength dependence of the GD of the UBCMs are included. The residual phase can be reasonably assumed to have a smooth property and is determined by fitting the trace to a cubic-polynomial function with respect to the frequency [23,24]. Because of the use of the autocorrelation, the direction of the time axis is not determined only by this process. By comparison with the calculated phase aforementioned, the direction can be determined. The estimated phase and fitted FRAC trace are shown in Fig. 3.29 and Fig. 3.28 (indicated by full circles), respectively.

Both phase profiles show the similar behavior. The deviation is within $\pi/2$ radian over the whole spectral range from 510 to 790 nm. The oscillations are due to those of the GD of the UBCMs. The large deviations in the regions for < 500 and > 800 nm are due to the limited bandwidth of the UBCMs, which are, however, less effective to the pulse-width broadening because the spectral intensity in these regions is weak enough. The difference between both phases is mainly caused by the uncertainty of the measured GD without information at whole spectral range. It is also difficult to determine the precise values of the compressor parameters such as the IPL.

The calculated and fitted FRAC traces are nearly the same shape and agree very well with the experimental trace even in the side wings. The estimated intensity profiles are shown in Fig. 3.30. The calculated profile gives a 4.7-fs duration, whereas the fitted one gives a 4.7±0.1-fs duration. The result indicates that the phase correction with the highest precision is attained using the prism-chirped mirror compressor and almost TL pulses are obtained. It is the first demonstration that the UBCMs is applied to the visible range over more than 200 THz. Note that the electric field oscillates only

with 2.2 cycles in the FWHM of the intensity profile.

The difference of the intensity profiles clearly indicates the limitation in extracting the pulse shape from a FRAC trace. The information of the phase is mainly included in the fringes of the side wings which, however, cannot be measured with enough high signal-to-noise ratio in many cases, and the uncertainty is then caused especially in the shape of the trailing pulses. However, the pulse width which is
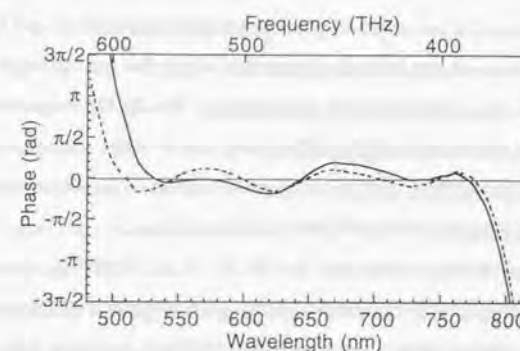
Fig. 3.29. Spectral phase profiles of the pulse extracted by a calculation using the GD property (solid curve) and FT-fitting of the FRAC trace (dashed curve). The linear dependence of the phase on frequency is arbitrarily subtracted.
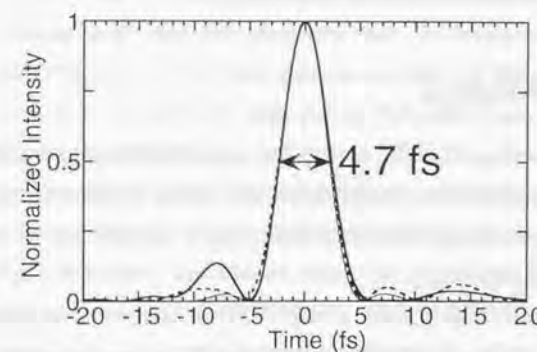
Fig. 3.30. Intensity profile of the compressed pulse. The TL pulse width determined by the spectrum is 4.4 fs (thin solid curve), whereas the calculated (thick solid curve) and FT-fit (dashed curve) pulse widths are 4.7 fs and 4.7±0.1 fs, respectively.

defined as the FWHM is reasonably estimated by these method with a 0.1-fs accuracy. The pulse shape and phase can be precisely determined by other methods such as FROG [96]. It is still quite difficult to apply these methods to the measurement of the sub-5-fs signal pulse, which has the broadest spectrum across the visible region. However, it is an important subject to be challenged in the nearer future.

As far as we know this is the shortest visible pulses ever reported, and the first success of a sub-5-fs pulse manipulation using other method than the continuum-compression scheme. Those sub-5-fs pulse generations reported in 1997 are all based on a Ti:sapphire laser or amplifier, the spectra of which are mainly located in the NIR and limit the versatile spectroscopic applications. The NOPA expands the spectral range of sub-5-fs pulses to the higher frequency and enables the investigation of the ultrafast kinetics in materials such as conjugated polymers, visual pigments, and wide band-gap semiconductors with the highest time resolution.

One of the outstanding advantages of a NOPA is the flexibility of the pulse width in the range longer than 5 fs by selecting some spectral portion by increasing the seed chirp. For example, inserting a 1-mm-thick fused-silica substrate before the crystal narrows the bandwidth and tunable TL pulses with a 6 to 8-fs duration are generated from 550 to 700 nm by simply scanning the delay line of the seed and adjusting the prism insertion amount, as performed in Section 3.2.

3.5. Future Prospects

We have investigated NOPA as a tunable shortest pulse source and then achieved the outstanding ability. These achievements will lead us to a new regime in ultrafast science. The further progression of the NOPA can be foreseen and we would like to note the planning here.

The full-bandwidth operation of the NOPA also enables the further spectral broadening of the idler. The bandwidth should be the same as that of the signal and a sub-5-fs pulse generation is also expected in the NIR region. However, the phase inversion between the signal and idler makes it more difficult to design the pulse

compressor. The bandwidth of the prism compressor to attain the positive GDD is not broad enough to cover the broader idler spectrum with a negative chirp as shown in Fig. 3.18. For the more precise phase correction, we plan to manufacture the chirped mirrors for the NIR region. The recent calculations of the GD in the dielectric multilayer system indicates the possibility to attain the appropriate positive chirp over the expected broadest spectral region from 800 to 1400 nm, where the GDDs of most of optical elements fall into negative [117]. Also examined is the use of a spatial-light modulator (SLM) [118,119,120,121]: it seems straightforward because the idler is intrinsically dispersed spatially. The angular-dispersion compensator designed in this work can act as a pulse shaper by arranging a SLM composed of more than 100 elements in the Fourier plane. The SLM manipulates the phases of individual spectral components programmably and enables the precise pulse compression. The adaptive approach progressed recently [122,123,124,125] seems to give the practical handling ability in the experiments.

The further improvements of the angular-dispersion compensator is also essential for the shorter pulse generation. The variation of the exit angle of the idler is mainly due to the nonlinear angular dispersion of the grating as mentioned in Section 3.3.1, which may be further optimized by a fine optical design using non-spherical mirrors. The adaptive approach using a deformable mirror [126,127] can be also applied. Much distorted GD caused by the aberration using such optics can be acceptable because of the high programmability of a SLM. The generation of sub-5-fs NIR pulses by using these high technologies is a great challenge, and the first achievement of a monocycle optical pulse is strongly expected.

The further broadening of the bandwidth is also one of the most interesting subjects to be quested. Two schemes can be proposed: (1) A multi-stage amplification with each stage with different noncollinear angles can amplify the different spectral portions of the injected seed pulses [45,128]. The extension of the signal spectrum to less than 500 nm is expected. (2) As discussed in Section 2.2, a NOPA can have the broadest bandwidth if both of the signal and idler have angular dispersions to satisfy Eq.(2.12). This is the general case of the group-velocity matching between the signal

and idler. The bandwidth can cover the wide range over the visible and NIR (see Fig. 2.3). The key point to utilize this marked property is to design an angular-dispersion generator/compensator system, which can precisely control the angular dispersion of the signal and/or idler to satisfy the above strict requirement.

It is expected that the pulse energy can be scaled up to a mJ level by the combination with a technology of a chirped-pulse OPA pumped by a Q-switched laser [89,129]. This approach is a candidate for a visible terawatt source [130]. The pulse-front-matched interaction will become more important in such a case of a high-energy operation, which requires a larger beam diameter in a gain medium.

By utilizing these methods we can expect the generation of much shorter high-power optical pulses from a NOPA over the wider spectral range. It seems one of the most promising candidates to lead us to the regime of a monocycle optical pulse (~2 fs). Further extensive investigations by world-wide researchers will succeed and the further progress is expected to be experienced in the nearer future.

4. Application: Real-time Spectroscopy of Coherent Geometrical Relaxation in Polydiacetylenes

4.1. Introduction

4.1.1. Polydiacetylene – One-dimensional Conjugated Polymer

Conjugated polymers are one of the most promising candidates for future applications to nonlinear optical devices because of their often large and ultrafast nonlinear optical susceptibilities, varieties of main chains and side groups, and facility of processing of large-area samples [131]. Optical and electronic properties of conjugated polymers have attracted enormous attention in order to understand the characteristic nonlinearity. Among them, polydiacetylens (PDAs) which possess the backbone structure of a diacetylene-type configuration $(=CR-C\equiv C-CR'=)_n$ (R and R' are substituents, see Fig. 4.1(a)) are the most intensively studied because of their several remarkable characteristics. The values of the third-order optical susceptibilities $\chi^{(3)}$ exceed 10^{-9} esu and the relaxation is completed within a few picoseconds. These features put the group of materials on a particular position in material science. The wide variety of sample morphologies such as solutions, single crystals, and thin films are available and also enable many scientists to investigate this material by versatile spectroscopic methods [132].

The PDAs have been modeled as a quasi-one dimensional semiconductor. The π-electron conjugation extended over many diacetylene units along the main chain originates the characteristic property of the one-dimensional electronic system. The formation of a Wannier-type exciton associated with the $\pi-\pi^*$ transition is well-characterized and called as a free exciton (FE) [133]. The oscillator strength of the exciton transition is substantially concentrated on one exciton state ($k = 0$), which originates the well-defined sharp absorption peak in the visible far below the edge of
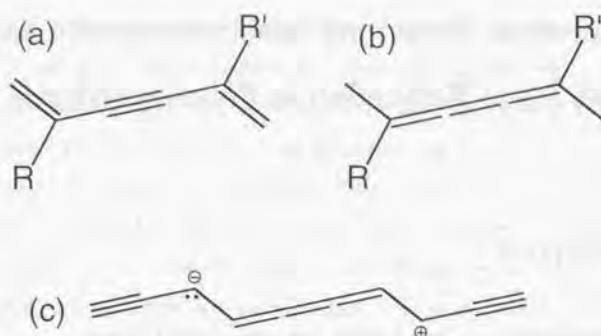
Fig. 4.1. Molecular structures of a PDA backbone. (a) Acetylenic PDA, (b) butatrienic PDA. (c) Schematic structure of a STE localized in the butatrienic configuration.

the conduction band as well as the gigantic optical nonlinearity.

Another characteristic feature is the strong electron-phonon coupling. The backbone consists of alternating single, double, and triple bonds of carbon atoms. All of the stretching vibrations are substantially coupled to the electronic transition and induce many different nonlinearities from those in most of inorganic semiconductors. The electronic excitation is coupled with these vibrations, which induces not only a strong resonant Raman activity [134] but various optical nonlinear processes such as Raman gain [135], inverse Raman scattering [135], phonon-mediated hole burning [136,137] and optical Stark shift [138,139], and so on. The change of the π bond-orders accompanies the electronic transition by the coupling, and the resultant lattice deformation localized in the main chain triggers the ultrafast nonlinear response of conjugated polymers. In polyacetylenes (PAs) the creation of the localized excitation called soliton have been well examined by both theoretical [140] and experimental studies [141,142,143,144]. The degeneracy of the ground state characterizes PAs and facilitates the description of the kinetics after photo-excitation.

4.1.2. Geometrical Relaxation to form Self-trapped Exciton

Extensive experimental works have been also performed to investigate the fast

relaxation dynamics of PDAs with no degeneracy in the ground state [131]. Kobayashi and his co-workers have investigated several PDAs systematically [135,145,146,147, 148,149,150,151,152,153,154] and proposed that the initial kinetics after photo-excitation is generally dominated by a relaxation of a FE to a self-trapped exciton (STE) [133], which is localized as a result of the lattice deformation. Because there is no barrier for the self-trapping of excitons in one-dimensional systems [155], the structural change following the photo-excitation is expected to take place within few periods of the coupled vibrations [155,156].

In pump-probe experiments of various PDAs the formation of a STE has been generally observed as a photo-induced absorption (PIA) below the stationary absorption edge (see Fig. 4.2). The broad PIA spectrum is assigned to the transition from the STE to upper-lying nB_u and/or mA_g states and a biexciton state [133]. The characteristic spectral change of the PIA to a higher energy within the initial 500-fs delay is explained in terms of a relaxation from the FE to the bottom of the potential surface of the STE by the emission of phonons, as schematically shown in Fig. 4.3. The formation of the PIA around the highest edge of the spectrum takes about 150 fs, which was explained by Kobayashi et al. as the formation of a "nonthermal" STE [146,147,149]. The nonthermal STE represents the non-equilibrium state where a STE is not relaxed to the bottom of the potential surface and the binding energy remains as the vibrational energy of the strongly coupled modes. This time constant is often called as the formation time of a STE, however, it is to be mentioned that the self-trapping process may be completed within the vibrational periods of the C=C and C≡C stretching modes (16–23 fs), which has not been time-resolved. These features are also observed in other polymers such as PAs [143,144] and polythiophenes (PTs) [157] with the time constants of 70–150 fs, indicating the formation of the STE plays an important role in the initial dynamics of conjugated polymers.

The formation of the STE is expected to be the geometrical relaxation from an acetylenic structure to a butatrienic structure (Fig. 4.1) [146]. The FE moving over the acetylenic main chain creates by itself a displaced potential via the electron-phonon coupling and then trapped in the resultantly-formed butatriene-like structure localized
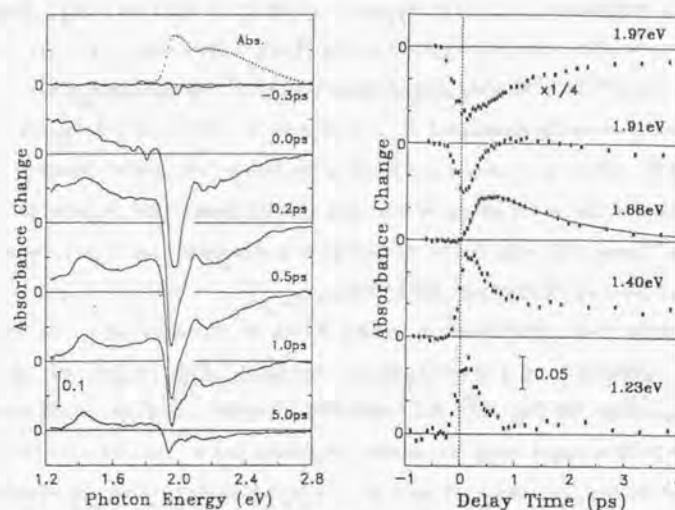
Fig. 4.2. Typical transient behaviors of a blue-phase oriented PDA-4BCMU (4-butoxycarbonylmethylurethane) film at 290 K induced by a 100-fs pump pulse at 1.98 eV. (left figure) Transient absorption spectra. The dotted curve is the stationary absorption spectrum. (right figure) Time dependence of the absorbance change at five different photon energy. The solid curve at 1.88 eV is the calculated trace with the formation and decay times of 140 fs and 1.6 ps, respectively. (quoted from ref. [147])

in the main chain. Thus the transverse axis in Fig. 4.3 represents the local deformation mode which explains this acetylene-butatriene isomerization. Yoshizawa *et al.* investigated this geometrical relaxation by the time-resolved resonance Raman gain spectroscopy of PDA-3BCMU (3-butoxycarbonylmethylurethane) and concluded the formation of the butatrienic structure by observing a transient mode at 1200 cm^{-1} which had a similar behavior to the PIA [152].

The relaxation of the PIA and the recover of the population in the ground state are completed within a few picoseconds [131]. The features of the relaxation time insensitive to temperature and the dependence of the FE energy have led a tunneling model between the STE potential and the ground state [146,147,149]. Around the crossing the quantum-mechanical tunneling occurs dominantly and the radiative

relaxation process is suppressed. In the standard blue-phase PDAs which have the exciton peaks around 1.8–2.0 eV the PIA is relaxed within 1–2 ps, which is systematically explained by this tunneling process [149,154]. However, it can partly explain the characteristic low quantum yield of the order of 10^{-5} in these PDAs under the conventional assumption that the lowest excited state has a B_u symmetry [131].

Recent experimental [158,159,160,161,162] and theoretical [163,164] studies manifest the lowest singlet state in a blue-phase PDA to be an optically-forbidden 2^1A_g state lying ~0.1 eV below a 1^1B_u FE state. The low quantum yield is then reasonably explained by the expected radiative lifetime longer than 100 ns. The expected internal conversion (IC) from the 1^1B_u FE to the 2^1A_g state complicates the dynamics of the above mentioned self-trapping picture [153,154]. There has been no experimental verification about the existence of the exciton in the 2^1A_g state. In addition, we face the question whether the coherence of the stretching motion coupled to the exciton can be maintained or not through the IC process.

Owing to the recent progresses of femtosecond light sources it has become feasible to detect a molecular motion directly by using various time-resolved
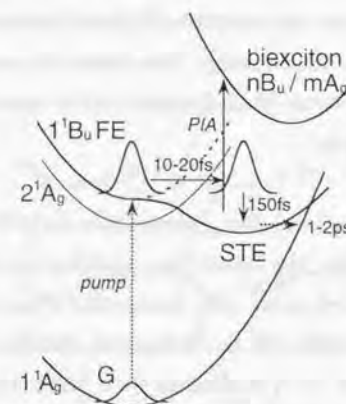

Fig. 4.3. Model of relaxation kinetics in potential surfaces in standard blue-phase PDAs. The transverse axis is the configurational coordinate representing the local deformation from an acetylenic backbone to a butatriene-like backbone.

spectroscopic methods. There have been many reports about the observation of the coherent wavepacket motion in small molecules in a gas phase [165], crystalline lattices [166], solutions [167,168], and visual pigment molecules [169,170]. However, the molecular vibration in PDAs is expected to be in the time scale of 10–20 fs due to the large force constants between the carbon atoms and the observation has been a challenging work. The first report was by Pham, Bigot, and their co-workers in 1995 [171], who observed the oscillations in a photon-echo signal of a PDA-DCHD (1,6-di(n-carbazolyl)-2,4 hexadiyne) film caused by the C=C stretching motion by using 10-fs pulses. They also observed the same stretching mode in the transient bleaching signal [172]. In both cases they reported that the wavepacket motion continued only for the initial 100 fs after excitation and the C≡C stretching vibration could not be observed during this period. From these results they proposed a quite different model from the one above mentioned: just after photo-excitation the transient butatrienic configuration is undertaken and then return to the acetylenic configuration after the excitonic dephasing (~50 fs) [171]. However, the possibility of existence of the higher-frequency mode of the C≡C stretching (period of ~16 fs) cannot be excluded because of their limited time resolution. In addition, no detailed information about the formation of the self-trapped state was derived because they could not investigate the PIA region well below the exciton energy. Thus further investigations are essentially required to elucidate the initial photo-dynamics and to determine the geometrical relaxation mechanism in detail.

In this Chapter the ultrashort pulses generated from the NOPA is applied to clarify these fundamental processes. The highest time resolution as well as the enormously broad spectrum of the sub-5-fs pulses show the remarkable potentiality to observe such a fast process occurring within 100 fs. A surprising multimode wavepacket motion with the shortest period of 16 fs is observed for a longer period than 1 ps, which visualizes the coherent geometrical relaxation to a localized butatriene-like configuration by the self-trapping process for the first time. The transient "real-time" spectrum of the PDAs is expected to offer a valuable information for the theoretical

investigations of the electron-phonon coupling property in a non-degenerate conjugated polymers.

4.2. Sample

4.2.1. Molecular Structure

The PDA studied is a novel ladder-polymer, poly[5,7,17,19-tetracosatetraynylene bis(N-butoxycarbonylmethyl)carbamate] (PDA-4BCMU4A(8)) [173]. The sample was prepared by Dr. H. Matsuzawa and Prof. H. Nakanishi at the Institute for Chemical Reaction Science of Tohoku University. The synthetic procedure of the diacetylene monomer 4BCMU4A(8) is described in refs. [173,174]. The thin film was prepared from $CHCl_3$ solution on a 1-mm-thick quartz plate by a spin-coating method. The film was polymerized in the solid-state by γ-ray irradiation with 2.5-Mrad dosage. The thickness of the film is 370 nm. The number of repeat units in the polymer is unknown.

The chemical structure of PDA-4BCMU4A(8) is shown in Fig. 4.4. From the high-resolution solid-state ^{13}C NMR spectroscopy it was confirmed that the
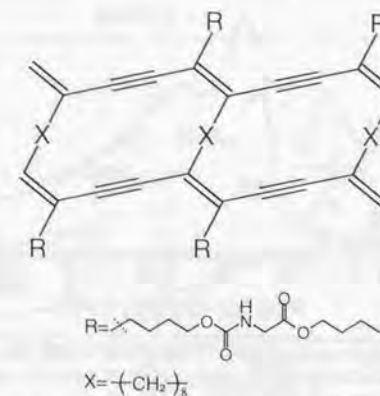

Fig. 4.4. Chemical structure of PDA-4BCMU4A(8).

polymerization takes place at the both butadiene moieties and the ladder structure composed of two PDAs linked with ethylene chains is constructed [173]. The powder X-ray diffractometry also indicates that the monomer crystal transforms to polymer crystal without large deterioration of their crystalline lattices [173]. The advantage of the ladder structure is the enhancement of the third-order optical nonlinearity by increasing the density of the π-conjugated PDA chain per unit volume [175].

4.2.2. Absorption Spectrum

Figure 4.5 shows the absorption spectrum of the PDA-4BCMU4A(8) film at room temperature. An absorption peak appears at $E_x = 1.956$ eV, which is the characteristic excitonic peak of the lowest singlet free excitons (1^1B_u FEs). The phonon sideband structure appears at the higher photon energy, which is clarified by the second-order derivative of the spectrum ($-\frac{\partial^2 I}{\partial E^2}$) and assigned to the sidebands of C=C and C≡C at 2.12 eV and ~2.21 eV, respectively. The sub-5-fs pulses of the NOPA output can
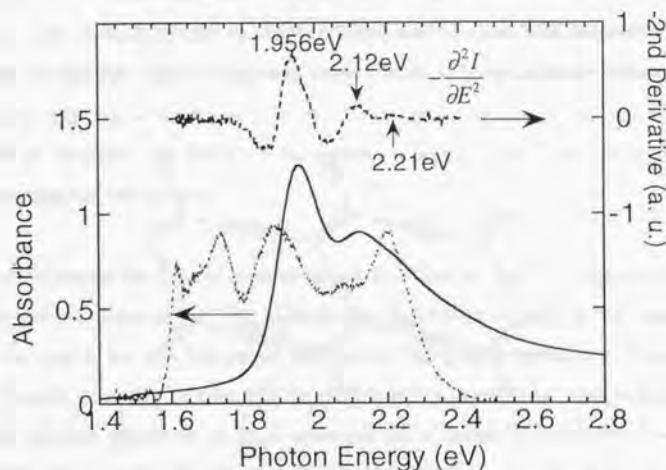
Fig. 4.5. Absorption spectrum of a PDA-4BCMU4A(8) film (solid curve) and its second-order derivative with respect to photon energy (dashed curve). Also shown is the spectrum of the sub-5-fs pulses used for the pump and probe (dotted curve).

excite the manifold of these vibronic states simultaneously. The spectrum is red-shifted by ~0.015 eV with respect to that of a non-ladder polydiacetylene PDA-4BCMU. The PDA-4BCMU4A(8) is classified as a typical blue-phase acetylenic PDA [131].

4.2.3. Raman Spectrum

Resonant Raman spectra of PDAs excited around the excitonic band mainly reflect the vibrations along the polymer chain and show simple structures despite the presence of complex side groups [176,177,178]. This is because only vibrational modes which couple with the π electrons delocalized over the backbone are enhanced due to the resonance condition. Figure 4.6 shows the static resonant Raman spectrum of a PDA-4BCMU4A(8) film at room temperature. Experimental details are as follows. The pump source is the second harmonics of a CW mode-locked Nd:YLF laser (60 mW, 100 ps at 527 nm (2.355 eV)). The Raman spectrum is measured with 90° scattering geometry on a triplet spectrometer (60-cm focal length). The resolution is 0.1 cm^{-1}. During the measurement the sample is rotated to avoid any heating effect. The strong Rayleigh wing prevents the measurement of the Raman modes with frequencies lower than 400 cm^{-1}.

There exist several remarkable peaks on top of the background due to the

Fig. 4.6. Resonant Raman spectrum of a PDA-4BCMU4A(8) film.

fluorescence. Two strong peaks at 1455 and 2080 cm^{-1} are modes which are generally observed in PDAs and correspond to the normal stretching modes of C=C and C≡C along the backbone, respectively [176,17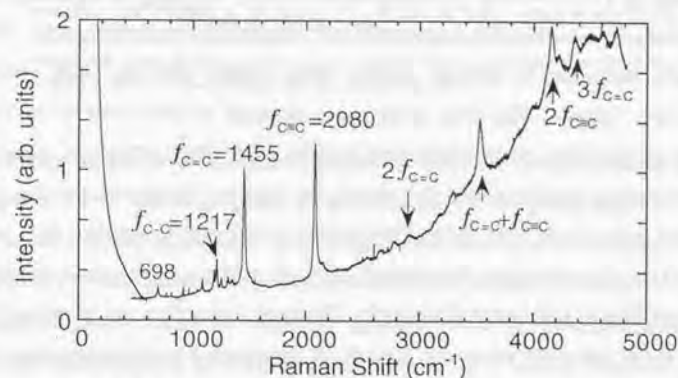7,178]. These overtones and combination modes are also observed. The relatively weak peak at 1217 cm^{-1} corresponds to the C–C stretching mode, which is sometimes attributed to a C=C bending mode [179], because this stretching mode is coupled inevitably with a bending mode including the double bond [134,177]. As reported in other PDAs, several weak peaks between 1000 and 1400 cm^{-1} are also observed. Lewis *et al.* calculated the normal modes in several PDAs and these modes are considered to be the modes involving complex motions of the C–C and C=C bonds and pendant side groups [177]. It is also possible to explain these modes by a Fermi resonance interaction with side groups [180]. The modes below 800 cm^{-1} are considered to be backbone deformation modes [181]. The peak at 698 cm^{-1} has not been clearly assigned in previous literatures. Only Bigot *et al.* reported it is a torsional mode [172].

4.3. Sub-5-fs Differential Transmission Spectroscopy System

The experimental setup of the sub-5-fs time-resolved pump-probe system is shown in Fig. 4.7. The signal pulses from the NOPA are divided to the pump and probe arms by a 0.5-mm-thick broadband beam splitter. The pump beam is intersected intermittently by a mechanical chopper (EG&G, Model 198) at a frequency $f = 158$ Hz. The probe beam passes through another beam splitter and the pulse energy is appropriately reduced. The beam splitters are identical to those used in the fringe-resolved autocorrelator of the NOPA (see Section 3.2.3). Both reflections occur at the same air-coating interfaces, which balances the material dispersion amounts in the pump and probe arms. The pulse compression at the sample position thus can be optimized by decreasing the intraprism path length in the compressor to compensate only the additional path length through air. After each beam diameter is reduced by an iris, the pump and probe beams are focused on the sample by spherical mirrors with r = 200- and r=300-mm curvatures, respectively, with the folding angles of less than 3°

Fig. 4.7. Apparatus of the sub-5-fs differential transmission spectrometer. TBS, thin beam splitter; SM1,SM2, r = 200- and 300-mm spherical mirrors; Ir, Iris; PD, photodiode.
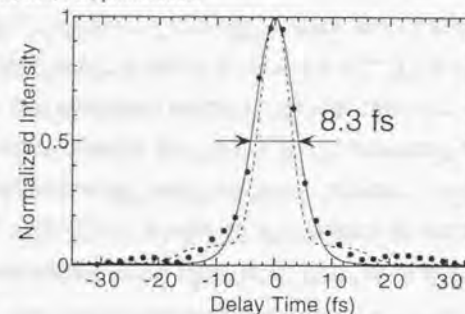
Fig. 4.8. Intensity autocorrelation trace of the sub-5-fs pulses at the sample position. The FWHM of the trace is 8.3 fs and the pulse width estimated by $sech^2$-fit is 5.4 fs (solid curve). The broadening is due to the geometrical smearing. Also shown by the dashed curve is the calculated trace from the estimated 4.7-fs intensity profile shown in Fig. 3.30.

to minimize astigmatism. The time separation between the pump and probe pulses is changed by a fine stage (Sigma-koki, P-AES-60X(IS)-20) composed both of a mechanical stepping motor and a piezo-electric transducer. The precision of the stage position is ±10 nm. The probe pulse spectrum after the sample was dispersed by a 30-cm monochromater (Ritsu, MC-30N) and measured with a Si photodiode with a 5-nm resolution. The signal is pre-amplified and detected by a lock-in amplifier (EG&G, Model 5210) locked to f. After measuring the transmittance change $\Delta T(\omega)$, the

stationary transmittance ($T(\omega)$) is measured by chopping the probe itself without pump and the differential transmittance ($\Delta T/T$) is evaluated. The broad spectrum of the probe pulse enables the investigation over the wide spectral range from 1.6 to 2.3 eV. All measurements presented here are performed at 295 K.

Figure 4.8 shows a typical intensity autocorrelation trace of the sub-5-fs pulse at the sample position after the prism position is optimized. The sech^2-fit pulse width is 5.4 fs. The shape is clearly broadened from the 4.7-fs autocorrelation trace calculated from the estimated intensity profile in Section 3.4.4. The wings on both sides are due to the structure of the pulse. The broadening can be explained by the geometrical smearing (see Appendix C). In the present experiments the beam crossing angle (θ_{ext}) is 1.5° and the beam diameters of the pump (d_{ex}) and probe (d_{pr}) are 100 μm and 80 μm, respectively, which give the smearing factor $\delta\tau = 2.6$ fs. For a 5-fs Gaussian pulse the measured pulse width τ_p^{meas} will then be broadened to 5.6 fs, which corresponds to a 12-% increase and it is substantial for the present experiment with such a high time resolution. All of the parameters θ_{ext}, d_{ex}, and d_{pr} must be further optimized to avoid the reduction of the time resolution. From the above estimation the resultant time resolution of the system is concluded to be about 8 fs (FWHM). The pump pulse energy and photon density are about 50 nJ and 2.1×10^{15} photons/cm^2, respectively, and the probe pulse energy is about 5 nJ. Polarizations of the pump and probe pulses
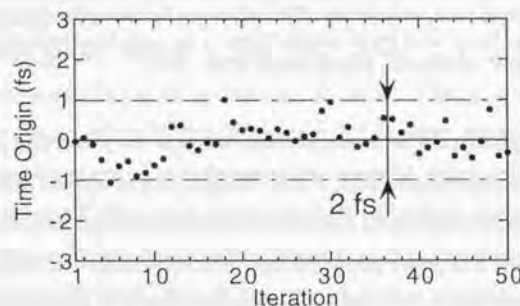
Fig. 4.9. Drift of the peak positions of autocorrelation traces. Each peak position is determined by fitting. The overall fluctuation width is less than 2 fs.

are parallel to each other.

Figure 4.9 shows the change of the peak positions of the autocorrelation traces measured over two hours, exhibiting the accuracy of the delay time and time origin of different decay traces. The stage is highly stabilized by a closed-loop feedback system and the resettability is assured to be less than 100 nm. Therefore it is considered that the ~2-fs scattering originates from the mechanical instability of the optical mounts and/or refractive index fluctuation due to air flow in both arms. The amount of this shift is almost inevitable in such a system using a non-common path.

The measured decay curves are fitted using the biexponential response function

$$\frac{\Delta T(t)}{T} = I_{AC}(t) \otimes \left[I_0 \delta(t) + A_1 \exp\left(-\frac{t}{\tau_1}\right) + A_2 \exp\left(-\frac{t}{\tau_2}\right) + C \right], \tag{4.1}$$

where the first and last terms in the parenthesis mean an instantaneous response and a long-living component, respectively. $I_{AC}(t)$ is the autocorrelation trace measured by the above mentioned method. Because chirp-free pulses are used for both pump and probe, the same autocorrelation trace can be used for the convolution with the response function at whole probe photon energy. The instantaneous component expresses the coherent artifact [182], and then its strength should be dependent on the probe photon energy and may be affected by cross-phase modulation [183]. Thus it is quite difficult to estimate the amount of the contribution at the zero-delay. In the present experiment this component is reasonably introduced to best-fit the trace to separate the molecular motion. Also will be discussed this problem below.

4.4. Dynamics of PDA-4BCMU4A(8) on a 5-fs Time Scale

4.4.1. Real-time Spectra

The time dependence of the transmittance change in a PDA-4BCMU4A(8) film is shown in Fig. 4.10. The measurements were performed at 15 different probe photon energies over the wide spectrum of the NOPA with each time step of 2 fs. The

predominant feature commonly appearing in the traces is high-frequency oscillations in addition to the underlying slowly-varying transient components. The oscillations are observed over the whole probe spectral range and exhibit a quite complicated behavior. Figure 4.11 shows the transient behaviors with extended times to 2.5 ps at six probe energies. The oscillations persist for a period longer than 1 ps. These behaviors are quite different from those Bigot *et al.* reported [172]. They observed oscillations only within the initial 100 fs and rather weak features at the lower energy side. This may be because non-transform-limited (TL) pulses with the longer (9 fs) duration were used in their study. The oscillations are due to the coherent molecular motions which are created both on the ground-state and excited-state potential surfaces as will be discussed later. The complicated structures clearly indicate the motion is composed of several frequency components.

The overall slowly-varying transmittance changes originate from the dynamics of the excited electronic states by the photo-excitation. The positive signal observed for $E_{probe} > 1.9$ eV is due to a bleaching induced by the saturation of the excitonic absorption and the phonon sidebands. Around 1.85 eV the signal is suppressed quickly and crosses zero transmittance change around ~400 fs. At lower probe energies than 1.8 eV the signal becomes negative due to the photo-induced absorption (PIA). The positive behaviors for the initial ~100 fs can be assigned to the stimulated emission (SE). Additional features at a negative delay and around the time origin, especially in the lower energy side, are due to the pump-perturbed polarization decay [182,184], coherent coupling [182], and cross-phase modulation [183]. The non-negligible size of the tail structure of the pulse (see Fig. 3.30) also enhances the artificial signals.
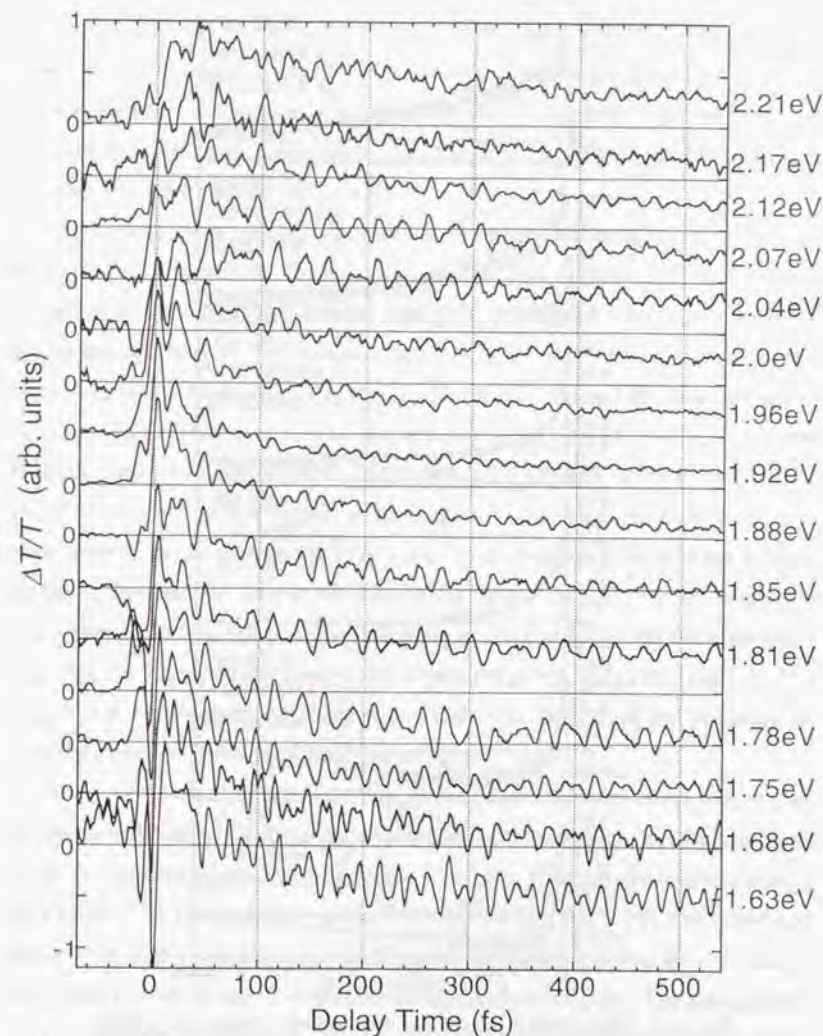

Fig. 4.10. Time dependence of the transmittance change in a PDA-4BCMU4A(8) film at 15 probe photon energies marked on the right. The intensities are normalized at the peak of each trace.
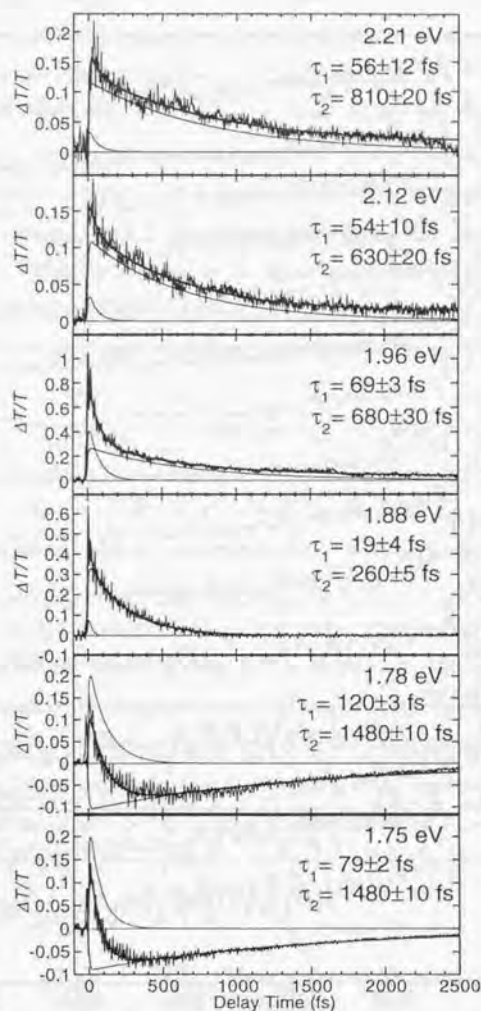
Fig. 4.11. Time dependence of the transmittance change in a PDA-4BCMU4A(8) film with an extended time. The bold curves are the fitting results by biexponential functions. The thin solid curves are the fitting components and the resultant parameters are shown on the right in each frame.

4.4.2. Electronic Dynamics

The time dependence of the transmittance changes seems quite complicated at a glance by the combing effect of the electronic and molecular contributions. However, smearing the oscillating components is possible by scanning the delay line quickly. In order to separate the dynamics of the electrons and molecular motions, the long-term behavior of the electronic contribution is studied. It should be noted that this fast scan also may smear the near-zero fast component.

Figure 4.12 shows the time dependence of the transmittance changes over 5 ps with each time step of 20 fs. The behavior is similar to those of other PDAs previously studied using ~100-fs excitation pulses [146,147]. The bleaching for $E_{probe} > 1.9$ eV is due to the saturation of the absorption to the 1^1B_u FE state. There is a long-living component which exists even at a 5-ps delay, which is assigned to the lowest triplet excitons with the lifetime of several tens microseconds [151,185]. The recovery time becomes faster at the higher probe photon energy. The PIA observed for $E_{probe} < 1.8$ eV after the initial positive signal can be assigned to the transitions from the STE to some upper-lying state. Since the STE relaxes to the bottom of the potential surface, the decay time becomes shorter for lower probe photon energy [147]. No long-living component due to the triplet excitons is observed, which is reasonable because we are observing the higher photon energy side of the broad PIA [147,185]. For 1.8 eV < E_{probe} < 1.9 eV the time dependence is complicated because of the simultaneous contributions of the bleaching and PIA to the signal.

The positive signals observed for $E_{probe} < 1.8$ eV are of great interest. Because the stationary absorption is sufficiently weak in this spectral region, it is reasonable to assign this positive signals as the SE from a 1^1B_u state. This fast component is seen in the transients for probe energy smaller than ~2.0 eV (see Fig. 4.10). The broadband feature of the fast component can be explained as the transitions from the 1^1B_u state to the ground state (0–0) and its broad phonon sidebands (0–1) [150]. The fitting results of the transmittance changes at 1.96 and 1.78 eV by using Eq.(4.1) are shown in Fig. 4.13. The recovery times of the ground state at the FE peak of 1.96 eV are determined
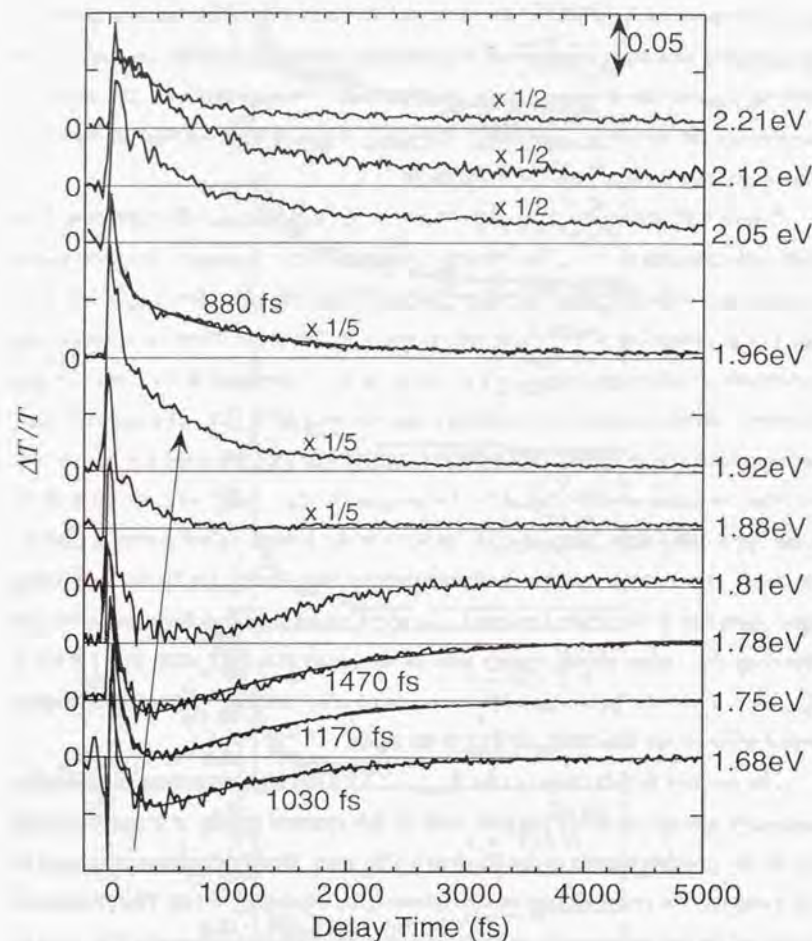
Fig. 4.12. Time dependence of the transmittance change from −200 fs to 5 ps. The time step is 20 fs to suppress the fast molecular motions. The gray solid curves are the fitting traces.
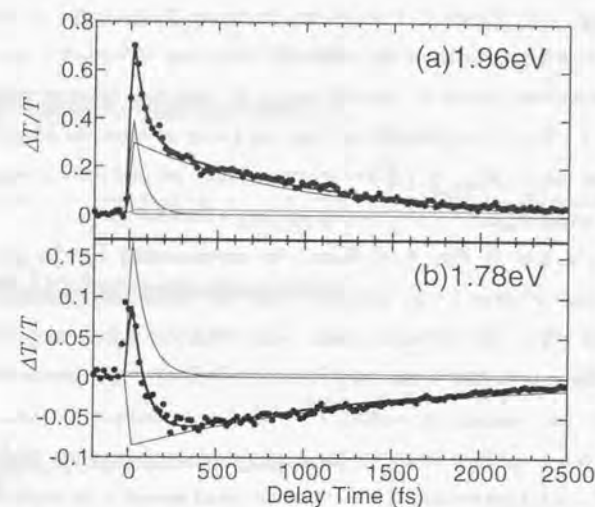
Fig. 4.13. Time dependence of transmission change at (a) 1.96 eV and (b) 1.78 eV. The bold curves are the fitted curves by biexponential; functions. The thin curves are the fitting components.

as 62 ± 5 fs and 880 ± 30 fs. Two decay constants at 1.78 eV are determined to be 85 ± 5 fs and 1.5 ± 0.1 ps. The constants corresponding to the SE are different by ~20 fs from that at 1.96 eV, and this difference is always seen between the transients for E_{probe} > 1.9 eV and E_{probe} < 1.8 eV.

4.4.3. Analysis of Molecular Vibration

For the discussion on the molecular motion, the oscillating components are to be separated from the overall transient curves. We fit the transient curves by Eq.(4.1) and then the electronic contributions are subtracted. The time constants determined in the former section are used as initial values. Even with the uncertainty in the fitting procedure caused by the oscillations, other methods such as a low-pass Fourier-filtering [186] and low-order polynomial fitting [169] seem to be less appropriate due to the smearing of the fast electronic components or the lack of the physical meaning. The fitting results of the time constants are given in the corresponding frames to the

traces in Fig. 4.11. Figure 4.14 shows the oscillating components extracted by this procedure. In order to eliminate the substantial deviations between the measured traces and fitting functions caused by the fluctuations, the high-pass filtering with the cut-off frequency of 150 cm^{-1} is processed and the oscillating components are reconstructed. The oscillations for $E_{probe} > 1.9$ eV decay within 1 ps and only a noise remains, whereas those for $E_{probe} < 1.9$ eV continue for longer than 1.5 ps.

The right side in Fig. 4.14 shows the corresponding Fourier-power spectra integrated from 20 fs to 1.5 ps, with the lower limit constrained by the exclusion of any coherent effects around the zero-delay. The resolution is determined by the range of the transformation and in this case 11 cm^{-1} (HWHM). As shown in Fig. 4.9, the motions of the mechanical mounts of optical components or refractive index fluctuation due to air flow determine the precision of the delay time. The accuracy of the frequency is then estimated as ~ 0.1 % and is small enough to be neglected.

The Fourier spectra clearly show the existence of two main modes of the C=C (~1455 cm^{-1}) and C≡C (~2080 cm^{-1}) stretching over the whole range of probe photon energy. Also observed are the peaks around 230, 700, and 1220 cm^{-1} with intensities dependent on the probe photon energy. All these modes except for the 230-cm^{-1} mode are observed in the static resonant Raman spectrum (Fig. 4.6). A reasonable candidate of the peak at 230 cm^{-1} is the mode of the C–C=C bending in the plane of the backbone, which is typically observed in polyenes [187]. This mode cannot be observed in the Raman spectrum partly due to the Rayleigh scattering. There were also few reports observing Raman modes in this low frequency side in PDAs [180,188].

Bigot et al. observed only the C=C stretching mode and weak mode around 700 cm^{-1} for the initial 100 fs, which was the ground of their claim of the instantaneous formation of the butatrienic backbone structure by the photo-excitation [171,172]. However, our results clearly present the strong C≡C stretching motion induced just after the photo-excitation (see Fig. 4.10). Also clearly different is that the coherence of the oscillation is maintained over 1 ps in our study. Both features mentioned above has been discovered owing to the high performance of the NOPA with the nearly TL shortest pulse shape, which has the duration well below the oscillation period of the
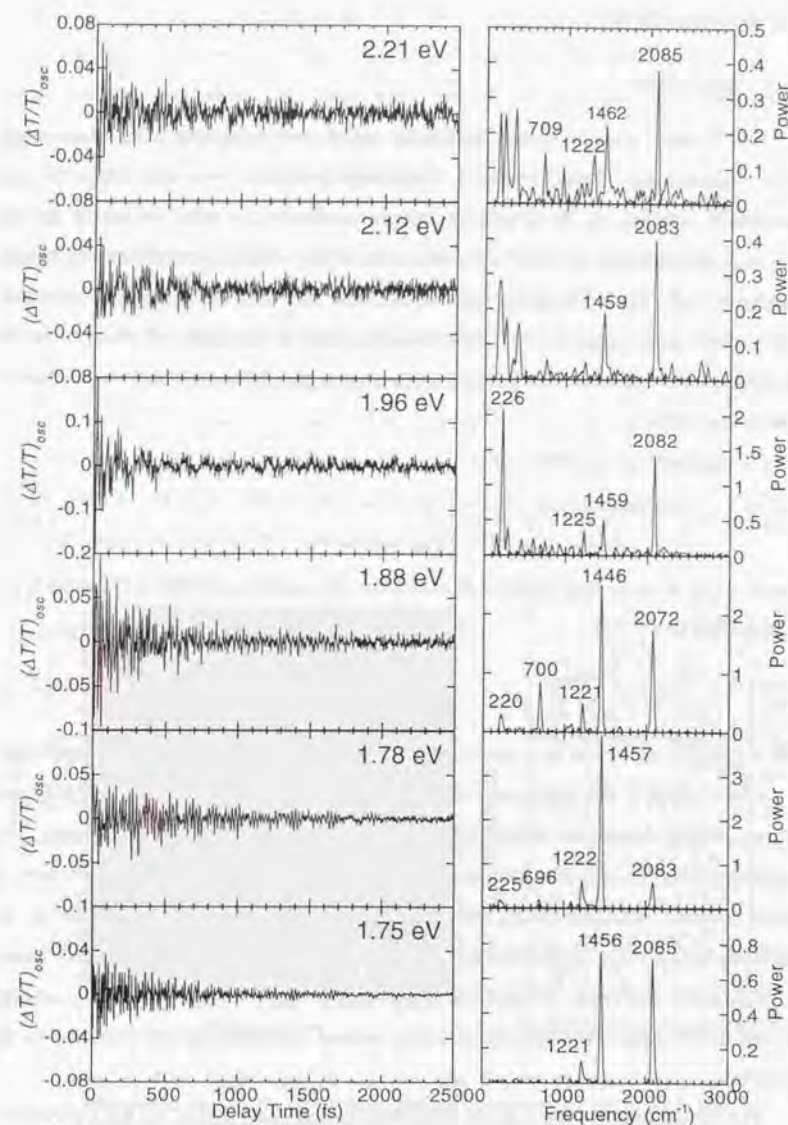

Fig. 4.14. Time dependence of the oscillating components in Fig. 4.11. The corresponding Fourier-power spectra integrated from 20 fs to 1.5 ps are shown on the right.

C≡C stretching (16 fs).

4.4.4. Spectrogram

The Fourier analysis of the oscillating signal over extended delay time range offers information of the averaged vibrational frequency over the range of the wavepacket motion. It is of greater interest to study the time evolution of the frequency components, especially for the study of the ultrafast geometrical relaxation associated with the self-trapping process. One of the most advantageous approach seems to be a spectrogram [189,190], which is used to the study of the revivals of wavepacket motion in anharmonic systems in the gas-phase molecules such as Br_2 [189] and K_2 [190].

The spectrogram is defined as

$$S(\omega,\tau) = \left| \int_{-\infty}^{+\infty} \left(\frac{\Delta T(t)}{T} \right)_{osc} W_H(t-\tau) e^{i\omega t} dt \right|, \tag{4.2}$$

where $W_H(t)$ is a sliding window function. In the present analysis a Hanning-type window function [191]

$$W_H(t) = \frac{1}{2} \left[1 + \cos\left(\frac{\pi t}{\Delta T} \right) \right] \tag{4.3}$$

with a FWHM ΔT of 150 fs is used. $S(\omega, \tau)$ represents the Fourier amplitude spectrum at the gate delay τ. All the reports using this technique so far were in the gas-phase systems which vibrational dephasing times are much longer than ten picoseconds. By applying this technique to condensed-phase molecules such as PDAs, it is expected that a dynamic behavior of the molecular motions may be seen at a glance as an exchange of a loss of frequency resolution, and useful informations about thermalization processes induced by vibration-vibration energy scrambling among several modes and conformational changes such as isomerization are expected to be extracted.

The spectrograms $S(\omega, \tau)$ of the oscillating components in Fig. 4.14 are shown in Fig. 4.15, which well expresses the time-frequency dependence of the molecular motion in the transient transmittance changes of the PDA. The spectrograms clearly

exhibit an interesting feature of mode-frequency modulations. The fine structures are well reproducible except for those in the spectrograms at 2.12 and 1.96 eV. The fast decay of the oscillations at these probe photon energies prevents the precise calculation of the spectrogram at a longer delay time than 500 fs.

The time dependence of the transient amplitudes and center-of-mass frequencies at the three characteristic stretching modes is shown on the right side of each spectrogram. For $E_{probe} < 1.9$ eV the oscillations give the similar features: the frequencies of the C–C and C=C stretching modes are modulated with the opposite phase to each other, whereas the frequencies of the C≡C stretching mode show weaker modulations and seem to be almost independent from the other modes. Over the three lower probe energies the modulations are in almost the same phase. Also observed is the red-shifts of the frequencies of the C=C and C≡C stretching modes form Raman frequencies by ~10 cm^{-1}. These features are visualizing the geometrical relaxation of the backbone. The details will be discussed in the following section.
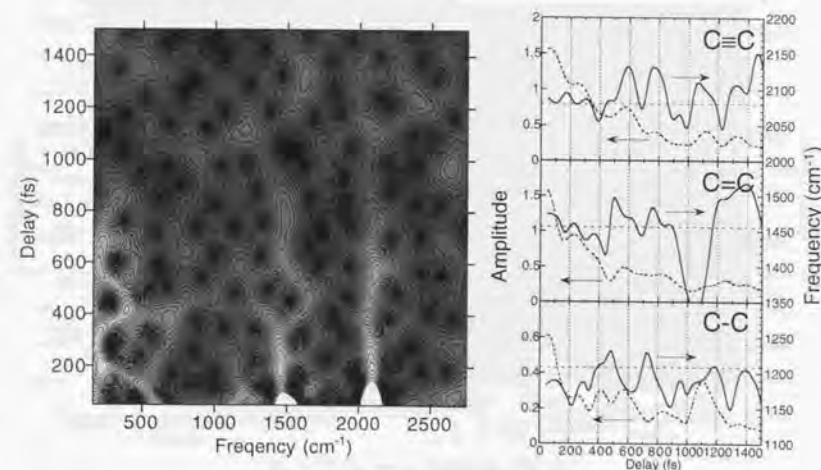
Fig. 4.15 (a) Spectrogram at 2.12 eV. The Fourier amplitude increases from black to white. The center-of-mass frequency (solid curve) and integrated amplitude (dashed curve) of each stretching mode are shown on the right. The thin dashed lines indicate the corresponding Raman frequency positions measured in the static resonance Raman scattering. The bandwidth for the integration is 200 cm^{-1} (also in Fig. 4.15 (b)–(e)).
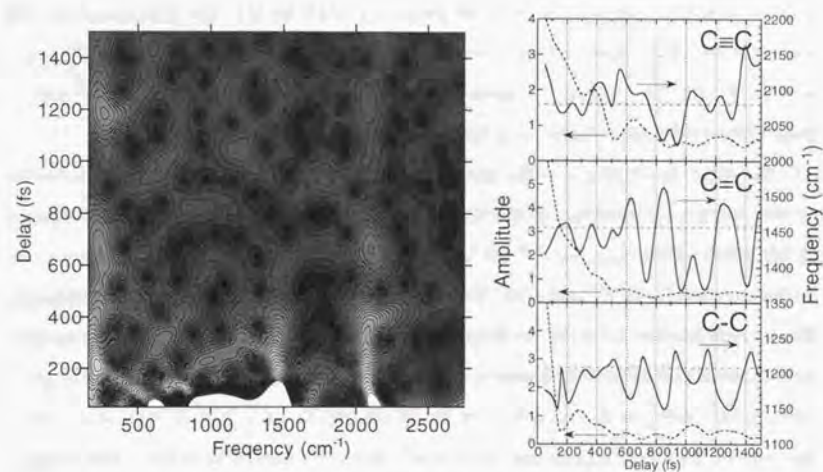
Fig. 4.15 (b) Spectrogram at 1.96 eV.

Fig. 4.15 (d) Spectrogram at 1.78 eV.

Fig. 4.15 (c) Spectrogram at 1.88 eV.
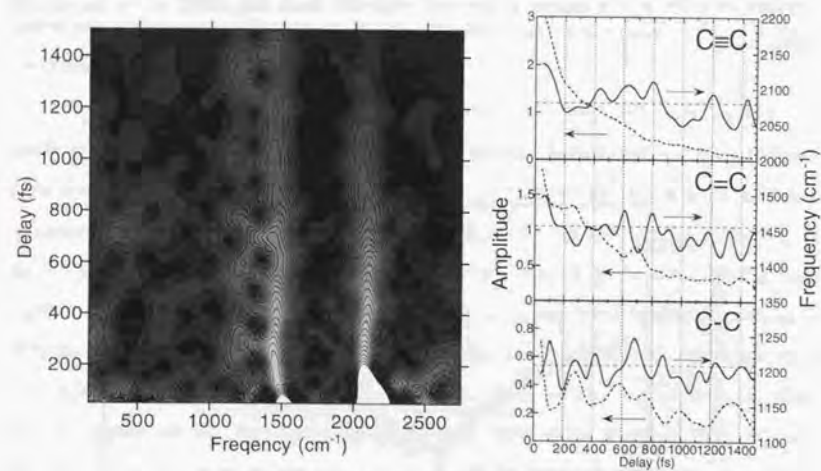
Fig. 4.15 (e) Spectrogram at 1.75 eV.

4.4.5. Phase of Oscillations

It is also important to elucidate the energy dependence of the phase of each stretching mode over the wide spectral range. Fourier transformation is performed with an integration range from 100 to 500 fs to separate the contributions of the initial FE state. Because the mode frequencies are modulated, each phase is obtained by averaging the angular part of the complex Fourier amplitude with the bandwidth of 200 cm^{-1} around 1220, 1440, and 2060 cm^{-1}. The results for the three stretching modes are shown in Fig. 4.16. The size of error is determined by the precision of the zero-delay (2 fs). The behavior of each phase is quite similar, presenting the phase retardation on both energy sides, as clearly observed in Fig. 4.10. Also shown is the phase of the 230 cm^{-1} mode averaged over a 150-cm^{-1} bandwidth, which is well observed in the bleaching signal especially for E_{probe} > 1.9 eV (Fig. 4.14). It also shows the similar probe energy dependence. These facts offer an evidence that the phase changes over the probe energies does not originate from any chirp of the pump and probe pulses.
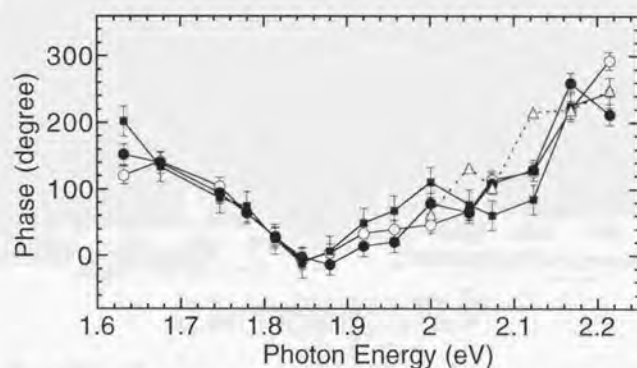
Fig. 4.16. Probe photon energy dependence of the phases of the vibrations of C–C (open circles), C=C (full circles), and C≡C (full squares) stretching modes. Also shown is that of the phase of the mode at 230 cm^{-1} observed at the higher probe photon energy (open triangles).

4.5. Discussion

4.5.1. Internal Conversion to Self-trapped 2^1A_g State

The behavior of electronic components after the photo-excitation seems to be well explained by the conventional self-trapping model [146,147,149]. The ~80-fs time constants observed for E_{probe} < 1.8 eV can be explained by the suppression of the SE and the creation of the STE. Yasuda *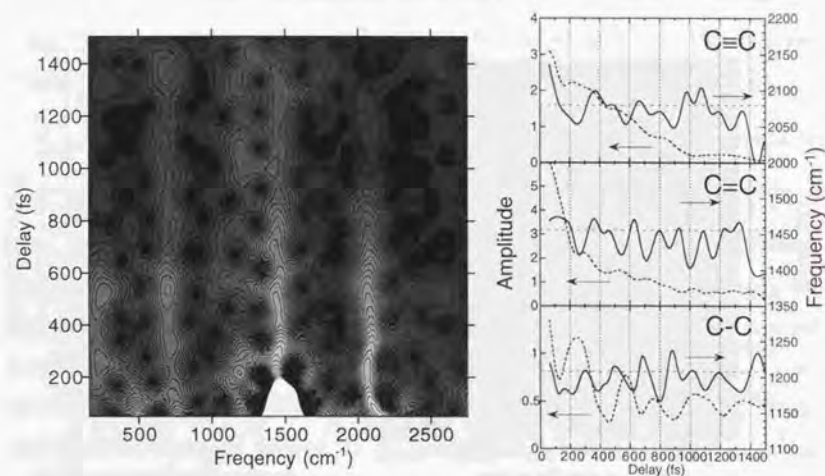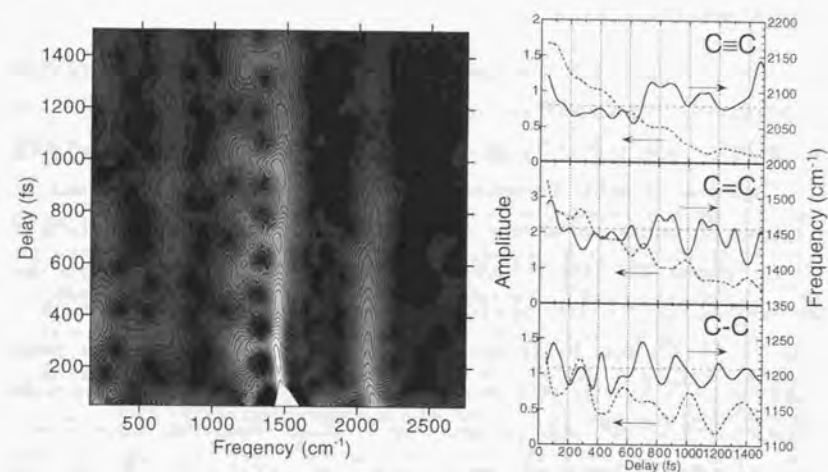et al.* extracted the SE spectra in a PDA-C$_4$UC$_4$ (R = R' = (CH$_2$)$_4$OCONH(CH$_2$)$_3$CH$_3$) oriented film by using a technique of probe saturation spectroscopy and explained that the 140-fs decay constant of the SE is due to the self-trapping from a FE to a STE [150]. Yoshizawa *et al.* reported an up-conversion experiment of a blue-phase PDA-3BCMU cast film and observed a 130-fs decay of a weak fluorescence [192]. Present experimental observation is quite consistent with these results, except for the shorter lifetime partly due to the high time resolution.

However, it is difficult to explain the fast damping time of 60–80 fs if the STE has the B$_u$ symmetry. The most probable explanation of the 60–80-fs process is an internal conversion (IC) to the lowest singlet 2^1A_g state. A theory indicates that in polyenes including PDAs a 2^1A_g state becomes below a 1^1B_u state with the increase of the repeat units by a strong electron correlation interaction [163]. Experimental results also support this prediction. It was observed that a weak two-photon fluorescence excitation spectrum exists below the edge of the linear absorption spectrum in a diacetylene oligomer, indicating that it has a 2^1A_g state ~0.2 eV below the 1^1B_u state [158]. Spectra of the third-order susceptibility have also revealed this property [159,161]. The recent experiment of a broadband third-harmonic generation of a PDA-TPCLP (8-(4-bromophenylthio)-5,7-octadiyne-N-(p-chlorophenyl)carbamate) oriented film clearly shows the enhancement of the third-order nonlinear susceptibility, which is well explained by the two-photon resonance to a 2^1A_g state ~0.1 eV below the 1^1B_u FE [162]. Today the picture that a 2^1A_g state exists below the 1^1B_u state in PDAs is

widely accepted [153,154,161,164].

We use the term "2^1A_g state" since there is no experimental verification of the existence of excitons in the 2^1A_g state [153]. Tanaka *et al.* calculated the property of an exciton in a ^1A_g symmetry and obtained the wavefunction of a charge-transfer-type exciton, the electron and hole existing at the nearest neighbor sites with the largest amplitude [193]. This feature seems to well express the picture of a STE (Fig. 4.1(c)). However, it is to be noted that their prediction that the 2^1A_g exciton is lying more than 0.7 eV above the 1^1B_u FE is contradictory to the present model. Zerbetto reported a calculation about the structure of a diacetylene oligomer $C_{14}H_8$ by an *ab-inito* and QCFF/PI methods [194], which indicates that the 2^1A_g state has nearly a butatrienic structure while the 1^1B_u state shows the medium property between the acetylenic and butatrienic structures. In the case of a PDA with an infinite main chain, the change of the π bond-orders will be reduced by the spread of the excitation to a few units by charge transfer [193]. It may, however, be reasonable to assign the 2^1A_g state to be the final geometrically-relaxed state in the butatriene-like configuration localized in the main chain.

The model is as follows. A photo-generated 1^1B_u FE is self-trapped and converted to a 1^1B_u STE within the vibrational periods of the stretching modes (10–20 fs), as mentioned below. The broadband SE corresponds to the transitions from the 1^1B_u FE/STE to the ground state and its broad phonon sidebands. The SE is quickly-damped by the IC to the nonfluorescent self-trapped 2^1A_g state* with a ~60–80-fs lifetime. The longer lifetime of the SE in the lower photon energy may represent the dynamic Stokes shift before the IC. The time constant of ~60–80 fs is considered to be reasonable if we compare it with the previous study by Kandori *et al.* [195], who determined the time constant to be ~200 fs for the nonradiative transition of S_2 (1^1B_u) → S_1 (2^1A_g) in β-carotene with the gap energy of ~0.4 eV.

---

* In the case of absence of excitons in a 2^1A_g state, it may be appropriate to use the term "geometrically-relaxed 2^1A_g state" in place of "self-trapped 2^1A_g state". In this thesis the term "self-trapped 2^1A_g state" is used for simplicity.

After the IC the PIA from the self-trapped 2^1A_g state becomes dominant. The final state of the PIA may be possibly a n^1B_u state. The PIA decays with the time constant of 1.5 ± 0.1 ps. This lifetime can be well explained by the tunneling model, in which the lifetime of the self-trapped state is characterized and determined by the FE energy [149,154]. The recovery of the ground-state population observed as the decay of the bleaching signal (880 ± 30 fs at 1.96 eV) is faster than the decay of the self-trapped 2^1A_g state. This is because in the self-trapped state a part of the population with the higher kinetic energy can relax to the ground state through a path without the potential barrier or with a very small barrier height [149,154]. The reason why the recovery time becomes faster at the higher probe photon energy is unknown.

The stationary fluorescence then originates only from the transition from the initial 1^1B_u FE/STE with a 60–80-fs lifetime. Because the radiative lifetime estimated from the oscillator strength of the 1^1B_u FE transition is a few nanoseconds [153], the characteristic low quantum yield of the order of 10^{-5} in blue-phase PDAs [131] is quantitatively explained. There is no contribution from the following nonfluorescent self-trapped 2^1A_g state, which is then returned to the ground state via the nonradiative tunneling process.

4.5.2. Origin of Coherent Molecular Motion

As clearly seen from the Fourier spectra in Fig. 4.14, the oscillating components are due to the creation of the wavepackets in the adiabatic potential surfaces. Because the wide range of the absorption spectrum including the phonon side bands (see Fig. 4.5) is excited coherently with the negligible phase distortion over a 150-THz (5000-cm^{-1}) range, the manifold of quantized vibrational levels are coherently added and constitute the well-confined nonstationary vibronic states which describe the classical nuclear motions. The complicated multimode motions on the potential surfaces should be depicted by multi-dimensional coordinates. As far as we know the oscillations with a period of 16 fs due to the C≡C stretching is the shortest among many works of the coherent molecular motion. In the temporal picture, it means that the excitation is well within the Born-Oppenheimer approximation even for such a high-frequency nuclear

motion. The shortest excitation pulse can minimize the defusing of the wavepackets on the potential surface within the excitation.

In general wavepackets are created on both the electronic ground and excited-state surfaces. The former process is induced by impulsive stimulated Raman scattering (ISRS) [196,197]. This process originates from the broad spectrum of the femtosecond pulses which can cause the stimulated Raman process within the bandwidth of one pulse. In the resonant case it has been shown that the ground-state wavepacket is dominantly caused by the coherent interaction with the excited state, which transfers the momentum from the instantaneously sliding wavepacket formed on excited-state surface to a "hole" wavepacket on the ground-state surface [196,197]. This ground-state wavepacket sometimes dominates the oscillating signal in the differential transmission [169], therefore it is of vital importance to determine the origin of the oscillation to investigate the ultrafast dynamics.

As discussed in the former section the behavior of the electronic components well indicates that the photo-generated 1^1B_u FE state is self-trapped and then experiences the IC to the nonfluorescent self-trapped 2^1A_g state. This process is well reflected on the quickly-damped SE with the time scale of 60–80 fs, then followed by the appearance of the PIA from the self-trapped 2^1A_g state to the upper-lying n^1B_u state. Therefore the initial strong oscillations observed in the SE (see Fig. 4.10) dominantly represent the molecular motion in the 1^1B_u STE. The quick appearance of the wavepackets clearly indicates the self-trapping process occurs within 10–20 fs. Because the transition from a 2^1A_g state to a 1^1A_g ground state is optically-forbidden, after the IC the wavepacket motion on the excited state is not expected in the bleaching signal. As shown in Fig. 4.10, the behavior of the transmittance changes for $E_{probe} > 1.9$ eV clearly supports this expectation. Just after the photo-excitation, the well-contrasted strong oscillations are created and rapidly damped after only a few oscillations, together with the annihilation of the SE. The weak oscillations then continue for ~1 ps, indicating that the wavepacket motion in the ground state is driven by the ISRS.

On the other hand, the oscillation behaviors for $E_{probe} < 1.8$ eV, where the PIA is dominant, are of interest with different features. The strong wavepacket motion is kept for more than 1 ps, and it has a maximum amplitude around the delay time of 100–300 fs. This behavior strongly indicates that the wavepacket is created on the potential surface of the self-trapped 2^1A_g state. The red-shifting features of the transient oscillating frequencies from the static Raman frequencies are also consistent. The previous experiment investigating the resonance Raman excitation profile of a PDA-PTS (2,4-hexadiyne-1,6-diol) crystal exhibited the 30–60-cm^{-1} frequency down-conversion of the three stretching modes in the 1^1B_u state with respect to those in the ground state [178]. However, there is no observation about the vibronic property of the 2^1A_g states. A theoretical calculation about $C_{14}H_8$ indicates the similar change between modes in the ground and 2^1A_g states, except for the up-conversion of the C–C modes by 6 cm^{-1} [194]. In the case of a PDA the smaller frequency change is expected by a spread of the excitation. It is of great interest to see that the coherence of the initial wavepacket motion on the 1^1B_u surface is transferred to the self-trapped 2^1A_g state via the IC without substantial degradation.
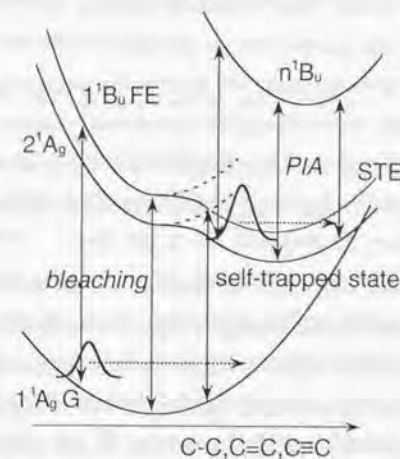

Fig. 4.17. Explanation of the probe photon energy dependence of the phase of the oscillations in each species after the internal conversion. For simplicity the surface of the STE is written by gray line.

The interpretation of a coherent molecular motion is strongly supported by the probe energy dependence of the phases of the oscillations shown in Fig. 4.16. The behavior can be clearly separated to two regions with the opposite slopes. The phase should be dependent on the probe photon energy due to the wavepacket motion on the potential surfaces, as schematically depicted in Fig. 4.17. Here the n^1B_u state is thought to have the displaced potential with respect to the self-trapped state. Thus the energy separations between two of these potentials have the different dependence on the nuclear positions. The PIA at a higher photon energy becomes stronger when the wavepacket is closed to the original 2^1A_g state, whereas that at a lower photon energy becomes weaker. Therefore the oscillations of the PIA at the higher energy side of ~1.85 eV is 180° ahead of those at the lower energy side of ~1.6 eV. In the similar way, the oscillations of the bleaching in the transition from the ground state to the excited state is expected to reverse the phase between ~1.85 and ~2.2 eV. In this case the observed ~250° retardation seems to be slightly larger. Bardeen *et al.* observed the phase retardation of 270° across the absorption band in dye solution [186]. In their case the oscillating signal is composed of the wavepackets in both the ground and excited states, thus the enhancement is expected to take place when both wavepackets evolve out-of-phase. In the present case the situation is different because Figure 4.16 represents the behavior after the initial 100 fs when the wavepacket in the 1^1B_u state is annihilated. The probable explanation is that around the boundary region (1.8–1.9 eV) the signal is composed of the two transitions between the ground and 1^1B_u states and between the 2^1A_g and n^1B_u states, which is also expected to introduce the excess phase retardation.

The stretching modes coupled to the excitons are the driving force of the self-trapping process, and the relaxation energy triggers the wavepacket motion in the self-trapped states. Experimentally it is of no doubt that the wavepacket is generated in the self-trapped 2^1A_g state by the coherence transfer from the wavepacket generated in the 1^1B_u FE state. It is interesting that the oscillations do not decay through the IC. To explain this feature it can be considered as follows. The wavepacket in the 1^1B_u state leaks on both sides of the potential surface, then in the 2^1A_g state every leak is

coherently summed and then after 80 fs the wavepacket is reconstructed without a substantial distortion. From the above finding it can be concluded that the curvatures of the two potential surfaces are equal to each other. This is supported by a calculation about $C_{14}H_8$ [194], which shows the mode-frequency differences of the three stretching modes are all less than 10 cm^{-1} between the 1^1B_u and 2^1A_g states. After the IC, the wavepacket motion is kept for ~1 ps and decays via the nonradiative tunneling process to the ground state [149].

It seems that the vibrational dephasing time of each mode on the ground and self-trapped state can be determined by the time dependence of the oscillating amplitude. However, because the damping time is strongly dependent on the initial formation conditions such as the phase of excitation pulses [186,198,199], it is not appropriate to extract the vibrational lifetime or dephasing time from this kind of experiment of a real-time molecular motion [186]. In fact, the dephasing time of the C=C stretching mode in the ground state was reported to be longer than 8 ps in a cast film of red-phase PDA-4BCMU, which was measured by coherent anti-Stokes Raman spectroscopy [200]. The long-living features of the oscillations in the PIA may possibly indicate that the dephasing time is nearly the same as or longer than the 1.5-ps lifetime of the self-trapped state.

4.5.3. Stretching–Mode Coupling with Bending Motion

As clearly observed in the spectrograms (Fig. 4.15), the instantaneous mode frequencies are modulated after the photo-excitation. This interesting feature is observed for all probe energies, but in the bleaching the oscillations suffer from a quick damping which prevents a reliable observation. For $E_{probe} < 1.9$ eV the modulations are mainly due to the wavepacket motion in the self-trapped state. The long-living feature is advantageous for the investigation of this modulation. The fine structures of the dynamic mode-frequency changes can be well reproduced and show a similar behavior across the PIA region. In Fig. 4.18 the center-of-mass mode frequencies and corresponding integrated amplitudes at 1.75 eV are shown again.

The mode frequencies of the C–C (ν_{C-C}) and C=C ($\nu_{C=C}$) stretching modes are

modulated out-of-phase from each other. On the other hand, the $C\equiv C$ stretching mode ($\nu_{C\equiv C}$) seems to behave relatively independently, and the relative modulation depth is also smaller than the former two modes. These features can be explained by the self-trapping, which deforms the acetylenic backbone structure $(=CR-C\equiv C-CR=)_n$ to the butatrienic structure $(-CR=C=C=CR-)_n$ localized in a few units in the main chain. The stretching modes coupled with the exciton drives this isomerization, and after this process the coherent nuclear motion stays around this local deformation. In the local butatrienic unit there are only the $C-C$ and $C=C$ bonds, so that the above dynamic property is concentrated on these two modes. Actually, the bond alternation may partly occur since we can observe the smaller red-shifts of the mode frequencies than the
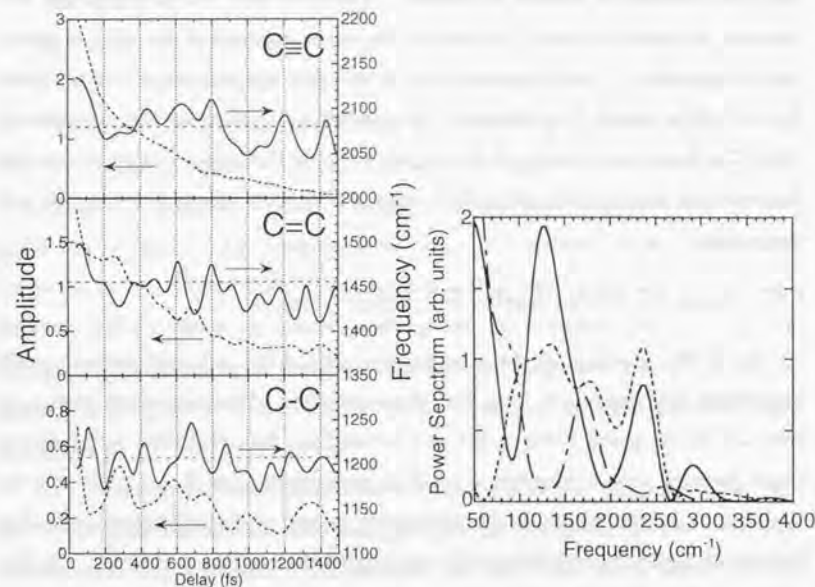

Fig. 4.18. Properties of the frequency oscillations of the stretching modes at 1.75 eV. The instantaneous frequencies (solid curves) and amplitudes (dashed curves) are shown for the three modes. On the right shown is the Fourier power spectra of these oscillations of $C-C$ (solid curve), $C=C$ (dashed curve), and $C\equiv C$ (dashed-dotted curve) stretching modes after eliminating the offsets.

prediction. It may be appropriate to describe that the π bond-orders of the $C=C$ $(1 - \delta_0)$ and $C\equiv C$ $(2 - \delta_0)$ bonds decrease to $1 - \delta$ and $2 - \delta$, respectively, where δ_0 and δ $(\delta_0 < \delta < 1)$ are the π bond-orders of the $C-C$ bond in the ground state and equilibrium self-trapped 2^1A_g state.

The Fourier spectra of the frequency modulations in the three modes are shown on the right side of Fig. 4.18. ν_{C-C} and $\nu_{C=C}$ have modulation frequencies at 230 cm^{-1} and around 130 cm^{-1}. This ~230-cm^{-1} frequency is also observed in the coherent wavepacket motion, especially for $E_{\text{pmbe}} > 1.9$ eV (see Fig. 4.14). This mode can be assigned to a planar bending mode of $C-C=C$ bonds. This lies in the typical frequency range of the CCC bending modes of olefines and alkynes [187]. From recent *ab-inito* calculations, it has been shown that these bending modes have large Franck-Condon activities in molecules such as octatetraene (C_8H_{10}, 220–400 cm^{-1}) [201] and diacetylene oligomers ($C_{14}H_8$, ~160 cm^{-1}) [194] as prototypes of the PAs and PDAs, respectively. Even though the dimensionless displacements (B factors) between the ground and excited states are the same orders as those of stretching modes, these contributions have not been clearly observed experimentally in the absorption, fluorescence, or resonance Raman spectra due partly to the low frequency, and the importance has not been noticed.

Even though the bending mode has such a low frequency, the wavepacket motion has not been observed in any of previous reports on the time-resolved spectroscopic studies of PDAs to our knowledge. The coupling feature was firstly and only observed by Nunzi *et al.* [188]. They performed a dynamic hole burning spectroscopy [182,184] of a blue-phase PDA-4BCMU film and observed the creation of holes at both sides of the exciton energy with the separation of 290 cm^{-1}, which was explained by the planar bending mode in the backbone. A large Franck-Condon factor was estimated from the hole depths even though the corresponding Raman peak was quite weak [188]. This mode may correspond to the 230-cm^{-1} mode observed here. The frequency change may be explained by the linkage of the two backbones by methylene chains in PDA-4BCMU4A(8). Our result is the first observation of the coherent wavepacket formation of this bending mode.
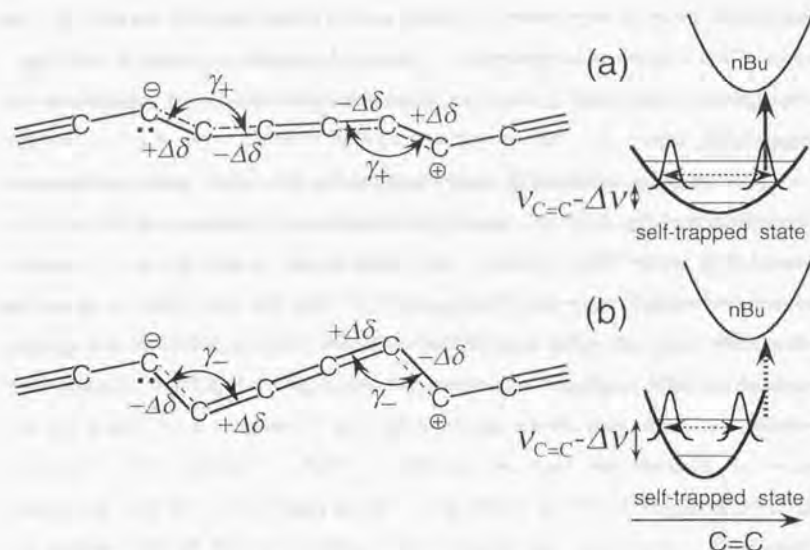
Fig. 4.19. Bending motion around the lattice deformation created by the self-trapping. The butatriene-like backbone is locally constructed, which has a large kinetic energy through the coherence transfer from the FE, and the stretching and bending motions are active. Between the states with different bending angles ((a) and (b)) the force constants of the C–C and C=C bonds are different, resulting in the modulation of the π bond-orders and the bond-length. Thus both of the frequency and amplitude are modulated by the bending motion. The right pictures are the schematic of the corresponding instantaneous potentials projected to the coordinate representing the C=C distance, which explains the change of the transition probability due to the force-constant modulation. The frequency and amplitude experience out-of-phase oscillations with each other.

For $E_{probe} < 1.9$ eV the Fourier peak around 230 cm^{-1} is weakened and disappeared at 1.75 eV, even with the long-living oscillations (see Fig. 4.14). However, the large Franck-Condon activity of this mode can create well-confined wavepackets both on the ground and excited-state potential surfaces especially due to the long oscillatory period (~150 fs). After the self-trapping and IC, the excited-state wavepacket can still remain by the mechanism mentioned before. If the Franck-Condon factor of this mode between the self-trapped state and the upper-lying state is small, the PIA signal cannot

contain a clear oscillations corresponding to this bending motion.

The frequency modulations of v_{C-C} and $v_{C=C}$, on the other hand, clearly indicate the formation of this bending motion after the geometrical relaxation to the butatriene-like configuration. Because the equilibrium positions of the carbon atoms and the bond angle of C–C=C are different from those in the acetylenic configuration [202], the coherent vibrations of the stretching modes and the C–C=C bending mode continue till thermalization. The self-trapped state is not thermalized before the tunneling to the ground state, and these nuclear motions are then well observed for ~1.5 ps. In such non-equilibrium states the bending motion perturbs both force constants of the C–C and C=C stretching modes. Figure 4.19 illustrates the mechanism. For simplicity the case of a fully butatrienic structure is considered, with the position of the single and double bonds alternated. If the bond angle is decreased, the bond-order in the C–C bond is increased while that in the C=C bond decreased, which causes the corresponding frequencies to be up-converted and down-converted, respectively. In the opposite case the changes are reversed, resulting in the out-of-phase modulations of v_{C-C} and $v_{C=C}$. The out-of-phase property between each amplitude and frequency can also be easily explained as follows. The potential curve intersected along the corresponding normal coordinate is modulated by the bending motion: in the case of a larger frequency of the stretching mode, the potential curve is steepened and the amplitude of the wavepacket motion is confined, which is reflected on the $\Delta T/T$ as a smaller oscillation amplitude by the reduction of the overlap integral with the upper-lying state.

The amounts of the modulated bond-length and bond-orders can be estimated from the frequency modulation. Lewis et al. introduced an empirical relation [177]

$$r_{ij} = r_0 + \frac{B}{K_{ij}},$$

(4.4)

where the stretching force constant K_{ij} between two atoms i and j is related to the bond-length r_{ij}. The parameters $r_0 = 0.106$ nm and $B = 1.65 \times 10^{-8}$ N were evaluated in the case of PDA-PTS. Batchelder et al. estimated K_{ij}'s in the excited state as $K_{C-C} = 474$ N/m and $K_{C=C} = 481$ N/m [178]. Here the subscripts denote the bonds in the

acetylenic configuration.

The mode frequenciy v_j generally depends on all the force constants including the bending modes. Because the modulation depths of $v_{C\equiv C}$ and bending modes cannot be measured, we assume the coupling between the two stretching modes is important, i.e.,

$$\begin{pmatrix} \Delta v_{C-C} \\ \Delta v_{C=C} \end{pmatrix} = \begin{pmatrix} \dfrac{\partial v_{C-C}}{\partial K_{C-C}} & \dfrac{\partial v_{C-C}}{\partial K_{C=C}} \\ \dfrac{\partial v_{C=C}}{\partial K_{C-C}} & \dfrac{\partial v_{C=C}}{\partial K_{C=C}} \end{pmatrix} \begin{pmatrix} \Delta K_{C-C} \\ \Delta K_{C=C} \end{pmatrix}. \tag{4.5}$$

The differential coefficients $\dfrac{\partial v_j}{\partial K_{ij}}$ are given in Table 3 in ref. [203] for a PDA-PTS crystal in a ground state and $\dfrac{\partial v_{C-C}}{\partial K_{C-C}} = 0.57, \dfrac{\partial v_{C-C}}{\partial K_{C=C}} = 0.12, \dfrac{\partial v_{C=C}}{\partial K_{C-C}} = 0.31,$ and $\dfrac{\partial v_{C=C}}{\partial K_{C=C}} = 0.77 \, \text{m/N} \cdot \text{cm}$. There is no information about the excited state, which limits us to use these coefficients for the first calculation.

The modulation depths Δv_{C-C} and $\Delta v_{C=C}$ are evaluated as standard deviations of the instantaneous frequencies in Fig. 4.18 yielding both ~16 cm^{-1}. Eq.(4.5) then gives the modulation depths of the force constants (ΔK_{ij}'s), and from Eq.(4.4) the modulated bond-lengths are estimated as $\Delta r_{C-C} = \pm 0.0026$ nm and $\Delta r_{C=C} = \mp 0.0025$ nm. Using $r_{C-C} = r_{C=C} = 0.14$ nm in the excited state [178], the relative modulations of r_{C-C} and $r_{C=C}$ are ± 1.9 % and ∓ 1.8 %, respectively.

The modulation of the π bond-orders are estimated by using the simple relationship between the mode frequency and bond-order derived by Baughman *et al.* [176]. They investigated π-electron delocalization in many PDAs with different Raman frequencies of stretching modes. Empirical relations for the bond-lengths of sp–sp and sp^2–sp^2 bonds were used the mode frequencies were tabulated with respect to the π bond-order δ of a C–C bond. The obtained coefficient $dv_{C=C}/d\delta = 512.4$ cm^{-1} in the case of Dewar's relationship [204] well explained the mode-frequency distribution of the C=C stretching. If this is also valid in the 2^1A_g state of a PDA-4BCMU4A(8), the modulation depth $\Delta\delta$ is given as ± 0.031 from $\Delta v_{C=C}$. In the case of $r_{C-C} = r_{C=C} = 0.14$ nm, $\delta = 0.41$ [204] then the relative modulation is estimated as

7.6 %.

These estimations are based on many assumptions. First, we use the values of PDA-PTS investigated in detail because there is no such experiments about PDA-4BCMU4A(8). Second, in ref. [178] K_{ij}'s and r_{ij}'s in the excited state were estimated by measuring resonance Raman excitation profiles, which only reflects the molecular structure in the 1^1B_u state and includes no information about the 2^1A_g state. Third, the values of $\dfrac{\partial v_j}{\partial K_{ij}}$ in the ground state is used with the assumption of Eq.(4.5). Finally, Dewar's relationship used in ref. [176] is based on the assumption that in determining bond-lengths π-election resonance is much less important than hybridization when only one classical structure of the molecule can be written [204]. The π-electron resonance is, however, to be non-negligible in a strongly electron-correlated system such as a PDA. It should be noted that the present analysis only gives the zeroth-order approximation.

As mentioned before the isomerization is not perfect and the backbone may be only "butatriene-like". The C≡C bond is remained in the center of the butatriene-like unit with the reduced bond-order and also vibrating. However, because the bond is not connected with the bending part of C–C=C, it may experience negligible effects by the bending motion and evolve almost independently. The modulation amounts of the bond-lengths and bond-orders mentioned above may be overestimated because of the assumption of a perfectly delocalized structure ($r_{C-C} = r_{C=C}$) between the acetylenic and butatrienic configurations. In fact it is a quite difficult problem to determine the amounts of the bond-orders in the 2^1A_g state.

As far as we know, this is the first observation of the diabatic coupling between normal modes via the vibration of other modes. This phenomenon is expected to be broadly observed in such a photo-excited non-equilibrium system in the shortest time scale.

4.5.4. Coherent Geometrical Relaxation

As we have discussed above, we could visually observe the ultrafast geometrical

relaxation process in the PDAs for the first time. Figure 4.20 presents the elucidated feature of the dynamic self-trapping shown with the potential surfaces. The photo-generated FEs are coupled with the carbon stretching modes and quickly self-trapped within 10–20 fs. The IC from the 1^1B_u STE to the 2^1A_g state follows with the damping of the SE with a time constant of 60–80 fs. The wavepacket motion in the self-trapped 2^1A_g state is transferred coherently from the FE via the IC without any degradation. The self-trapped (geometrically-relaxed) 2^1A_g state is the final state of the photo-isomerization, being expected to have more butatrienic configuration than the 1^1B_u state. The non-equilibrium self-trapped state is characterized by the coherent stretching and bending motions around the constructed butatriene-like backbones localized in the main chains, where the C–C and C=C bonds exchange the vibration energy with each

other via the bending motion. The coherent self-trapped state is then damped nonradiatively via the tunneling process at the crossing with the ground state with a 1.5-ps decay time.

We investigated PDA-4BCMU4A(8), which is one of the various PDAs. Because the dynamics predominantly originates from the electrons confined along the main chain, the PDAs are known to show the common kinetics independent from the side groups and sample form, with only the exception of red-phase PDAs [153]. It is believed that the coherent motions of the C=C and C≡C stretching along the backbone act as the driving force of the self-trapping and the geometrical change to the butatrienic configuration. The present result will offer a valuable information about the geometrical relaxation and encourage the theoretical investigations of the election-phonon and electron-electron interactions in non-degenerate conjugated polymers. for the quantitative understanding of this characteristic coherent features.

Fig. 4.20. Model of the geometrical relaxation dynamics in PDAs elucidated in this work.

5. Conclusions

Noncollinear optical parametric amplification (NOPA) has been investigated for the generation of extremely short optical pulses. The noncollinear geometry can realize a group-velocity matching between the signal and idler, which is equivalent to an achromatic phase matching with the spectral angular dispersion, and the broadest gain bandwidth is attained. The basic principle is demonstrated in an OPA based on a β-BaB_2O_4 crystal. It is shown that the pulse-front tilting accompanying the noncollinear interaction limits the pulse-width shortening. A pulse-front-matching geometry is introduced and transform-limited sub-8-fs pulse generation is succeeded with the advantageous tunability between 550 and 700 nm. The angular-dispersion compensation of the idler realizes sub-9-fs pulses also in the near-infrared. The shortest 4.7-fs visible pulses are achieved by a compressor composed of a prism pair and customized chirped mirrors with the bandwidth of broader than 200 THz. The NOPA is the first tunable sub-10-fs pulse generator as well as the first sub-5-fs light source by other methods than the conventional continuum-compression scheme. Also remarked is the future prospects of this NOPA.

The NOPA is applied for the investigation of the ultrafast geometrical relaxation process in polydiacetylenes. A high-frequency long-living wavepacket motion is observed, which contains vibrations of the three carbon stretching modes and a planar bending mode. Both features of the electronic and molecular dynamics indicate the coherent relaxation from a free exciton to a self-trapped state within 80 fs via the internal conversion from a 1^1B_u state to a 2^1A_g state. The time-frequency analysis visualize the coherent geometrical relaxation and the highly vibronic non-equilibrium state is characterized by the instantaneous mode frequency and amplitude modulations at 230 cm^{-1}. This feature is well explained by the diabatic coupling of the stretching modes via the vibration of the planar bending mode in the local butatriene-like backbone. This is the first observation of such diabatic molecular motions.

The NOPA has many advantageous aspects such as a tunability, pulse energy,

flexible pulse width and bandwidth, which is believed to be the most useful light source for ultrafast spectroscopy of various materials. The properties of the broad bandwidth and shortest durations are quite useful for the real-time observation of an ultrafast molecular vibrational dynamics and structural change in photo-chemical reactions. These features will open the door to explore unknown phenomena on an extreme time scale, and will lead to a new regime in ultrafast science.

Appendix A. Pulse-front Tilting

An ultrashort pulse has a thin volume in which the electric field exists. For example, a 100-fs pulse has only a 30-μm thickness. On the other hand, the beam cross section in general is an order of millimeters. Thus the time-space coupling across the cross section by some distortion of propagation can give a tilted pulse volume from the wave front. This is called as a pulse-front tilting, resulting in a pulse-width broadening and spectral lateral walk-off.

As a simple example, we consider a pulse propagation through a prism (Fig. A.1) [84]. The beam 1 and 2 are rays propagating along both edges of the cross section. As a basic principle of the wave front,

$$AB + AC = nB\,C, \tag{A.1}$$

where n is the refractive index of the prism. Because the pulse propagation in the prism is described by the group velocity $v_g = \dfrac{c}{n - \lambda\,dn/d\lambda}$, a time difference is caused across the cross section:

$$\Delta T = \frac{B\,C}{v_g} - \frac{AB + AC}{c} = -\frac{B\,C}{c}\lambda\frac{dn}{d\lambda}, \tag{A.2}$$

where Eq.(A.1) is used. Therefore the pulse front which is defined as "the surface coinciding with the peak intensity of the pulse" [86] is tilted from the wave front by an
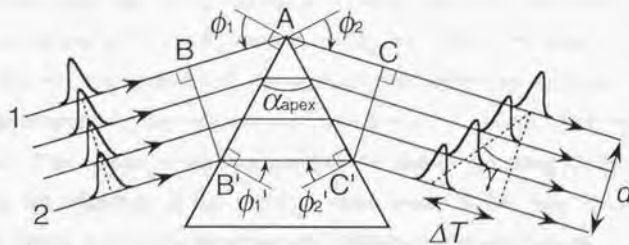
Fig. A.1. Schematic of the pulse-front tilting by the propagation through a prism. ϕ_1, $\phi_1{}'$, external and internal incident angles; ϕ_2, $\phi_2{}'$, external and internal exit angles.

angle γ satisfying the relation

$$\tan\gamma = \frac{c\Delta T}{d} = -\frac{B\,C}{d}\lambda\frac{dn}{d\lambda}, \tag{A.3}$$

where d is the beam diameter after the prism.

The relation for a prism with an apex angle α_{apex} and the Snell's law are

$$\phi_1{}' + \phi_2{}' = \alpha_{apex}, \tag{A.4}$$

$$\sin\phi_1 = n\sin\phi_1{}', \tag{A.5}$$

$$\sin\phi_2 = n\sin\phi_2{}'. \tag{A.6}$$

Differentiating Eq.(A.5) and using Eq.(A.4) yield

$$\frac{\partial\phi_2{}'}{\partial\lambda} = -\frac{\partial\phi_1{}'}{\partial\lambda} = \frac{\tan\phi_1{}'}{n}\frac{dn}{d\lambda}, \tag{A.7}$$

for ϕ_1 = const.. Similarly, by differentiating Eq.(A.6) and using Eqs.(A.4) and (A.7), we obtain

$$\frac{\partial\phi_2}{\partial\lambda} = \frac{\sin\alpha_{apex}}{\cos\phi_1{}'\cos\phi_2}\frac{dn}{d\lambda}. \tag{A.8}$$

By substituting Eq.(A.8) into Eq.(A.3) and using the geometrical relations $d = AC\cos\phi_2$ and $B\,C\cos\phi_1{}' = AC\sin\alpha_{apex}$, we obtain a simple formula

$$\tan\gamma = -\lambda\frac{\partial\phi_2}{\partial\lambda}. \tag{A.9}$$

Thus it is shown that the angular dispersion caused by the deflection at a prism originates the pulse-front tilting.

General Formalism

It can be generally said that an angular dispersion generated in a pulse propagation corresponds to the pulse-front tilting. A generalized discussion is presented below based on the description by Martinez [85,205]. A "dipersor" which generates an angular dispersion can be characterized by the relation

$$\Delta\phi_2 = \eta\Delta\phi_1 + \kappa\Delta\omega, \tag{A.10}$$

where the deviation of the exit angle $\Delta\phi_2 = \phi_2 - \phi_{20}$ is expressed by both deviations of

the incident angle $\Delta\phi_1 = \phi_1 - \phi_{10}$ and the angular frequency $\Delta\omega = \omega - \omega_0$ to the first-order. The parameters η and κ characterize the dispersor. In the case of the example mentioned above, from Eqs.(A.4)–(A.6) yielding

$$\eta = \frac{\partial\phi_2}{\partial\phi_1} = -\frac{\cos\phi_1 \cos\phi_2{}'}{\cos\phi_1{}' \cos\phi_2}, \qquad (A.11)$$

and from Eq.(A.8) and $\omega = 2\pi c/\lambda = ck$

$$\kappa = \frac{\partial\phi_2}{\partial\omega} = -\frac{\lambda^2}{2\pi c}\frac{\partial\phi_2}{\partial\lambda} = -\frac{\sin\alpha_{apex}}{\cos\phi_1{}' \cos\phi_2}\frac{\lambda^2}{2\pi c}\frac{dn}{d\lambda}. \qquad (A.12)$$

We consider the propagation property of the amplitude $a(x, y, \Delta\omega)$ defined as the spectral component at $\omega = \Delta\omega + \omega_0$ of the electric field at a point (x, y) on a plane normal to the direction of propagation z. Here we assume the angular dispersion occurs only in the xz plane. The dependence of the amplitude on y is that given by propagation in free space and is included explicitly only when necessary for the discussion. We use a x_i-axis normal to each direction of propagation.

Figure A.2 explains the phase changes at the dispersor (a) for the incident angle change $\Delta\phi_1$ and (b) for the angular frequency change $\Delta\omega$, originating the exit angle change $\Delta\phi_2$. For (a), the phase experienced by the incident beam is

$$k(\sin\Delta\phi_1 \cdot x_1 + \cos\Delta\phi_1 \cdot z_1) \cong k(\Delta\phi_1 x_1 + z_1) \qquad (A.13)$$

whereas that by the exit beam is similarly given by $k(\Delta\phi_2 x_2 + z_2)$. For $z_1, z_2 \to 0$, both phases should be equal to each other, then $\Delta\phi_1 x_1 = \Delta\phi_2 x_2$, yielding

$$x_1 = \frac{\Delta\phi_2}{\Delta\phi_1}x_2 = \frac{\partial\phi_2}{\partial\phi_1}x_2 = \eta x_2. \qquad (A.14)$$

Similarly for (b) the phase experienced by the spectral component at ω is

$$k\Delta\phi_2 x_2 = k\kappa\Delta\omega x_2 \qquad (A.15)$$

for $z_2 = 0$. From Eqs.(A.14) and (A.15), we obtain the relationship between the amplitudes of the incident beam $a_1(x_1, \Delta\omega)$ and the exit beam $a_2(x_2, \Delta\omega)$:

$$a_2(x_2, \Delta\omega) = c_1 a_1(x_1, \Delta\omega)\exp(ik\kappa\Delta\omega x_2) = c_1 a_1(\eta x_2, \Delta\omega)\exp(ik\kappa\Delta\omega x_2). \qquad (A.16)$$

A set of constants $\{c_i\}$ is used thereafter for simplicity describing the energy
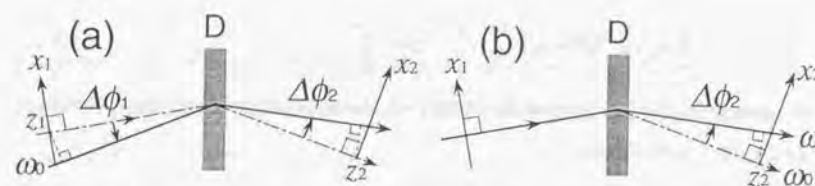
Fig. A.2. Origin of the phase changes by passing through an arbitrary dispersor (D). The exit angle change $\Delta\phi_2$ is caused in the case of (a) the incident angle change $\Delta\phi_1$ ($\Delta\omega = 0$) and (b) the angular frequency change $\Delta\omega$ ($\Delta\phi_1 = 0$).

conservation under the divergent beam propagation. More generalized derivation of Eq.(A.16) is also given in ref. [205].

A Gaussian spatial profile is assumed for the input beam [206]:

$$a_1(x_1, y, \Delta\omega) = a_{in}(\Delta\omega)\exp\left[-\frac{k(x_1^2 + y^2)}{2q(d_0)}\right], \qquad (A.17)$$

with

$$q(z) = z + i\frac{k\sigma^2}{2}, \qquad (A.18)$$

where σ is the $1/e^2$ radius for the beam waist and d_0 is the position of the beam waist, defined positive if it is located before the dispersor. The temporal amplitude is then given by

$$A_2(x_2, y, t) = \int a_2(x_2, y, \Delta\omega)e^{-i\Delta\omega t}d\Delta\omega$$
$$= c_1 \int a_1(\eta x_2, y, \Delta\omega)\exp[i(k\kappa x_2 - t)\Delta\omega]d\Delta\omega \qquad (A.19)$$
$$= c_1 \exp\left[-\frac{k(\eta^2 x_2^2 + y^2)}{2q(d_0)}\right]\int a_{in}(\Delta\omega)\exp[i(k\kappa x_2 - t)\Delta\omega]d\Delta\omega.$$

We consider the case of a Gaussian temporal profile for the envelope function

$$A_{in}(t) = A_0 \exp(-t^2/\tau_0^2), \qquad (A.20)$$

yielding

$$a_{in}(\Delta\omega) = \int A_{in}(t)e^{i\Delta\omega t} dt = a_0 \exp\left[-\frac{\tau_0^2}{4}(\Delta\omega)^2\right].$$ (A.21)

By substituting Eq.(A.21) into Eq.(A.19) we obtain the expression of the pulse-front-tilted temporal amplitude:

$$A_2(x_2, y, t) = c_2 \exp\left(-i\frac{k\eta^2 x_2^2 + y^2}{2q(d_0)}\right)\exp\left[-\left(\frac{k\kappa x_2 - t}{\tau_0}\right)^2\right].$$ (A.22)

The cross term $x_2 t$ clearly represents the time-space coupling. The delay of the time for the peak intensity at x_2 is $\Delta T = k\kappa x_2$. The tilt angle γ from the wave front ($x_2 y$ plane) normal to the direction of propagation is then given by the relation

$$\tan\gamma = \frac{c\Delta T}{x_2} = ck\kappa.$$ (A.23)

By substituting $\kappa = \dfrac{\partial\phi_2}{\partial\omega} = -\dfrac{\lambda^2}{2\pi c}\dfrac{\partial\phi_2}{\partial\lambda}$, we obtain

$$\tan\gamma = -\lambda\frac{\partial\phi_2}{\partial\lambda}$$ (A.24)

again. In this way it is shown that Eq.(A.9) is a formula generally satisfied in the pulse-front tilting generated by an arbitrary dispersor.

Propagation Property

Eq.(A.22) represents the amplitude at the dispersor just after the deflection. The amplitude at a distance z propagating from the dispersor is described by the Kirchhoff-Fresnel integral in an approximate form:

$$a_3(x_3, y_3, z, \Delta\omega) = \frac{i}{\lambda z}\int a_2(x_2, y_2, \Delta\omega)\exp\left\{\frac{ik}{2z}\left[(x_3 - x_2)^2 + (y_3 - y_2)^2\right]\right\}dx_2 dy_2.$$ (A.25)

Inserting Eqs.(A.16) and (A.17) yields

$$a_3(x_3, z, \Delta\omega) = c_3 a_{in}(\Delta\omega)\exp\left(i\frac{kx_3^2}{2z}\right)\exp\left[-i\frac{kq(d_0)}{2zq(d_0 - \eta^2 z)}(x_3 - \kappa\Delta\omega z)^2\right],$$ (A.26)

where c_3 includes the minor position dependence.

Eq.(A.26) explicitly presents important characteristics. The spectral lateral walk-off after passing through the dispersor is expressed in the parenthesis. We consider a

well-collimated beam propagation used in most practical experiments. This condition is that the beam propagating distance is much smaller than the confocal parameter, i.e. $|d_0| \ll \pi\sigma^2/\lambda$ and $|d_0 - \eta^2 z| \ll \pi\sigma^2/\lambda$. The coefficient $q(d_0)/q(d_0 - \eta^2 z)$ is then

$$q(d_0)/q(d_0 - \eta^2 z) = 1 - 2i\eta^2 z/k\sigma^2.$$ (A.27)

In this case Eq.(A.26) is rewritten as

$$a_3(x_3, z, \Delta\omega) = c_3 a_{in}(\Delta\omega)\exp\left[-\frac{\eta^2}{\sigma^2}(x_3 - \kappa\Delta\omega z)^2\right]\exp\left[-i\frac{k\kappa^2 z}{2}(\Delta\omega)^2 + ik\kappa x_3 \Delta\omega\right].$$ (A.28)

The first exponential describes the effective spectral filtering at each point by the lateral walk-off. The phase with the characteristic quadratic term

$$\phi(\omega) = -\frac{k\kappa^2 z}{2}(\Delta\omega)^2 = -\frac{k\kappa^2 z}{2}(\omega - \omega_0)^2$$ (A.29)

is derived. The group-delay dispersion (GDD) is then given by

$$\frac{\partial^2\phi}{\partial\omega^2} = -k\kappa^2 z = -\frac{\lambda^3}{2\pi c^2}\left(\frac{\partial\phi}{\partial\lambda}\right)^2 z.$$ (A.30)

The sign of the GDD is always negative, presenting the characteristic feature of a GDD by an angular dispersion [92]. The GDD is proportional to the propagation distance z from the dispersor. However, if the beam divergence is non-negligible, i.e., the plane-wave approximation given in Eq.(A.27) is invalid, the GDD contains the terms with the complicated dependence on z. The inclusion of the higher-order deflection of the angular dispersion in Eq.(A.10) can describe the higher-order dispersion such as a third-order dispersion.

The temporal envelope is given by

$$A_3(x_3, z, t) = \int a_3(x_3, z, \Delta\omega)e^{-i\Delta\omega t}d\Delta\omega$$
$$= \exp\left[-\frac{(t - t_0)^2}{\tau^2}\right]\exp\left[iC(t - t_0)^2\right]\exp\left[-i\varepsilon(t - t_0)\right]\exp\left(-\frac{\eta^2 x_3^2}{(1 + u)\sigma^2}\right)f(x, z),$$ (A.31)

where

$$u = \left(\frac{2\eta\kappa z}{\sigma\tau_0}\right)^2, \tag{A.32a}$$

$$\tau^2 = \left[(1+u) + \frac{4k^2\kappa^4 z^2}{\tau_0^4(1+u)}\right]\tau_0^2, \tag{A.32b}$$

$$t_0 = \frac{k\kappa x_3}{1+u}, \tag{A.32c}$$

$$C = \frac{2k\kappa^2 z}{(1+u)\tau_0^2\tau^2}, \tag{A.32d}$$

$$\varepsilon = \frac{u}{1+u}\frac{x_3}{\kappa z}, \tag{A.32e}$$

and $f(x, z)$ is a minor function representing the change of the curvature. The picture in the time domain is obvious. The pulse-front tilting is described by t_0 in Eq.(A.32c) and we obtain the tilt angle as

$$\tan\gamma(z) = \frac{ct_0}{x_3} = \frac{ck\kappa}{1+u} = \frac{\tan\gamma_0}{1+u}, \tag{A.33}$$

where γ_0 is the tilt angle at the exit of the dispersor given by Eq.(A.23). Thus the tilt angle is decreased as u increases, i.e., as the pulse propagates away from the dispersor. For example, a 10° tilt angle is decreased to 5° at $u = 1$.
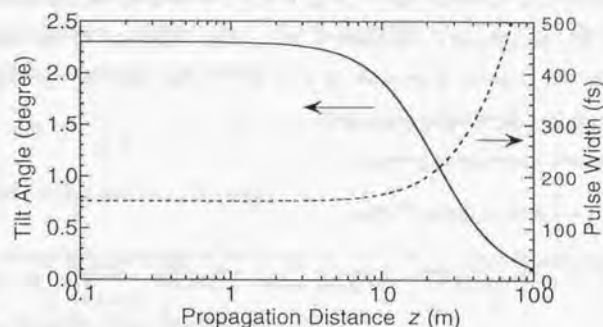

Fig. A.3. Propagation property of a tilted pulse on the present experimental condition. The tilt angle (solid curve) and pulse width (dashed curve) are shown. The initial values at the prism ($z = 0$) are 2.3° and 150 fs, respectively.

As indicated in Eq.(A.32b), the pulse width is broadened by the propagation because of the effective spectral narrowing due to the lateral walk-off and of the GDD by the angular dispersion. C represents the resultant positive chirp, whereas ε gives the position dependence of the spectral component along the cross section.

In the pulse-front matching geometry in the present work a 45° fused-silica prism is used with a 49° incidence angle. In this case from Eqs.(A.8) and (A.9) the tilt angle generated at the prism is 2.3°. From Eqs.(A.11) and (A.12) $\eta = -0794$ and $\kappa = 8.3\times10^{-3}$ fs. On the experimental condition of $\sigma \sim 2$ mm and $\tau_0 = 150$ fs, $u = (0.044z)^2$ resulting in $z = 23$ m for $u = 1$. The changes of the tilt angle and pulse width are shown in Fig. A.3, clearly indicating the changes are small enough even at $z = 1$ m. However, if the tilt angle is larger and the pulse width is shorter, the distortion becomes non-negligible just after the dispersor [85].

Magnification of Tilt Angle

The tilt angle can be changed by an imaging optics. If the dispersor is placed on the objective plane of a telescope with a longitudinal magnification factor M, the temporal amplitude on the image plane is given strictly by

$$A_4(x_4, y_4, t) = c_4 A_3(-Mx_4, -My_4, t)$$
$$= c_1 c_4 \exp\left(-i\frac{k\eta^2 x_4^2 + y_4^2}{2q(d_0)/M^2}\right)\exp\left[-\left(\frac{Mk\kappa x_4 + t}{\tau_0}\right)^2\right] \tag{A.34}$$

The beam diameter is then reduced by the lateral magnification factor M^{-1}, whereas the transferred tilt angle γ' is given by the relation

$$\tan\gamma' = -Mck\kappa = -M\tan\gamma. \tag{A.35}$$

Thus the tilt angle is magnified with the direction reversed.

Refraction at Boundary

The tilt angle is also changed when the tilted pulse is injected to a medium (Fig. A.4). Because the distortion of the tilted pulse by propagation is in most cases small enough as mentioned above, we consider the amplitude of the incident beam as $a_3(x_3, z = 0, \Delta\omega)$ given in Eq.(A.28). The relation with the amplitude of the refracted beam $a_5(x_5, \Delta\omega)$ in the medium (refractive index n) can be derived in the same way as in
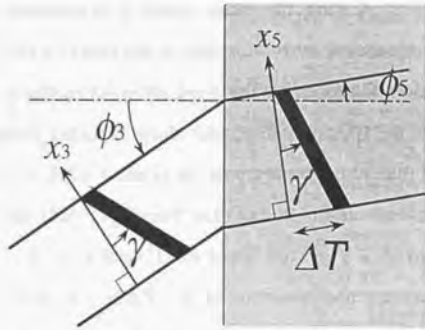
Fig. A.4. Refraction of a tilted pulse in a medium.

Eqs.(A.13)–(A.16) with slight differences. From the Snell's law $\sin\phi_3 = n\sin\phi_5$, we obtain the coefficients in Eq.(A.10) as

$$\eta' = \frac{\partial\phi_5}{\partial\phi_3} = \frac{\cos\phi_3}{n\cos\phi_5}, \tag{A.36}$$

$$\kappa' = \frac{\partial\phi_5}{\partial\omega} = -\frac{\lambda^2}{2\pi c}\frac{\partial\phi_5}{\partial\lambda} = \frac{\lambda^2}{2\pi c}\frac{1}{n}\frac{dn}{d\lambda}\tan\phi_5. \tag{A.37}$$

The phases of the external and internal angle changes $\Delta\phi_3$ and $\Delta\phi_5$ are equalized as

$$k\Delta\phi_3 x_3 = k\Delta\phi_5 nx_5. \tag{A.38}$$

It should be noted that the optical path is used for the refracted beam. Substituting Eq.(A.36) yields

$$x_3 = \frac{\partial\phi_5}{\partial\phi_3}nx_5 = \eta' nx_5. \tag{A.39}$$

The amplitude of the refracted beam is then obtained in analogy with Eq.(A.16):

$$\begin{aligned} a_5(x_5, \Delta\omega) &= c_5 a_3(x_3, z=0, \Delta\omega)\exp(ik\kappa'\Delta\omega nx_5) \\ &= c_5 c_3 a_3(\eta' nx_5, z=0, \Delta\omega)\exp(ik\kappa'\Delta\omega nx_5) \\ &= c_5 c_3 a_m(\Delta\omega)\exp\left[-\left(\frac{\eta\eta' nx_5}{\sigma}\right)^2\right]\exp\left[iknx_5(\kappa\eta'+\kappa')\Delta\omega\right], \end{aligned} \tag{A.40}$$

where Eq.(A.28) is substituted. The temporal amplitude is obtained similarly by the

procedures from Eqs.(A.19) to (A.22) as

$$A_5(x_5, y, t) = c_6 \exp\left(-i\frac{k(\eta\eta' nx_5)^2 + y^2}{2q(d_0)}\right)\exp\left[-\left(\frac{knx_5(\kappa\eta'+\kappa')-t}{\tau_0}\right)^2\right], \tag{A.41}$$

which represents the delay of the peak intensity $\Delta T = kn(\kappa\eta'+\kappa')x_5$. Using the group velocity v_g in the medium the transferred tilt angle γ' is given by

$$\begin{aligned} \tan\gamma' &= \frac{v_g\Delta T}{x_5} = v_g kn(\kappa\eta'+\kappa') = ck\kappa n\left(\eta'+\frac{\kappa'}{\kappa}\right)\frac{v_g}{c} \\ &= r\tan\gamma, \end{aligned} \tag{A.42}$$

with

$$r = n\left(\eta'+\frac{\kappa'}{\kappa}\right)\frac{v_g}{c} = \frac{\cos\phi_3}{\cos\phi_5}\left(1+\lambda\frac{dn}{d\lambda}\frac{\sin\phi_5}{\cos\phi_3\tan\gamma}\right)\frac{v_g}{c}, \tag{A.43}$$

where Eqs.(A.23), (A.36) and (A.37) are used. Considering $\lambda\,dn/d\lambda = 0.02-0.2$ in typical media, we obtain a simple formula

$$\tan\gamma' = \frac{v_g}{c}\tan\gamma, \tag{A.44}$$

in the case of a small incident angle. Note that the change of a tilt angle by refraction is described not by refractive indices but by group velocities. This formula can be also derived straightforwardly from the geometrical relation in Fig. A.4.

Appendix B. Ray-tracing Formalism of Group Delay in a Prism Pair and Grating Pair

For the design of a pulse compressor, conventionally used is elimination of each Taylor-expanded terms of the phase such as the group-delay dispersion (GDD) and third-order dispersion (TOD) at a center frequency. However, if the phase has a complicated frequency dependence, this approach seems inappropriate. This is especially when the compressor is composed of chirped mirrors, which sometimes have non-negligible oscillating structures. As discussed in Section 3.2.2, a global cancellation of the group delay (GD) over the spectrum is useful for the compressor design in a sub-10-fs regime. This approach has been applied in previous works [20,21, 23,24,93] and is used thoroughly in the present work as is in Chapter 2.

The GD as a function of wavelength is obtained by a ray-tracing analysis, which includes the wavelength-dependent refraction, diffraction, and refractive index. Differentiating the accumulated phase along the optical path gives the GD. Here the description is based on geometrical optics, equivalent to a plane-wave approximation. If the beam divergence is non-negligible, the wave experiences a phase shift with more complicated dependence on the propagation distance as indicated in Appendix A. In most practical applications including the present work, the compressor is introduced for a well-collimated beam with the propagation distance much shorter than the confocal parameter. In this case the GD of a prism pair or a grating pair is given as an analytical form, as presented below for the convenience of rapid applications.

Basic Description

Martinez et al. derived the GD originating from a refraction in a general form by use of geometrical optics [92]. Consider the plane-wave propagation refracted by a slab of refractive index n (Fig. B.1). The phase shift suffered by the wave propagating from A to B is

$$\phi(\lambda) = k \cdot \overrightarrow{AB} = kl\cos\theta = \frac{2\pi}{\lambda}nl\cos\theta, \tag{B.1}$$
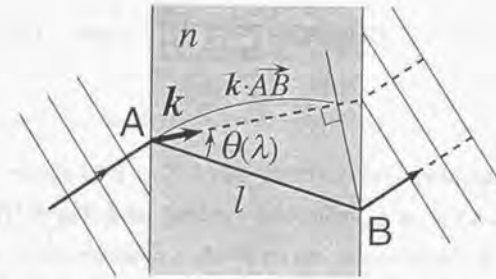
Fig. B.1. Wavelength-dependent phase shift by refraction in a slab. The thin lines represent the wave fronts.

where k is the wavevector in the slab, l is the angle which k makes with AB, and l is the distance of AB. The optical path length is

$$P(\lambda) = \frac{c}{\omega}\phi(\lambda) = nl\cos\theta. \tag{B.2}$$

Then the GD and GDD are given by

$$T(\lambda) = \frac{d\phi}{d\omega} = \frac{1}{c}\left(P(\lambda) - \lambda\frac{dP}{d\lambda}\right) = \frac{l}{c}\left(n\cos\theta - \lambda\frac{dn}{d\lambda}\cos\theta + n\lambda\frac{d\theta}{d\lambda}\sin\theta\right), \tag{B.3}$$

$$
\begin{aligned}
GDD(\lambda) &= \frac{d^2\phi}{d\omega^2} = \frac{\lambda^3}{2\pi c^2}\frac{d^2P}{d\lambda^2} \\
&= \frac{\lambda^3}{2\pi c^2}\left[\frac{d^2n}{d\lambda^2}\cos\theta - 2\sin\theta\frac{dn}{d\lambda}\frac{d\theta}{d\lambda} - n\cos\theta\left(\frac{d\theta}{d\lambda}\right)^2 - n\sin\theta\frac{d^2\theta}{d\lambda^2}\right]l.
\end{aligned} \tag{B.4}
$$

When AB is parallel to k at the center wavelength, $\theta = 0$, yielding

$$T(\lambda_0) = \frac{l}{c}\left[n_0 - \lambda_0\left(\frac{dn}{d\lambda}\right)_0\right] = \frac{l}{v_g}, \tag{B.5}$$

$$GDD(\lambda_0) = \frac{\lambda_0^3}{2\pi c^2}\left[\left(\frac{d^2n}{d\lambda^2}\right)_0 - n_0\left(\frac{d\theta}{d\lambda}\right)_0^2\right]l, \tag{B.6}$$

where 0 denotes the center value and v_g is the group velocity. Eq.(B.6) clearly represents the property of the GDD by refraction. The first term expresses the material dispersion and is positive in a normal dispersion. The second term originates from the refraction and always negative irrespective of the sign of $d\theta/d\lambda$. If the slab is vacuum

$(n = 1)$, Eq.(B.6) reduces to $GDD(\lambda) = -\dfrac{\lambda^3}{2\pi c^2}\left(\dfrac{d\theta}{d\lambda}\right)^2 l$, which is equal to Eq.(A.30)

in Appendix A.

Prism Pair

The optical path length $P(\lambda)$ given by Eq.(B.2) is valid also in the case of an arbitrary prism pair arranged in anti-parallel with each other (Fig. B.2) [91,92]. In this case $n = 1$ and $\theta \neq 0$. Considering the round-trip propagation for elimination of the angular dispersion, the GD given by Eq.(B.3) reduces to

$$T(\lambda) = \frac{2l}{c}\left(\cos\theta + \lambda\frac{d\theta}{d\lambda}\sin\theta\right).\tag{B.7}$$

For the sake of convenience, let us express Eq.(B.7) by a slant length l and an intraprism path length (IPL) x which is defined as the path length in the prism at the center wavelength. Defining Ψ as the angle which AB makes with the normal vector of the exit surface of the first prism yields

$$\theta(\lambda) = \Psi - \phi_2(\lambda).\tag{B.8}$$

Here angles ϕ_1, $\phi_1{}'$, ϕ_2, $\phi_2{}'$ are defined as in Fig. A.1. Then we obtain

$$\frac{d\theta}{d\lambda} = -\frac{d\phi_2}{d\lambda} = -\frac{\sin\alpha_{apex}}{\cos\phi_1{}'(\lambda)\cos\phi_2(\lambda)}\frac{dn}{d\lambda}.\tag{B.9}$$
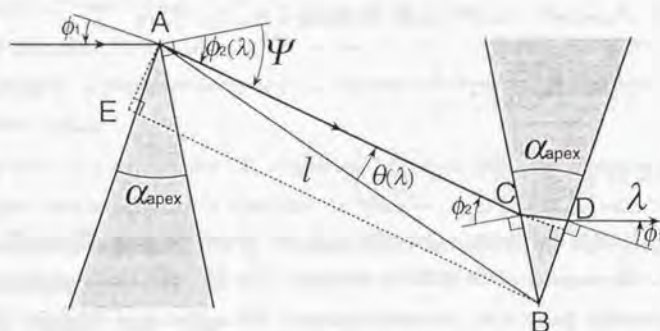
By geometry (see Fig. B.2),

Fig. B.2. Geometry of a prism pair. The incident angle ϕ_i is constant for all λ. For the more details of the calculation of $P(\lambda)$, see ref.[91].

$$BC = AE/\cos\phi_2 = l\sin\theta/\cos\phi_2,\tag{B.10}$$

$$BC\sin\alpha_{apex} = CD\cos\phi_1{}'.\tag{B.11}$$

The IPL is the distance of CD at the center wavelength. Then from Eqs.(B.10) and (B.11), we obtain

$$x = l\frac{\sin\theta_0\sin\alpha_{apex}}{\cos\phi_{10}{}'\cos\phi_{20}}.\tag{B.12}$$

By using Eq.(B.8) at the center wavelength,

$$\theta_0 = \Psi - \phi_{20} = \sin^{-1}\left(\frac{x}{l}\frac{\cos\phi_{10}{}'\cos\phi_{20}}{\sin\alpha_{apex}}\right),\tag{B.13}$$

then θ is expressed as

$$\theta(\lambda) = \sin^{-1}\left(\frac{x}{l}\frac{\cos\phi_{10}{}'\cos\phi_{20}}{\sin\alpha_{apex}}\right) + \phi_{20} - \phi_2(\lambda).\tag{B.14}$$

By substituting Eqs.(B.9) and (B.14) into Eq.(B.7), we obtain the exact form of the wavelength-dependent GD with parameters of l and x. Angles $\phi_1{}'(\lambda)$, $\phi_2(\lambda)$, $\phi_{10}{}'$, and ϕ_{20} are obtained from Eqs.(A.4)–(A.6) for an arbitrary incident angle ϕ_i. In the case of the minimum deviation used thoroughly in the present work, $\phi_1 = \phi_{20}$ and $\phi_{10}{}' = \phi_{20}{}' = \alpha_{apex}/2$ [207].

Grating Pair

In the case of a grating pair (see Fig. B.3), Eq.(B.2) is invalid. Because of the property of the diffraction, there is each phase delay along the direction CB on the surface of the second grating. The amount is $2m\pi$ per each step of ruling for the m-th order diffraction [90]. The phase shift is then given by

$$\phi(\lambda) = \frac{\omega P(\lambda)}{c} - 2m\pi\frac{BC}{a} = \frac{\omega P(\lambda)}{c} - 2m\pi bG\tan(\gamma - \theta),\tag{B.15}$$

where a is the grating constant, $b = 1/a$ is the grove density, γ is the incident angle, and G is the grating separation. The optical path length along PABQ is [90]

$$P(\lambda) = \frac{G}{\cos(\gamma - \theta)}(1 + \cos\theta).\tag{B.16}$$
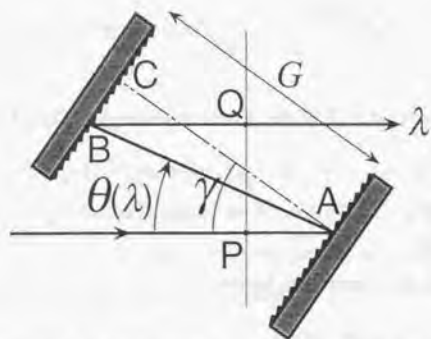
Fig. B.3. Geometry of a grating pair. For the more details, see ref. [90].

The grating equation is

$$\sin(\gamma - \theta) + \sin \gamma = mb\lambda, \qquad (B.17)$$

then

$$\frac{d\theta}{d\lambda} = -\frac{mb}{\cos(\gamma - \theta)}. \qquad (B.18)$$

By substituting Eq.(B.16) into Eq.(B.15) and using Eq.(B.17), we obtain the well-known formula

$$T(\lambda) = \frac{d\phi}{d\omega} = \frac{P(\lambda)}{c}. \qquad (B.19)$$

This simple relation between the GD and $P(\lambda)$ was also derived from a Fermat's principle for a grating [208]. The GD and GDD by a round-trip propagation are

$$T(\lambda) = \frac{2G(1 + \cos\theta(\lambda))}{c \cos(\gamma - \theta(\lambda))}, \qquad (B.20)$$

$$GDD(\lambda) = \frac{d^2\phi}{d\omega^2} = \frac{1}{c}\frac{dP}{d\omega} = -\frac{\lambda^3 m^2 b^2 G}{\pi c^2 \cos^3(\gamma - \theta)} = -\frac{\lambda^3}{2\pi c^2}\left(\frac{d\theta}{d\lambda}\right)^2 \frac{2G}{\cos(\gamma - \theta)}. \qquad (B.21)$$

The GD as a function of λ can then be calculated by use of Eq.(B.17). The characteristic negative GDD by refraction given by Eq.(B.6) is obtained again with $n = 1$ and $l = 2G/\cos(\gamma - \theta)$.

Appendix C. Geometrical Smearing of Two-beam Crossing

In the interaction of femtosecond pulses with a finite noncollinear angle there lies a fundamental problem of a pulse-front mismatch. The mismatch causes the pulse-width broadening because of the time-space coupling over the beam cross section. In Chapter 3 we have introduced a tilted-pump geometry to a noncollinear optical parametric amplification and the pulse-front matching between the pump and signal is attained. The non-tilted signal amplification enables the compression to the transform-limited pulse. In the up-conversion (autocorrelation, cross-correlation, etc.) or the similar pump-probe-like interaction, the pulse-front matching is also possible by introducing prisms [209] or gratings [210] in either or both of paths of two beams. However, it is rather complicated to control the pulse-front tilt before the crystal or the sample. In addition, especially in the case of a sub-10-fs pulse interaction, the pulse-width broadening as well as the nonlinear tilt caused by the insertion of dispersive elements would become significant (see Section 3.1 and Appendix A). Here the broadening effect of a pulse without any tilt-control is estimated in the case of an autocorrelation. This type of smearing of the delay is well known and even utilized for single-shot-type measurements [211,212,213]. Similar results are also introduced in ref. [95,96] for an frequency-resolved optical gating.

The schematic of a two-beam interaction is shown in Fig. C.1. The pulse 1 at the point A precedes that at O, then the electric field is written as

$$E_1(\mathbf{r}, t) = E_{envelope}\left(t + \frac{x}{v_g}\sin\frac{\theta}{2} - \frac{z}{v_g}\cos\frac{\theta}{2}\right)E_{profile}\left(\sqrt{\left(x\cos\frac{\theta}{2}\right)^2 + y^2}\right)$$
$$\times\left[\exp\left(i\omega\left(t + \frac{x}{v}\sin\frac{\theta}{2} - kz\cos\frac{\theta}{2}\right)\right) + c.c.\right], \qquad (C.1)$$

where $E_{envelope}$ and $E_{profile}$ are the envelope and spatial profile function, respectively. v, v_g, ω, and k are the phase velocity, group velocity, angular frequency, and wavevector, respectively. For simplicity, the pulse shape is assumed to be Gaussian with a

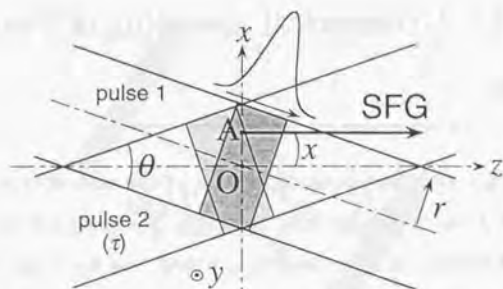## Appendix C. Geometrical Smearing of Two-beam Crossing

Fig. C.1. Schematic representation of the geometrical smearing due to a noncollinear interaction. SFG, sum-frequency generation.

Gaussian spatial profile, i.e.,

$$E_{\text{envelope}}(t) \propto \exp\left(-\frac{t^2}{T^2}\right), \quad E_{\text{profile}}(r) \propto \exp\left(-4\frac{r^2}{d^2}\right),$$ (C.2)

where $T \equiv \tau_p / \sqrt{2\ln 2}$. τ_p and d are the pulse width (FWHM) and beam diameter ($1/e^2$), respectively. The pulse 2 delayed by τ from the pulse 1 has the reversed relation along the cross section, so that the power of the sum frequency emitted at r is

$$P_{\text{SFG}}(\mathbf{r}, t; \tau) \propto |P^{\omega+\omega}|^2 \propto |E_1 E_2|^2$$

$$= E_{\text{envelope}}^2\left(t + \frac{x}{v_g}\sin\frac{\theta}{2}\right) E_{\text{envelope}}^2\left(t - \tau - \frac{x}{v_g}\sin\frac{\theta}{2}\right) E_{\text{profile}}^4\left(\sqrt{\left(x\cos\frac{\theta}{2}\right)^2 + y^2}\right),$$ (C.3)

where $P^{\omega+\omega}$ is the induced second-order nonlinear polarization. The reduced time coordinate $t \leftarrow t - (z/v_g)\cos(\theta/2)$ is used. The correlation intensity $I_{AC}(\tau)$ is given as the integrated emitted energy. Substituting Eq.(C.2) into Eq.(C.3), we obtain

$$I_{AC}(\tau) \propto \int dx \int dy \int dt |P_{\text{SFG}}(\mathbf{r}, t; \tau)|^2 \propto \int dx \int dy \int dt$$

$$\times \exp\left[-\frac{2}{T^2}\left(t + \frac{x}{v_g}\sin\frac{\theta}{2}\right)^2 - \frac{2}{T^2}\left(t - \tau - \frac{x}{v_g}\sin\frac{\theta}{2}\right)^2\right] \exp\left[-16\left(\frac{\left(x\cos\theta/2\right)^2 + y^2}{d^2}\right)\right]$$

$$= \text{const.} \times \exp\left(-\frac{\tau^2}{\alpha^2 T^2}\right),$$ (C.4)

where

$$\alpha^2 \equiv 1 + \left(\frac{d}{2v_g T}\tan\frac{\theta}{2}\right)^2.$$ (C.5)

Because the autocorrelation function of $E_{\text{envelope}}(t)$ is equal to itself, $\exp(-\tau^2/T^2)$, T is artificially increased to αT. The measured pulse width τ_p^{meas} is then given by

$$\tau_p^{\text{meas}} = \sqrt{2\ln 2}\,\alpha T = \sqrt{\tau_p^2 + \delta\tau^2},$$ (C.6)

where

$$\delta\tau \equiv \sqrt{\frac{\ln 2}{2}}\frac{d}{v_g}\tan\frac{\theta}{2}.$$ (C.7)

Note that the velocity is a group velocity in the medium, which differs from ref. [95,96] in addition to a numerical coefficient. Assuming that $v_g \approx v = c/n$ and θ is small, Eq.(C.7) reduces to

$$\delta\tau \approx \sqrt{\frac{\ln 2}{8}}\frac{d \cdot \theta_{\text{ext}}}{c},$$ (C.8)

where θ_{ext} is the external noncollinear angle.

In the case of a 5-fs pulse, this geometrical smearing is a severe problem. For $\theta_{\text{ext}} = 3°$ and $d = 100$ μm, $\delta\tau$ is as large as 5.1 fs and the measured pulse width will then be broadened to 7.2 fs. Therefore the noncollinear angle and beam diameter should be as small as possible to maintain the highest time resolution. Examples on various practical experimental conditions are listed in Table C.1.

τ_p	d	θ_{ext}	τ_p^{meas}	τ_p	d	θ_{ext}	τ_p^{meas}
5 fs	100 μm	1.5°	5.6 fs	100 fs	100 μm	1.5°	100 fs
		3°	7.2 fs			3°	100 fs
		10°	17.9 fs			10°	101 fs
10 fs	100 μm	1.5°	10.3 fs		1 mm	1.5°	103 fs
		3°	11.2 fs			3°	112 fs
		10°	19.8 fs			10°	198 fs

Table C.1. Geometrical smearing on various experimental conditions.

Acknowledgements

The present research has been performed under the continuing guidance of Prof. T. Kobayashi. The author would like to gratefully acknowledge him for his support and for providing me many opportunities to publicize the present works in scientific journals.

The author would very much thank Dr. K. Misawa for a number of helpful discussions and suggestions during the course of this work and for providing the software for data acquisition of a transient transmission change. I would like to thank Messrs. A. Ueki and S. Otsuka for their technical supports and kind advises in manufacturing a number of components of the system. The author would also like to thank Mr. F. Shimokoshi for taking photographs of the system for the presentations in newspapers.

The author would like to thank all the colleagues in our group for their kindness and encouragement of the research, especially Mr. I. Sakane, who produced a program for a Fourier analysis of the autocorrelation traces and gave me useful advises in constructing other programs. I would also like to thank Dr. S. Takeuchi, who kindly provided the original program and diagrams of electric circuits for data acquisition. The useful suggestions and contributions from Drs. T. Sekikawa, Z. Lei, Q. Zheng, S. Hughes, and A. Sugita and Messrs. S. Morita, H. Kanou, and A. Furuta are also especially appreciated.

The author would like to express special thanks to Mr. M. Takasaka and his colleagues for providing us the chirped mirrors for the sub-5-fs pulse generation. I would also like to thank Prof. H. Nakanishi and Dr. H. Matsuzawa for providing us the polydiacetylene film samples. Their supports in both co-working programs are invaluable.

The author would like to thank Prof. H. Okamoto for measuring the Raman spectra of the polydiacetylene sample. I also gratefully acknowledge the valuable advises from Profs. Y. Toyozawa, M. Yoshizawa, and H. Hashimoto about the self-trapping processes in polydiacetylenes.

The author would appreciate the kind encouragement given by a number of researchers in the fields related to this work, especially by Profs. S. Watanabe, N. Sarukura, S. De Silvestri, and A. Piskarskas and by Drs. K. Torizuka, R. Szipöcs, M. K. Reed, V. V. Yakovlev, and J. Itatani. I would especially acknowledge Dr. Szipöcs for fabrication of the chirped mirrors in the early days.

The author would very much thank Profs. S. Yamamoto, K. Tsubono, S. Watanabe, H. Kuroda, and K. Ueda for refereeing and improving the present thesis kindly.

Finally, the author would express special thanks to my parents and my fiancée, Haruno for their continuous help and support in continuing the present research. This thesis is dedicated to my only brother, Takashi.

Publications and Presentations by the Author

Publications in Scientific Journals

1. H. W. Mao, A. Shirakawa, and T. Kobayashi, "Angular Tuning of Femtosecond Synchronously Pumped KTP IR OPO", Chinese Journal of Lasers 22, 902–907 (1995).

2. Akira Shirakawa and Takayoshi Kobayashi, "Efficient Femtosecond Optical Parametric Oscillator Tunable in a Blue-Orange Region", The Review of Laser Engineering 23, 922–927 (1995). [in Japanese]

3. A. Shirakawa, H. W. Mao, and T. Kobayashi, "Highly efficient generation of blue-orange femtosecond pulses from intracavity-frequency-mixed optical parametric oscillator", Optics Communications 123, 121–128 (1996).

4. Lei Zhang, Akira Shirakawa, Shigeki Morita, and Takayoshi Kobayashi, "Nonllinear Phase Shift and Detuning by Second- and Third-Order Nonlinearlities", Japanese Journal of Applied Physics 36, L1294–1296 (1997).

5. Akira Shirakawa and Takayoshi Kobayashi, "Noncollinearly phase-matched femtosecond optical parametric amplification with a 2000-cm^{-1} bandwidth", Applied Physics Letters 72, 147–149 (1998).

6. Akira Shirakawa and Takayoshi Kobayashi, "Noncollinear Phase- and Group-Velocity Matching of Optical Parametric Amplifier for Ultrashort Pulse Generation", IEICE Transactions on Electronics E81-C, 246–253 (1998).

7. Akira Shirakawa, Isao Sakane, and Takayoshi Kobayashi, "Pulse-front-matched optical parametric amplification for sub-10-fs pulse generation tunable in the visible and near-infrared", Optics Letters, 23, 1292–1294 (1998).

8. A. Shirakawa, I. Sakane, M. Takasaka, and T. Kobayashi, "Sub-5-fs visible pulse generation by pulse-front-matched noncollinear optical parametric amplification", Applied Physics Letters, to be published in the issue of 19 April 1999.

Publications in Bulletins and Books

1. A. Shirakawa, H. W. Mao, and T. Kobayashi, "Highly-efficient generation of visible femtosecond pulses from optical parametric oscillator", Technical Report of IEICE, LQE94, 35–40 (1994). [in Japanese]

2. Akira Shirakawa, Isao Sakane, and Takayoshi Kobayashi, "Broadband Optical Parametric Amplification", Oyo Buturi 67, 1070–1071 (1998). [in Japanese]

3. Akira Shirakawa, Isao Sakane, and Takayoshi Kobayashi, "Sub-5-fs Pulse Generation by Pulse-front-matched Optical Parametric Amplification", in Ultrafast Phenomena XI, T. Elsaesser, J. G. Fujimoto, D. A. Wiersma, and W. Zinth eds. (Springer-Verlag, Berlin, 1998), p.54–56.

Presentations in International Conferences and Workshops

1. A. Shirakawa, H. W. Mao, and T. Kobayashi, "High-power, high-repetition-rate femtosecond light source tunable in a green-orange region", International Workshop on Femtosecond Technology, Tsukuba, February 1995.

2. A. Shirakawa, H. W. Mao, and T. Kobayashi, "High-power Green femtosecond pulses", Conference on Lasers and Electro-Optics/Pacific Rim '95, Chiba, July 1995.

3. A. Shirakawa, S. Morita, K. Misawa, and T. Kobayashi, "Broadband Femtosecond Optical Parametric Amplification in a Non-collinear Phase-Matching Geometry", Fourth International Workshop on Femtosecond Technology, Tsukuba, February 1997.

4. Akira Shirakawa, Shigeki Morita, Kazuhiko Misawa, and Takayoshi Kobayashi, "100-nm Bandwidth Noncollinearly Phase-matched Femtosecond Optical Parametric Amplifier", Conference on Lasers and Electro-Optics/Pacific Rim '97, Chiba, July 1997.

5. Akira Shirakawa and Takayoshi Kobayashi, "Broadband 18-fs Optical Parametric Amplifier by Noncollinear Phase-matching", Ultrafast Optics 1997, Monterey, August 1997.

6. Akira Shirakawa and Takayoshi Kobayashi, "Sub-10-fs Pulse Generation from a Noncollinear Optical Parametric Amplifier," Fifth International Workshop on Femtosecond Technology, Tsukuba, February 1998.

7. A. Shirakawa, I. Sakane, and T. Kobayashi, "Pulse-front-matched Optical Parametric Amplification for Pulse Generation Tunable in the Visible and Near-infrared Reaching to 6.5fs", 1998 Conference on Lasers and Electro-Optics, Postdeadline Paper, San Francisco, May 1998.

8. A. Shirakawa, I. Sakane, and T. Kobayashi, "Sub-5-fs Pulse Generation by Pulse-front-matched Optical Parametric Amplification", XIth International Conference on Ultrafast Phenomena, Postdeadline Paper, Garmisch-Partenkirchen, July 1998.

9. A. Shirakawa, I. Sakane, M. Takasaka, and T. Kobayashi, "Sub-5-fs Visible Pulse

Generation by Pulse-front-matched Optical Parametric Amplification", 1999 Conference on Lasers and Electro-Optics, Baltimore, May 1999 (invited talk).

10. T. Kobayashi, A. Shirakawa, H. Matsuzawa, and H. Nakanishi, "Sub-5-fs Real-time Spectroscopy of Coherent Geometrical Relaxation Processes in Polydiacetylenes", 1999 Quantum Electronics and Laser Science Conference, Baltimore, May 1999.

11. Akira Shirakawa, "Novel Sub-5-fs Pulse Generation by Noncollinear Optical Parametric Amplification," Sixth International Workshop on Femtosecond Technology, Tsukuba, July 1999 (invited talk).

12. Akira Shirakawa, "Sub-9-fs pulse generation tunable in visible (550–700nm) and near-IR (0.9–1.3μm) by noncollinear phase matching and pulse-front matching", Conference on Lasers and Electro-Optics/Pacific Rim '99, Seoul, August 1999 (invited talk).

Presentations in Domestic Meetings and Workshops [in Japanese]

1. A. Shirakawa, H. W. Mao, and T. Kobayashi, "Femtosecond Optical Parametric Oscillator tunable in the Visible", 1994 Sectional Meeting of the Physical Society of Japan, Shizuoka, September 1994.

2. A. Shirakawa, H. W. Mao, and T. Kobayashi, "High-power Green femtosecond pulses", Workshop of IEICE on Lasers and Quantum Electronics, Sendai, November 1994.

3. A. Shirakawa and T. Kobayashi, "Review of Femtosecond Laser Spectroscopy", Fifth Workshop on Technology and Application of Linac, Tokai-mura, March 1996.

4. A. Shirakawa, S. Morita, K. Misawa, and T. Kobayashi, "Femtosecond Optical Parametric Amplifier under a Noncollinear Phase-matching Condition", 52nd Annual Meeting of the Physical Society of Japan, Nagoya, March 1997.

5. A. Shirakawa, S. Morita, K. Misawa, and T. Kobayashi, "Spectral Broadening in an Optical Parametric Amplification by a Noncollinear Phase Matching", 44th Spring Meeting of the Japan Society of Applied Physics and Related Societies, Funabashi, March 1997.

6. A. Shirakawa, A. Furuta, and T. Kobayashi, "Properties of the Broadband Amplification of a Femtosecond Optical Parametric Interaction under a Group-Velocity Matching", 1997 Sectional Meeting of the Physical Society of Japan, Kobe, October 1997.

7. A. Shirakawa and T. Kobayashi, "Tunable Sub-10-fs Pulse Generation by

Broadband Optical Parametric Amplification," 45th Spring Meeting of the Japan Society of Applied Physics and Related Societies, Hachioji, March 1998.

8. A. Shirakawa, I. Sakane, and T. Kobayashi, "Development of a Tunable Sub-9-fs Optical Pulse Source both in the Visible and Near-infrared", 1998 Sectional Meeting of the Physical Society of Japan, Naha, September 1998.

9. A. Shirakawa, I. Sakane, M. Takasaka, and T. Kobayashi, "Sub-5-fs Pulse Generation by Noncollinear Optical Parametric Amplification", 46th Spring Meeting of the Japan Society of Applied Physics and Related Societies, Noda, March 1999.

10. T. Kobayashi, A. Shirakawa, H. Matsuzawa, and H. Nakanishi, "Sub-5-fs Real-time Spectroscopy of Coherent Geometrical Relaxation in Polydiacetylenes", 46th Spring Meeting of the Japan Society of Applied Physics and Related Societies, Noda, March 1999.

References

[1] D. E. Spence, P. N. Kean, and W. Sibbett, Opt. Lett. **16**, 42 (1991).

[2] J. Squier, F. Salin, G. Mourou, and D. Harter, Opt. Lett. **16**, 324 (1991).

[3] P. E. Powers, R. J. Ellingson, W. S. Pelouch, and C. L. Tang, J. Opt. Soc. Am. B **10**, 2162 (1993).

[4] V. Petrov, F. Seifert, O. Kittelmann, J. Ringling, and F. Noack, J. Appl. Phys. **76**, 7704 (1994).

[5] M. K. Reed and M. K. Steiner-Shepard, IEEE J. Quantum Electron. **32**, 1273 (1996).

[6] K. R. Wilson and V. V. Yakovlev, J. Opt. Soc. Am. B **14**, 444 (1997).

[7] K. L. Vodopyanov, and P. G. Schunemann, Opt. Lett. **23**, 1096 (1998).

[8] H. Nishioka, W. Odajima, K. Ueda, and H. Takuma, Opt. Lett. **20**, 2505 (1995).

[9] Ch. Spielmann, N. H. Burnett, S. Sartania, R. Koppitsch, M. Schnürer, C. Kan, M. Lenzner, P. Wobrauschek, and F. Krausz, Science **278**, 661 (1997).

[10] K. Yamakawa, M. Aoyama, S. Matsuoka, T. Kase, Y. Akahane, and H. Takuma, Opt. Lett. **23**, 1468 (1998).

[11] Ch. Spielmann, P. F. Curley, T. Brabec, and F. Krausz, IEEE J. Quantum Electron. **30**, 1100 (1994).

[12] J. Zhou, G. Taft, C. P. Huang, M. M. Murnane, H. C. Kapteyn, and I. P. Christov, Opt. Lett. **19**, 1149 (1994).

[13] L. Xu, Ch. Spielmann, F. Krausz, and R. Szipöcs, Opt. Lett. **21**, 1259 (1996).

[14] I. D. Jung, F. X. Kärtner, N. Matuschek, D. H. Sutter, F. Morier-Genoud, G. Zhang, U. Keller, V. Scheuer, M. Tilsch, and T. Tschudi, Opt. Lett. **22**, 1009 (1997).

[15] I. P. Christov, V. D. Stoev, M. M. Murnane, and H. C. Kapteyn, Opt. Lett. **21**, 1493 (1996).

[16] J. Valdmanis, R. Fork, and J. P. Gordon, Opt. Lett. **10**, 131 (1985).

[17] W. J. Tomlinson, R. H. Stolen, and C. V. Shank, J. Opt. Soc. Am. B **1**, 139 (1984).

[18] R. L. Fork, C. H. Brito Cruz, P. C. Becker, and C. V. Shank, Opt. Lett. **12**, 483 (1987).

[19] M. S. Pshenichnikov, W. P. de Boeji, and D. A. Wiersma, Opt. Lett. **19**, 572 (1994).

[20] A. Baltuska, Z. Wei, M. S. Pshenichnikov, and D. A. Wiersma, Opt. Lett. **22**, 102 (1998).

[21] A. Baltuska, Z. Wei, M. S. Pshenichnikov, D. A. Wiersma, and R. Szipöcs, Appl. Phys. B **65**, 175 (1997).

[22] M. Nisoli, S. De Silvestri, and O. Svelto, Appl. Phys. Lett. **68**, 2793 (1996).

[23] M. Nisoli, S. De Silvestri, O. Svelto, R. Szipöcs, F. Ferencz, Ch. Spielmann, S. Sartania, and F. Krausz, Opt. Lett. **22**, 522 (1997).

[24] M. Nisoli, S. Stagira, S. De Silvestri, O. Svelto, S. Sartania, Z. Cheng, M. Lenzner, Ch. Spielmann, and F. Krausz, Appl. Phys. B **65**, 189 (1997).

[25] S. Sartania, Z. Cheng, M. Lenzner, G. Tempea, Ch. Spielmann, F. Krausz, and K. Ferencz, Opt. Lett. **22**, 1562 (1997).

[26] W. H. Knox, IEEE J. Quantum Electron. **24**, 388 (1988).

[27] G. Boyer, M. Franco, J. P. Chambaret, A. Migus, A. Antonetti, P. Georges, F. Salin, and A. Brun, Appl. Phys. Lett. **53**, 823 (1988).

[28] P. C. Becker, H. L. Fragnito, R. L. Fork, F. A. Beisser, and C. V. Shank, Appl. Phys. Lett. **54**, 411 (1989).

[29] R. W. Schoenlein, J. Y. Bigot, M. T. Portella, and C. V. Shank, Appl. Phys. Lett. **58**, 801 (1991).

[30] D. Steinbach, W. Hügel, and M. Wegener, J. Opt. Soc. Am. B **15**, 1231 (1998).

[31] E. T. J. Nibbering, O. Dühr, and G. Korn, Opt. Lett. **22**, 1335 (1997).

[32] Y. Nabekawa, Y. Kuramoto, T. Sekikawa, and S. Watanabe, *Techn. Digest of CLEO/Pacific Rim '97* (Chiba, July 1997), p.19.

[33] Y. Nagata, K. Midorikawa, M. Obara, and K. Toyoda, Opt. Lett. **21**, 15 (1996).

[34] A. Rundquist, C. G. Durfee III, Z. Chang, C. Herne, S. Backus, M. M. Murnane, and H. C. Kapteyn, Science **280**, 1412 (1998).

[35] Y. Kobayashi, T. Sekikawa, Y. Nabekawa, and S. Watanabe, Opt. Lett. **23**, 64 (1998).

[36] See, e.g., V. G. Dmitriev, G. G. Gurzadyan, and D. N. Nikogosyan, *Handbook of Nonlinear Optical Crystals, 2nd ed.* (Springer-Verlag, Berlin, 1997).

[37] F. Seifert, V. Petrov, and F. Noack, Opt. Lett. **19**, 837 (1994).

[38] M. Nisoli, S. De Silvestri, V. Magni, O. Svelto, R. Danielius, A. Piskarskas, G. Valiulis, and A. Varanavicius, Opt. Lett. **19**, 1973 (1994).

[39] M. K. Reed, M. K. Steiner-Shepard, and D. K. Negus, Opt. Lett. **19**, 1855 (1994).

[40] M. K. Reed, M. S. Armas, M. K. Steiner-Shepard, and D. K. Negus, Opt. Lett. **20**, 605 (1995).

[41] V. V. Yakovlev, B. Kohler, and K. R. Wilson, Opt. Lett. **19**, 2000 (1994).

[42] S. R. Greenfield and M. R. Wasielewski, Opt. Lett. **20**, 1394 (1995).

[43] R. L. Byer and R. L. Herbst, in *Nonlinear Infrared Generation*, Y. R. Shen ed. (Springer-Verlag, New York, 1977), p.96.

[44] R. Danielius, A. Piskarskas, A. Stabinis, G. P. Banfi, P. Di Trapani and R. Righini, J. Opt. Soc. Am. B **10**, 2222 (1993).

[45] T. S. Sosnowski, P. B. Stephens, and T. B. Norris, Opt. Lett. **21**, 140 (1996).

[46] S. Fournier, R. L. Martens, C. Le Blanc, E. Baubeau, and F. Salin, Opt. Lett. **23**, 627 (1998).

[47] M. Nisoli, S. Stagira, S. De Silvestri, O. Svelto, G. Valiulis, and A. Varanavicius, Opt. Lett. **23**, 630 (1998).

[48] S. Takeuchi and T. Kobayashi, J. Appl. Phys. **75**, 2757 (1994).

[49] E. S. Wachman, W. S. Pelouch, and C. L. Tang, J. Appl. Phys. **70**, 1893 (1991).

[50] Q. Fu, G. Mak, and H. M. van Driel, Opt. Lett. **17**, 1006 (1992).

[51] G. M. Gale, M. Cavallari, T. J. Driscoll, and F. Hache, Opt. Lett. **20**, 1562 (1995).

[52] A. Shirakawa, H. W. Mao, and T. Kobayashi, Opt. Commun. **123**, 121 (1996).

[53] D. T. Reid, C. McGowan, M. Ebrahimzadeh, and W. Sibbett, IEEE. J. Quantum

Electron. **33**, 1 (1997).

[54] P. Di Trapani, A. Andreoni, G.P. Banfi, C. Solcia, R. Danielius, A. Piskarskas, P. Foggi, M. Monguzzi, and C. Sozzi, Phys. Rev. A **51**, 3164 (1995).

[55] P. Di Trapani, A. Andreoni, P. Foggi, C. Solcia, R. Danielius, and A. Piskarskas, Opt. Commun. **119**, 327 (1995).

[56] P. Di Trapani, A. Andreoni, C. Solcia, P. Foggi, R. Danielius, A. Dubietis, and A. Piskarskas, J. Opt. Soc. Am. B **12**, 2237 (1995).

[57] J. Wang, M. H. Dunn, and C. F. Rae, Opt. Lett. **22**, 763 (1997).

[58] A. Shirakawa, S. Morita, K. Misawa, and T. Kobayashi, *Techn. Digest of CLEO/Pacific Rim '97* (Chiba, July 1997), p.18.

[59] A. Shirakawa and T. Kobayashi, Appl. Phys. Lett. **72**, 147 (1998).

[60] A. Shirakawa and T. Kobayashi, IEICE Trans. Electron. **E81-C**, 246 (1998).

[61] F. Hache, M. Cavallari, and G. M. Gale, in *Ultrafast Phenomena X*, P. F. Barbara, J. G. Fujimoto, W. H. Knox, and W. Zinth eds. (Springer-Verlag, Berlin, 1996), p.33.

[62] T. Wilhelm, J. Piel, and E. Riedle, Opt. Lett. **22**, 1494 (1997).

[63] G. Cerullo, M. Nisoli, and S. De Silvestri, Appl. Phys. Lett. **71**, 3616 (1997).

[64] A. Shirakawa, I. Sakane, and T. Kobayashi, Opt. Lett. **23**, 1292 (1998).

[65] G. Cerullo, M. Nisoli, and S. De Silvestri, Opt. Lett. **23**, 1283 (1998).

[66] A. Shirakawa, I. Sakane, and T. Kobayashi, in *Techn. Digest of XIth International Conference on Ultrafast Phenomena* (Garmisch-Partenkirchen, 1998), postdeadline paper ThD2.

[67] A. Shirakawa, I. Sakane, and T. Kobayashi, Appl. Phys. Lett., to be published in the issue of 19 April 1999.

[68] J. Krasinski and A. Sieradzan, Opt. Commun. **26**, 389 (1978).

[69] S. Saikan, S. Ouw, and F. P. Schäfer, Appl. Opt. **18**, 193 (1979).

[70] O. E. Martinez, IEEE J. Quantum Electron. **25**, 2464 (1989).

[71] G. Szabó and Zs. Bor, Appl. Phys. B **50**, 51 (1990).

[72] R. A. Cheville, M. T. Reiten, and N. J. Halas, Opt. Lett. **17**, 1343 (1992).

[73] Th. Hofmann, K. Mossavi, F. K. Tittel, and G. Szabó, Opt. Lett. **17**, 1691 (1992).

[74] S. H. Ashworth, M. Joschko, M. Woerner, E. Riedle, and T. Elsaesser, Opt. Lett. **20**, 2120 (1995).

[75] B. A. Richman, S. E. Bisson, R. Trebino, M. G. Mitchell, E. Sidick, and A. Jacobson, Opt. Lett. **22**, 1223 (1997).

[76] B. A. Richman, S. E. Bisson, R. Trebino, E. Sidick, and A. Jacobson, Opt. Lett. **23**, 497 (1998).

[77] D. Eimerl, L. Davis, S. Velsko, E. K. Graham, and A. Zalkin, J. Appl. Phys. **62**, 1968 (1987).

[78] V. Krylov, A. Kalintsev, A. Rabane, D. Erni, and U. P. Wild, Opt. Lett. **20**, 151 (1995).

[79] M. K. Reed, M. K. Steiner-Shepard, M. S. Armas, and D. K. Negus, J. Opt. Soc. Am. B. **12**, 2229 (1995).

[80] J. P. Foing, J. P. Likforman, M. Joffre, and A. Migus, IEEE J. Quantum Electron. **28**, 2285 (1992).

[81] *Handbook of Chemistry and Physics, 69th ed.* (CRC Press, 1988–1989), p.E-383.

[82] R. L. Fork, C. V. Shank, C. Hirlimann, R. Yen, and W. J. Tomlinson, Opt. Lett. **8**, 1 (1983)

[83] R. A. Baumgartner and R. L. Byer, IEEE. J. Quantum Electron. **15**, 432 (1979).

[84] Zs. Bor and B. Rácz, Opt. Commun. **54**, 165 (1985).

[85] O. E. Martinez, Opt. Commun. **59**, 229 (1986).

[86] Zs. Bor, Opt. Lett. **14**, 119 (1989).

[87] R. Danielius, A. Piskarskas, P. Di Trapani, A. Andreoni, C. Solcia, and P. Foggi, Opt. Lett. **21**, 973 (1996).

[88] R. Danielius, A. Piskarskas, P. Di Trapani, A. Andreoni, C. Solcia, and P. Foggi, IEEE J. Quantum. Electron. **34**, 459 (1998).

[89] A. Dubietis, G. Jonusauskas, and A. Piskarskas, Opt. Commun. **88**, 437 (1992).

[90] E. B. Treacy, IEEE J. Quantum Electron. **5**, 454 (1969)

[91] R. L. Fork, O. E. Martinez, and J. P. Gordon, Opt. Lett. **9**, 150 (1984).

[92] O. E. Martinez, J. P. Gordon, and R. L. Fork, J. Opt. Soc. Am. A **1**, 1003 (1984).

[93] C. H. Brito Cruz, P. C. Becker, R. L. Fork, and C. V. Shank, Opt. Lett. **13**, 123 (1988).

[94] W. H. Knox, N. M. Pearson, K. D. Li, and C. A. Hirlimann, Opt. Lett. **13**, 574 (1988).

[95] G. Taft, A. Rundquist, M. M. Murnane, I. P. Christov, H. C. Kapteyn, K. W. Delong, D. N. Fittinghoff, M. A. Krumbügel, J. N. Sweetser, and R. Trebino, IEEE J. Sel. Top. Quantum Electron. **2**, 575 (1996).

[96] A. Baltuska, M. S. Pshenichnikov, and D. A. Wiersma, Opt. Lett. **23**, 1474 (1998).

[97] J. C. Diels, E. W. Van Stryland, and D. Gold, in *Picosecond Phenomena*, C. V. Shank, E. P. Ippen, and S. L. Shapiro eds. (Springer-Verlag, Berlin, 1978), p.117.

[98] A. M. Weiner, IEEE J. Quantum Electron. **19**, 1276 (1983).

[99] A. Piskarskas, D. Podenas, A. Stabinis, A. Umbrasas, A. Varanavichius, A. Yankauskas, and G. Yonushauskas, in *Ultrafast Phenomena V*, G. R. Fleming and A. E. Siegman eds. (Springer-Verlag, Berlin, 1986), p.142.

[100] O. E. Martinez, IEEE J. Quantum Electron. **23**, 59 (1987).

[101] G. M. Gale, F. Hache, and M. Cavallari, IEEE J. Sel. Top. Quantum Electron. **4**, 224 (1998).

[102] R. Szipöcs and A. Köházi-Kis, Appl. Phys. B **65**, 115 (1997), and references therein.

[103] I. T. Sorokina, E. Sorokin, E. Wintner, A. Cassanho, H. P. Jenssen, and R. Szipöcs, Opt. Lett. **22**, 1716 (1997).

[104] J. Hebling, E. J. Mayer, J. Kuhl, and R. Szipöcs, Opt. Lett. **20**, 919 (1995).

[105] M. Yamashita, M. Ishikawa, K. Torizuka, and T. Sato, Opt. Lett. **11**, 504 (1986).

[106] R. Szipöcs, K. Ferencz, Ch. Spielmann, and F. Krausz, Opt. Lett. **19**, 201 (1994).

[107] G. Tempea, F. Krausz, Ch. Spielmann, and K. Ferencz, IEEE J. Sel. Top. Quantum Electron. **4**, 193 (1998).

[108] C. P. Chang, Y. H. Lee and S. Y. Wu, Opt. Lett. **15**, 595 (1990).

[109] W. H. Knox, Appl. Phys. B 58, 225 (1994).

[110] Zs. Bor, K. Osvay, B. Rácz, and G. Szabó, Opt. Commun. 78, 109 (1990).

[111] K. Naganuma, K. Mogi, and H. Yamada, Opt. Lett. 15, 393 (1990).

[112] M. Beck, I. A. Walmsley, and J. D. Kafka, IEEE J. Quantum Electron. 27, 2074 (1991).

[113] K. Osvay, G. Kurdi, J. Hebling, A. P. Kovács, Zs. Bor, and R. Szipöcs, Opt. Lett. 20, 2339 (1995).

[114] A. Kovács, K. Osvay, Zs. Bor, and R. Szipöcs, Opt. Lett. 20, 788 (1995).

[115] R. Szipöcs, private communication.

[116] F. Hache, A. Zéboulon, G. Gallot, and G. M. Gale, Opt. Lett. 20, 1556 (1995).

[117] M. Takasaka, private communication.

[118] A. M. Weiner, J. P. Heritage, and E. M. Kirschner, J. Opt. Soc. Am. B 5, 1563 (1988).

[119] A. M. Weiner, D. E. Leaird, J. S. Patel, and J. R. Wullert, II, IEEE J. Quantum Electron. 28, 908 (1992).

[120] M. M. Wefers and K. A. Nelson, Opt. Lett. 18, 2032 (1993).

[121] M. A. Dugan, J. X. Tull, and W. S. Warren, J. Opt. Soc. Am. B 14, 2348 (1997).

[122] A. M. Weiner, S. Oudin, D. E. Leaird, and D. H. Reitze, J. Opt. Soc. Am. A 10, 1112 (1993).

[123] K. Takasago, T. Itoh, M. Takekawa, K. Utoh, and F. Kannari, Jpn. J. Appl. Phys. 35, 624 (1996).

[124] D. Yelin, D. Meshulach, and Y. Silberberg, Opt. Lett. 22, 1793 (1997).

[125] T. Baumert, T. Brixner, V. Seyfried, M. Strehle, and G. Gerber, Appl. Phys. B 65, 779 (1997).

[126] K. Nemoto, T. Fujii, N. Goto, T. Nayuki, and Y. Kanai, Opt. Lett. 21, 168 (1996).

[127] F. Druon, G. Chériaux, J. Faure, J. Nees, M. Nantel, A. Maksimchuk, G. Mourou, J. C. Chanteloup, and G. Vdovin, Opt. Lett. 23, 1043 (1998).

[128] G. M. Gale, private communication.

[129] A. Galvanauskas, A. Hariharan, D. Harter, M. A. Arbore, and M. M. Fejer, Opt. Lett. 23, 210 (1998).

[130] I. N. Ross, P. Matousek, M. Towrie, A. J. Langley, and J. L. Collier, Opt. Commun. 144, 125 (1997).

[131] See, e.g., Relaxation in Polymers, T. Kobayashi ed. (World Scientific, Singapore, 1993).

[132] See, e.g., Polydiacetylenes, D. Bloor and R. R. Chance eds. (Martinus Nijhoff Publishers, Dordrecht, Netherlands, 1985).

[133] S. Abe, in Relaxation in Polymers, T. Kobayashi ed. (World Scientific, Singapore, 1993), p.215.

[134] D. Bloor, F. H. Preston, D. J. Ando, and D. N. Batchelder, in Structural Studies of Macromolecules by Spectroscopic Methods, K. J. Ivin ed. (Wiley, New York, 1976), p.91.

[135] M. Yoshizawa, M. Taiji, and T. Kobayashi, IEEE J. Quantum Electron. 25, 2532 (1989).

[136] B. I. Greene, J. F. Mueller, J. Orenstein, D. H. Rapkine, S. Schmitt-Rink, and M. Thakur, Phys. Rev. Lett. 61, 325 (1988).

[137] W. B. Bosma, S. Mukamel, B. I. Greene, and S. Schmitt-Rink, Phys. Rev. Lett. 68, 2456 (1992).

[138] G. J. Blanchard, J. P. Heritage, A. C. Von Lehmen, M. K. Kelly, G. L. Baker, and S. Etemad, Phys. Rev. Lett. 63, 887 (1989).

[139] S. D. Halle, M. Yoshizawa, H. Matsuda, S. Okada, H. Nakanishi, and T. Kobayashi, J. Opt. Soc. Am. B 11, 731 (1994).

[140] E.g., A. J. Heeger, S. Kivelson, J. R. Schrieffer, and W. P. Su, Rev. Mod. Phys. 60, 781 (1988).

[141] C. V. Shank, R. Yen, R. L. Fork, J. Orenstein, and G. L. Baker, Phys. Rev. Lett. 49, 1660 (1982).

[142] S. Takeuchi, M. Yoshizawa, T. Masuda, T. Higashimura, and T. Kobayashi, IEEE J. Quantum Electron. 28, 2508 (1992).

[143] S. Takeuchi, T. Masuda, and T. Kobayashi, Phys. Rev. B 52, 7166 (1995).

[144] S. Takeuchi, T. Masuda, and T. Kobayashi, J. Chem. Phys. 105, 2859 (1996).

[145] T. Hattori and T. Kobayashi, Chem. Phys. Lett. 133, 230 (1987).

[146] T. Kobayashi, M. Yoshizawa, U. Stamm, M. Taiji, and M. Hasegawa, J. Opt. Soc. Am. B 7, 1558 (1990).

[147] M. Yoshizawa, A. Yasuda, and T. Kobayashi, Appl. Phys. B 53, 296 (1991).

[148] M. Yoshizawa, Y. Hattori, and T. Kobayashi, Phys. Rev. B 47, 3882 (1993).

[149] M. Yoshizawa, K. Nishiyama, M. Fujihira, and T. Kobayashi, Chem. Phys. Lett. 207, 461 (1993).

[150] A. Yasuda, M. Yoshizawa, and T. Kobayashi, Chem. Phys. Lett. 209, 281 (1993).

[151] K. Ichimura, M. Yoshizawa, H. Matsuda, S. Okada, M. M. Ohsugi, H. Nakanishi, and T. Kobayashi, J. Chem. Phys. 99, 7404 (1993).

[152] M. Yoshizawa, Y. Hattori, and T. Kobayashi, Phys. Rev. B 49, 13259 (1994).

[153] T. Kobayashi, M. Yasuda, S. Okada, H. Matsuda, and H. Nakanishi, Chem. Phys. Lett. 267, 472 (1997).

[154] J. Kinugasa, S. Shimada, H. Matsuda, H. Nakanishi, and T. Kobayashi, Chem. Phys. Lett. 287, 639 (1998).

[155] E. I. Rashba, in Excitons (Selected Chapters), E. I. Rashba and M. D. Sturge eds. (North Holland, Amsterdam, 1987), p.273.

[156] K. Nasu, J. Lumin. 38, 90 (1987).

[157] U. Stamm, M. Taiji, M. Yoshizawa, K. Yoshino, and T. Kobayashi, Mol. Cryst. Liq. Cryst. 182A, 147 (1990).

[158] B. E. Kohler and D. E. Schilke, J. Chem. Phys. 86, 5214 (1987).

[159] F. Kajzar and J. Messier, in Nonlinear Optical Properties of Organic Molecules and Crystals, Vol.2, D. S. Chemla and J. Zyss eds. (Academic Press, New York, 1987), p.51.

[160] D. Birnbaum, B. E. Kohler, and C. W. Spangler, J. Chem. Phys. 94, 1684

(1991).

[161] W. E. Torruellas, K. B. Rochford, R. Zanoni, S. Aramaki, and G. I. Stegeman, Opt. Commun. **82**, 94 (1991).

[162] A. Furuta and T. Kobayashi, to be published.

[163] I. Omine, M. Karplus, and K. Schulten, J. Chem. Phys. **68**, 2298 (1978).

[164] D. Guo, S. Mazumdar, S, N. Dixit, F. Kajzar, F. Jarka, Y. Kawabe, and N. Peyghambarian, Phys. Rev. B **48**, 1433 (1993).

[165] A. H. Zeweil, Science **242**, 1645 (1988).

[166] K. P. Cheung and D. H. Auston, Phys. Rev. Lett. **55**, 2152 (1985).

[167] M. J. Rosker, F. W. Wise, and C. L. Tang, Phys. Rev. Lett. **57**, 321 (1986).

[168] H. L. Fragnito, J. Y. Bigot, P. C. Becker, and C. V. Shank, Chem. Phys. Lett. **160**, 101 (1989).

[169] S. L. Drexheimer, Q. Wang, L. A. Peteanu, W. T. Pollard, R. A. Mathies, and C. V. Shank, Chem. Phys. Lett. **188**, 61 (1992).

[170] Q. Wang, R. W. Shoenlein, L. A. Peteanu, R. A. Mathies, and C. V. Shank, Science **266**, 422 (1994).

[171] T. A. Pham, A. Daunois, J. C. Merle, J. Le. Moigne, and J. Y. Bigot, Phys. Rev. Lett. **74**, 904 (1995).

[172] J. Y. Bigot, T. A. Pham, and T. Barisien, Chem. Phys. Lett. **259**, 469 (1996).

[173] H. Matsuzawa, S. Okada, H. Matsuda, and H. Nakanishi, Chem. Lett., 1105 (1997).

[174] H. Matsuzawa, S. Okada, H. Matsuda, and H. Nakanishi, Mol. Cryst. Liq. Cryst., **315**, 129 (1998).

[175] S. Okada, T. Doi, A. Mito, K. Hayamizu, A. Ticktin, H. Matsuda, N. Kikuchi, A. Masaki, N. Minami, K. H. Haas, and H. Nakanishi, Nonl. Opt. **8**, 121 (1994).

[176] R. H. Baughman, J. D. Witt, and K. C. Yee, J. Chem. Phys. **60**, 4755 (1974).

[177] W. F. Lewis and D. N. Batchelder, Chem. Phys. Lett. **60**, 232 (1979).

[178] D. N. Batchelder and D. Bloor, J. Phys. C **15**, 3005 (1982).

[179] B. S. Elman, M. K. Thakur, D. J. Sandman, M. A. Newkirk, and E. F. Kennedy, J. Appl. Phys. **57**, 4996 (1985).

[180] D. Bloor, W. Hersel, and D. N. Batchelder, Chem. Phys. Lett. **45**, 411 (1977).

[181] Z. Iqbal, R. R. Chance, and R. H. Baughman, J. Chem. Phys. **66**, 5520 (1977).

[182] C. H. Brito Cruz, J. P. Gordon, P. C. Becker, R. L. Fork, and C. V. Shank, IEEE J. Quantum Electron. **24**, 261 (1988).

[183] K. Misawa and T. Kobayashi, to be published.

[184] C. H. Brito Cruz, R. L. Fork, W. H. Knox, and C. V. Shank, Chem. Phys. Lett. **132**, 341 (1986).

[185] J. Orenstein, S, Etemad, and G. L. Baker, J. Phys. C **17**, L297 (1984).

[186] C. J. Bardeen, Q. Wang, and C. V. Shank. J. Phys. Chem. A **102**, 2759 (1998).

[187] L. M. Sveldlov, M. A. Kovner, and E. P. Krainov, *Vibrational Spectra of Polyatomic Molecules* (Willey, New York, 1970), p.282–323.

[188] J. M. Nunzi, C. Hirlimann, and J. F. Morhange, Chem. Phys. Lett. **221**, 199 (1994).

[189] M. J. J. Vrakking, D. M. Villeneuve, and A. Stolow, Phys. Rev. A **54**, 37 (1996).

[190] E. Schreiber, *Femtosecond Real-time Spectroscopy of Small Molecules And Clusters* (Springer-Verlag, Berlin, 1998), p.60.

[191] W. H. Press, S. A. Teukolsky, W. T. Vetterling, and B. P. Flannery, *Numerical Recipes in C* (Cambridge, USA, 1992), p.554.

[192] M. Yoshizawa, A. Kubo, and S. Saikan, to be published.

[193] H. Tanaka, M. Inoue, and E. Hanamura, Solid State Commun. **63**, 103 (1987).

[194] F. Zerbetto, J. Phys. Chem. **98**, 13157 (1994).

[195] H. Kandori, H. Sasabe, and M. Mimuro, J. Am. Chem. Soc. **116**, 2671 (1994).

[196] W. T. Pollard, H. L. Fragnito, J. Y. Bigot, C. V. Shank, and R. A. Mathies, Chem. Phys. Lett. **168**, 239 (1990).

[197] W. T. Pollard, S. L. Drexheimer, Q. Wang, L. A. Peteanu, C. V. Shank, and R. A. Mathies, J. Phys. Chem. **96**, 6147 (1992).

[198] C. J. Bardeen, Q. Wang, and C. V. Shank, Phys. Rev. Lett. **75**, 3410 (1995).

[199] G. Cerullo, C. J. Bardeen, Q. Wang, and C. V. Shank, Chem. Phys. Lett. **262**, 362 (1996).

[200] J. Swiatkiewicz, X. Mi, P. Chopra, and P. N. Prasad, J. Chem. Phys. **87**, 1882 (1987).

[201] F. Zerbetto and M. Z. Zgierski, J. Chem. Phys. **101**, 1842 (1994).

[202] A. Karpfen, J. Phys. C **13**, 5673 (1980).

[203] A. C. Cottle, W. F. Lewis, and D. N. Batchelder, J. Phys. C **11**, 605 (1978).

[204] M. J. S. Dewar, *Hyperconjugation* (Ronald Press, New York, 1962), p.48.

[205] O. E. Martinez, J. Opt. Soc. Am. B **3**, 929 (1986).

[206] A. Yariv, *Quantum Electronics, 3rd ed.* (John Willey & Sons, New York, 1988), p.106.

[207] M. Born & E. Wolf, *Principles of Optics, 6th ed.* (Pergamon Press, Oxford, 1980), p.177.

[208] S. D. Brorson, and H. A. Haus, J. Opt. Soc. Am. B **5**, 247 (1988).

[209] T. R. Zhang, H. R. Choo, and M. C. Downer, Appl. Opt. **29**, 3927 (1990).

[210] A. A. Maznev, T. F. Crimmins, and K. A. Nelson, Opt. Lett. **23**, 1378 (1998).

[211] J. Janszky, G. Corradi, and R. N. Cyuzalian, Opt. Commun. **23**, 293 (1977).

[212] Y. Ishida, T. Yajima, and A. Watanabe, Opt. Commun. **56**, 57 (1985).

[213] D. J. Kane and R. Trebino, Opt. Lett. **18**, 823 (1993).